# Comparative Study and Analysis of THz Pulse and Continuous-wave Imaging towards Medical Application

by

Bahar Davoudi

A thesis
presented to the University of Waterloo
in fulfillment of the
thesis requirement for the degree of
Master of Applied Science
in
Electrical and Computer Engineering

Waterloo, Ontario, Canada, 2009

©Bahar Davoudi 2009

# AUTHOR'S DECLARATION

I hereby declare that I am the sole author of this thesis. This is a true copy of the thesis, including any required final revisions, as accepted by my examiners.

I understand that my thesis may be made electronically available to the public.

# Abstract

Until recently, there had been a gap between the output frequencies of electronic and optical sources, which included waves of frequencies around 300 GHz to 3 THz and was known as the Terahertz gap. After the development of sources and detectors that operated at these frequencies, Terahertz radiation began to find its way through a variety of applications such as surveillance, spectroscopy and medical imaging.

Terahertz radiation has been used in medical imaging experiments on different in-vitro and some in-vivo biological tissues and has shown promising results in differentiating certain features in those tissues. Moreover, it has demonstrated well in detecting certain polar molecules due to these molecules' fingerprint in Terahertz range of frequencies. Considering these facts, Terahertz has been proved to have the potential for being a perspective medical imaging method, which can be used as a complement to other imaging techniques such as MRI or X-ray or even as a separate method.

Due to the capacity of Terahertz radiation, much research is being done on using Terahertz generation-detection set-ups for medical imaging and improving the imaging parameters of these set-ups to capture more precise and meaningful images. In this thesis, the imaging parameters of two different THz imaging set-ups have been studied and compared. One of these imaging set-ups is a THz pulse set-up with photoconductive dipole antennas as source and detector and the other one is a continuous-wave set-up with a backward wave oscillator as the source and a Golay cell as the detector. To the best of our knowledge, a comparative analysis of the imaging parameters of these two types of THz imaging set-ups has not been performed previously.

In this thesis, parameters such as modulation transfer function (MTF), resolution and beam profile have been measured through the experiments, for both the THz pulse and THz CW imaging set-ups. These results are compared to the results obtained by theoretical formulas and the reason for any differences occurred between these two results has been explained. Moreover, the imaging parameters found from the experiments for the two set-ups have been compared together and similarities and differences have been discussed.

In this thesis, a set of experiments has also been done to verify the capability of the two imaging set-ups for in-vitro tooth imaging, towards developing THz imaging systems suitable for clinical imaging application. These experiments have been performed on a tooth crown sample with the pulse set-up and on a tooth cross-section sample with the continuous-wave set-up. The capability of our THz pulse

imaging system to distinguish thickness variations in a tooth crown sample by time-of-flight imaging has been shown and discussed.

# Acknowledgements

Hereby, I would like to thank my supervisor, Professor Safieddin Safavi Naeini, for his continuous guidance and invaluable support without which writing this thesis would not have been possible.

I also thank Dr. Simarjeet S. Saini and Dr. Amir H. Majedi for offering their time to review this thesis.

I would like to thank Dr. Daryoosh Saeedkia for introducing the THz world to me and for guiding me through my first steps in research on THz.

I would like to thank Dr. Arash Rohani, Mohammad, George, Amir, Daniel and all my colleagues in Professor Safavi Naeini's research group who answered my questions generously and patiently.

I would like to thank Mehrnoosh and Shahed for their assistance in the programming tasks of the imaging experiments.

Last but not least, I would like to thank my mother and father for their endless "tele-support".

# Dedication

I would like to dedicate my thesis to all the students who are taking their first steps in the world of THz medical imaging by reading this thesis.

# Table of Contents

# List of Figures

# List of Tables

# Chapter 1
# Introduction

In this chapter, an introduction to the contemporary methods of medical imaging has been presented and the major advantages and disadvantages of these methods have been mentioned. Moreover, Terahertz imaging has been introduced as an imaging method that has proved to overcome some of the drawbacks of common imaging methods. The introduction continues with a brief history of Terahertz imaging and its development up to the present. The chapter ends with an overview on the contents of this thesis.

## 1.1 A glance at medical imaging methods

Medical imaging is one of the fast-growing fields of research in today's world. Physicians from one side and biomedical physicists and engineers from the other side are leading the research in this area which has kept this field extremely up-to-date. Therefore, I believe that any research done on enhancing the current imaging methods or finding new methods which would overcome the disadvantages of currently used methods would be a fruitful research.

Today, the most common medical imaging techniques are X-ray, magnetic resonance imaging (MRI), Ultrasound and optical coherence tomography (OCT). Even though Terahertz isn't considered as one of these techniques yet, there are a number of features which makes this range of spectrum a good candidate for medical imaging purposes either as an independent technique or as a complement to some of the other medical imaging techniques. In this section we first go through a brief introduction into the advantages and disadvantages of common methods of medical imaging and then look into the features of Terahertz which makes it possible for this type of imaging to overcome some of the disadvantages of the common methods.

### 1.1.1 Advantages and disadvantages of common medical imaging methods

So far, X-ray has been the most powerful imaging method for monitoring the hard tissues of the body such as bone and tooth. The major disadvantage of X-ray imaging is that it is an ionizing radiation and has severe harmful effects on patient's body. Moreover, due to Rayleigh scattering around X-ray frequencies, the images taken with this method are generally considered as noisy images. The highest resolution achieved with this method is 50μm; however, the common resolution of X-ray images is smaller than this value. [1, 9, 11, 12]

Magnetic resonance imaging is a powerful method for soft tissue imaging. The images taken with this method are clear and precise; the resolution, however, is about 300μm. The main advantage of this method is that it doesn't contain any exposure to ionizing radiation and thus is considered much less harmful than X-ray. [1, 9, 10, 12]

Ultrasound imaging is one of the common methods of imaging due to being harmless especially for cases such as fetus imaging. A severe disadvantage of this method is the noise associated with the images taken with this method. Moreover, the penetration depth in this method is less than X-ray. The resolution of ultrasound images is between 25μm and 400μm. [1, 9, 12]

Optical coherence tomography (OCT) is a recently developed imaging method which is used for imaging of outer or inner surfaces of the body due to its small depth of penetration (2mm-3mm). Despite its small penetration depth, OCT has many upsides which make it the best imaging method for certain applications. Having high depth and transversal resolution, being harmless, contact-free and non-invasive and the possibility of using different methods of contrast formation with OCT are the major advantages of this imaging method. Moreover, availability and ever-growing development of optical sources such as photonic crystal fibres have played an important role in the enhancement of OCT. Today, different modalities of OCT are used in different imaging and therapeutic applications: Ultra-high resolution OCT and Functional OCT in in-vivo biopsy, Polarization Sensitive OCT in tooth imaging, high resolution OCT and spectroscopy in imaging of the gastrointestinal system, Doppler OCT in haemostatic therapy and conventional OCT in ophthalmology. [26, 41, 42]

### 1.1.2 A look at the potentials of Terahertz

After an introduction into the common methods used in medical imaging, we look at the potentials of Terahertz radiation which have theoretically been proved to be practicable in medical imaging and compare the advantages and disadvantages of Terahertz imaging with other imaging methods. Advantages such as relatively low scattering and better penetration of Terahertz waves compared to infrared frequencies, the possibility of phase measurement as well as amplitude measurement with detectors designed for Terahertz frequencies and also the possibility of applying both the imaging and the spectroscopy concepts in order to capture meaningful images, are considered as the main advantages of imaging at Terahertz frequencies, which make it a good candidate for medical imaging. Even though in this thesis no spectroscopic characteristic of Terahertz has been used in imaging, the simultaneous application of imaging and spectroscopy is a tool which is used currently in THz medical imaging research.

In order to diagnose a number of skin diseases (such as psoriasis-thickening of the epidermis-) MRI and ultrasound imaging are used. It is shown that the same diagnosis can be made by Terahertz pulse imaging; in which case, the diagnosis would become less expensive than MRI and would be contact-free unlike ultrasound imaging. [26]

There is also another context in which THz imaging is believed to perform more successfully than the common imaging techniques: The process of wound healing. Currently, invasive methods are used to diagnose the state of the wound so that the doctor would prescribe the proper drugs, while THz imaging is a non-invasive way to monitor the wound healing process. Moreover, with THz imaging, there would be no need for removing the wound dressings. This technique also provides a method for distinguishing a wound that forms a scar and enables the doctor to use certain drugs to prevent formation of scar tissues. [26, 27]

In order to detect skin cancer, OCT is the most powerful tool that is currently used. It can penetrate up to 2-3mm and can form images with resolution up to 10μm. Terahertz pulse imaging has performed a penetration depth of at least 1.5μm into the tissue and has been proved to achieve penetration depths more than that of OCT, since the Terahertz wave has a higher wavelength than the optical wave. Moreover, THz images have been taken which have the same resolution as that of OCT. Additionally, THz has the advantage of being less scattered than optical and infra-red waves. [26, 41]

MRI and ultrasound imaging are also used for skin imaging but there are small problems associated with these methods. In order to achieve the resolution of skin imaging with MRI, special coils are needed which makes it more costly. As for ultrasound, it cannot differentiate between the benign and malignant tumors, a task that has been performed successfully by Terahertz pulse imaging for in vitro samples. According to all these reasons, it is believed that THz imaging will eventually be used as a complementary method to common methods of skin cancer detection. [26]

X-ray is the imaging method most extensively used for tooth imaging but as mentioned earlier, it is harmful for body tissues and its use must be restricted to severe occasions. Therefore, it cannot be an appropriate method for regular dental check. Moreover, X-ray is incapable of detection of early tooth caries. That is why OCT has begun to find its way in applications such as tooth imaging. Even more, Terahertz has also proved that it can distinguish early tooth caries as well as OCT while it is expected to penetrate more in the tooth than OCT. [26, 41]

Generally, THz imaging is expected to perform most of the imaging tasks in which OCT is used because of their similar ability in depth and spectroscopic measurements. The main obstacle to this

objective is the lack of powerful sources at Terahertz frequency which can be used for imaging purposes. Moreover, lack of waveguides such as fiber optics which can deliver the Terahertz wave to the site of imaging inside the body is a grave problem in the way of THz medical imaging, while this problem has long been solved for optical and infrared frequencies. If such problems are solved, we would witness the application of Terahertz imaging as a complement to techniques such as MRI, ultrasound or OCT or even as the leading method of imaging in a number of applications due to the unique features of terahertz wave as well as the characteristic fingerprints that some biological tissues have at terahertz frequencies. [26]

## 1.2 Development of Terahertz imaging

The THz gap generally refers to the frequencies between 300GHz and 3 THz which occupy the range of 0.3 to 300 μm in the spectrum. Until recently, it was difficult to develop high-power sources and sensitive detectors in this region. That is the reason why this region in spectrum was called the ‘‘Terahertz gap’’ for a long time. [19]

Terahertz imaging was first used in astrophysics and space sciences. For the past 30 years the Terahertz radiation from the interstellar gases has been studied. [18, 30] The first step towards detecting Terahertz radiation was taken in 1890s by H. Reubens and E. F. Nicoles while they were doing measurements on blackbody radiations with a bolometer. [28] In the past, large and expensive sources such as free electron lasers or thermal sources were used for generating Terahertz radiation. These sources generated weak and incoherent Terahertz signal. [21]

During late 1980s a research group at AT&T Bell Laboratories and at IBM’s T. J. Watson Research Laboratories were the first team who were able to bridge the THz gap. This was achieved by gating biased photoconductive dipole antennas. [1] Terahertz pulse was generated and measured by Auston et al. for the first time in 1984. At that time he used both photoconductive antenna and optical rectification to generate a terahertz pulse. [23] After this achievement, research on Terahertz sources and detectors started to flourish at a high rate.

THz started finding its way through molecular spectroscopy and imaging in the mid 1990s. The first THz imaging system is believed to be developed by Hu and Nuss which was based on optoelectronic terahertz time-domain spectroscopy. In their developed set-up, a pulse was generated by a Ti-Sapphire laser. This pulse generated THz radiation after hitting a semi-insulating GaAs,. After collimation and being focused on the sample, this THz pulse was detected by an optically gated dipole detector. [18, 19, 22]

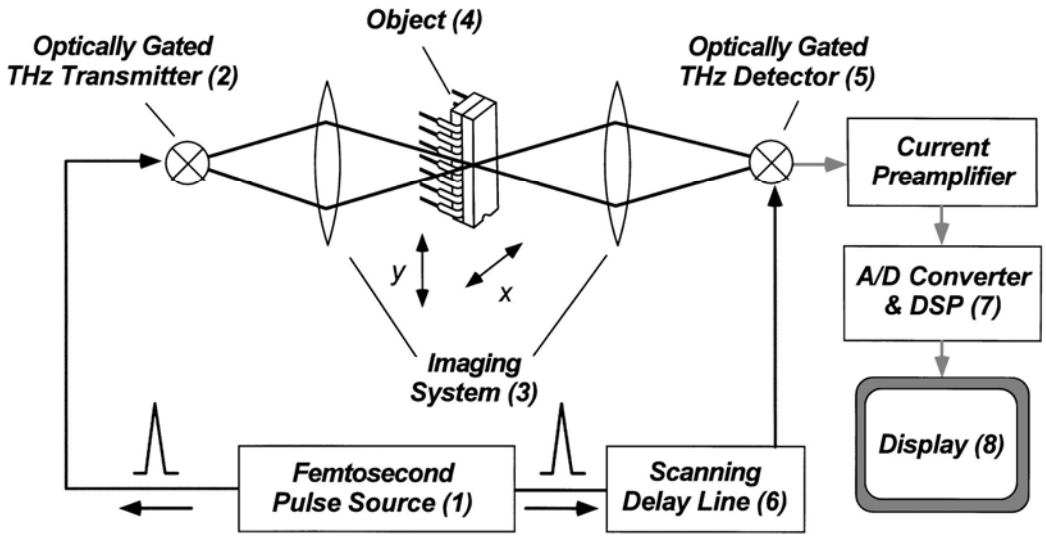


Fig. 1. 1 The schematic of the first THz imaging system developed by Hu and Nuss [22]

Advances and new technologies introduced in the field of ultra short pulse lasers, crystal growth techniques and non-linear optics have led to design and manufacture of original Terahertz sources as well as coherent Terahertz detectors that work in room temperature and cover a wide range of frequency. [29]

The first Terahertz images of biological tissue were taken in 1999. A short while after this event, Terahertz pulsed imaging was used on tooth caries inspection and two years after that, in 2001, the first in vivo reflection mode Terahertz imaging of the skin was performed. At the same year, the first ex vivo measurements of skin cancer was demonstrated. Finally, in a two years time after this event, the first commercialized reflection mode Terahertz imaging system was introduced. So far, a number of research groups have been working on different applications of Terahertz such as tissue imaging, disease diagnostics, performing label-free DNA sequencing and observing the radiation effects of THz on biological samples. On 2004, a commercial THz imaging system was reported to be installed in a hospital environment as a trial. [18, 30]

Up to this date, Terahertz medical imaging has gone through much advancement regarding both imaging techniques [32] and the samples being used for imaging. From the imaging techniques point of view, the most recent research includes high resolution imaging [15], near-field imaging [15], tomographic imaging [16, 36] and compress sensing imaging [17]. Moreover, considering the

imaging samples, Terahertz medical imaging has recently been performed on tooth and artificial skin models. Moreover, it has been used for primary imaging of excised breast carcinoma and also for revealing the contrast between the healthy skin and basal cell carcinoma both in vitro and in vivo. [28, 30]

## 1.3 Overview of thesis

This thesis starts with an introduction into sources of Terahertz generation as well as Terahertz detectors in chapter two with is followed by a discussion about the characteristics, advantages and disadvantages of those sources and detectors that are more commonly used in medical imaging in experimental set-ups. Chapter three offers a review on the major characteristics of Terahertz wave and the behavior of some materials in this range of frequency and then discusses on how these features can be used in medical applications such as spectroscopy or imaging. Some examples of the research, which has been done on THz imaging of different biological samples, are also shown. Moreover, in this chapter, a review on the definition of the major imaging parameters such as resolution is offered and the methods that were used to measure such parameters at Terahertz frequencies by different research are examined. Chapter four presents the THz pulse and THz continuous-wave set-ups and the imaging samples that were used for the experiments done in this thesis. In chapter five, the methods, experiments and simulations which were done in this thesis are explained and the results of these experiments and simulations are presented. Moreover, the results of different experiments have been compared together and deviations from the results expected from theory have been explained. Furthermore, the alignment procedure of the THz pulse and also the CW imaging set-up have been described in the appendix.

# Chapter 2
# Terahertz Sources and Detectors and Their Application in THz Imaging

This chapter introduces different sources and detectors that can be used for THz generation and detection, respectively. THz imaging set-ups which have been designed and used by a number of research groups are also shown. Moreover, the sources and detectors that are most commonly used in THz imaging set-ups are compared in terms of their performance.

## 2.1 Terahertz generation and detection

### 2.1.1 Terahertz generation

THz sources are generally categorized into two main groups according to the method used for their generation: Sources based on electronics and sources based on photonics. [21] Gyrotrons [24], synchrotrons, backward wave oscillators (BWO) [24], Gunn diodes and super-lattice electronic devices are examples of electronic based THz sources while lasers, photomixing devices [21, 24, 37] and photoconductive dipole antennas [23] are considered as photonics based sources for THz generation. Generally, the electronic based THz sources generate waves of frequencies around the microwave end of the THz frequencies. The upper frequency limit for these sources is usually about 300 GHz (except for BWO which can generate up to 1 THz) while the upper frequency limit for photonics based sources has reached hundred Terahertz. This makes electronic based THz sources less proper for medical applications and photonics based sources more common for such applications. [21 39]

What comes below is a brief description of the Terahertz generation method used in a number of the common Terahertz sources.

#### 2.1.1.1 Electronics-based Terahertz sources

##### 2.1.1.1.1 Gyrotrons and Backward wave oscillators (BWO)

Gyrotrons and backward wave oscillators (BWO) are examples of electron beam sources. In sources of this type, a high-energy electron beam interacts with a strong magnetic field in a resonant cavity which results in an energy transfer between the electron beam and electromagnetic wave. Today,

gyrotrons with 1MW power at 140 GHz [25] and backward wave oscillators with 50mW power at 300GHz have been manufactured. [24]

#### 2.1.1.1.2 Synchrotrons

Synchrotrons also use the interaction between high energy electrons and a magnetic field to generate Terahertz radiation. It has been reported that a research group at Jefferson Lab, USA have developed a 20W Terahertz source by using a synchrotron. This amount of power is many times more than the power of conventional Terahertz sources, which is about 1mW. [28]

### 2.1.1.2 Photonics-based Terahertz sources

Among this type of Terahertz sources are sources that generate pulsed Terahertz signal and sources that generate narrowband Terahertz signal, which are considered as continuous-wave sources. The most common photonics-based sources of the first category are photoconductive antenna and nonlinear crystals and some examples of the second category are optically pumped far-infrared gas lasers, Terahertz semiconductor lasers, photomixing in ultra-fast photoconductors and parametric interaction in nonlinear crystals. What comes below is a short review on Terahertz generation in a number of photonics-based Terahertz sources.

#### 2.1.1.2.1 Photoconductive antenna

In this method of Terahertz generation, the short pulse of a laser (normally of the order of 100fs or less) is incident on a biased semiconductor (usually Low temperature grown GaAs) of a photoconductive antenna. The bias voltage on the electrodes is in the range of 1-10kV per centimetre. The separation between the electrodes is of the order of hundreds of micrometers to a few centimetres. For the first antennas of this type, the gap between the electrodes was a few hundred micrometers while the laser spot size was 10 micrometers.

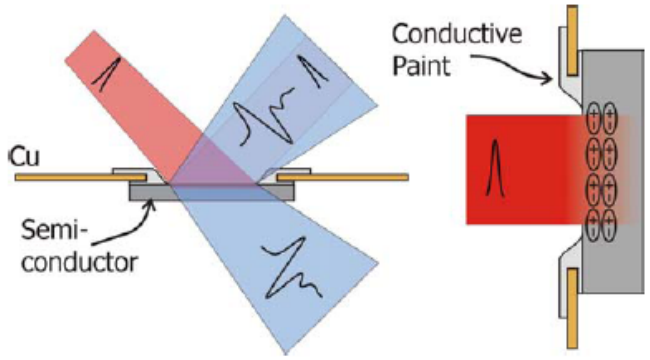


Fig. 2. 1 PDA as a Terahertz source. Left: The red beam is the laser pulse incident on the PDA and the blue beam is the generated THz pulse. Right: A bias voltage is applied cross the semiconductor. When the laser pulse hits the gap between the electrodes, electron-hole pairs are generated [23]

When the short pulse laser hits the biased semiconductor, it generates electron-hole pairs. At this stage, the insulating semiconductor becomes conductor and the flow of the electron-hole pairs along the semiconductor between the electrodes gives rise to the photoconductive current which depends on the pulse length. This photocurrent, however, decays with a rate depending on the carrier lifetime of the semiconductor. In far field, the terahertz electric field is proportional to the transient photocurrent due to Maxwell equations. This proportionality is shown in the following figure. [23]

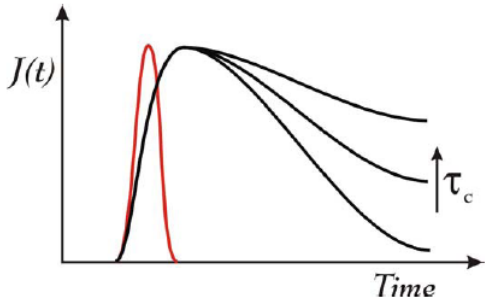


Fig. 2. 2 The pulse from the laser (shown in red) excites photocurrent in the PDA [23]

2.1.1.2.2 Optical rectification

When the IR pulse from the femtosecond laser passes through a crystal, it undergoes a nonlinear effect that results in a mixing of the frequency components of the IR pulse. These different frequencyomponents constitute the frequency components of a THz pulse. [21]

2.1.1.2.3 Photomixing

One of the ways to generate continuous terahertz wave is to optically mix light from two sources which are usually two laser diodes with frequency difference in the Terahertz range of spectrum. When near-infrared photons with frequency $f_1$ interact with the optical vibration modes inside a nonlinear crystal (such as $LiNbO_3$), some of their energy is transferred to the crystal and generates a photon with frequency $f_2$. After this interaction, the frequency of the output Terahertz signal from the crystal equals $f_1 - f_2$. The generated THz signal can then be coupled to a waveguide or an antenna. [24, 37]

2.1.1.2.4 Quantum cascade laser (QCL)

The most well-known Terahertz semiconductor laser is the quantum cascade laser, in which a carrier transition between various energy levels within the same band (either conduction or valence) results in a lasing in Terahertz frequency. So far, the highest power of a quantum cascade laser working at 300 K has been 3.5W at 33 THz. [24]

Quantum cascade lasers are regarded as CW Terahertz sources that are based on GaAs-AlGaAs hetero-structures. The power they generate is around tens of milliwatts. Until recently, these lasers worked in very low temperature. In 2005, however, a QCL has been developed which operates at up to 164k at approximately 3THz in pulsed mode. Since application of these types of lasers as a source of Terahertz generation is a relatively new field, much research is being done on optimization of a number of QCL's parameters, the most important of which is broadening its frequency range of operation. Currently this range is between 2 to 4.4 THz. [28, 37]

2.1.1.2.5 Optically-pumped far-infrared gas lasers

In optically-pumped far-infrared gas lasers a $CO_2$ pump laser radiates into a cavity which is filled with a certain gas. This gas lases at THz frequencies. By changing the gas inside that cavity, the lasing frequency can be changed. For a laser pump with a power of 20-100W, the common output power of the far-infrared gas lasers is 1-20mW. [24]

### 2.1.2 Terahertz Detection

Different techniques have been used for detection of Terahertz radiation. Usually when the source of Terahertz is either a photoconductive antenna or a nonlinear crystal, the same structure is used as the detector. Moreover, these two types of detectors are used when coherent detection of Terahertz signal is required. Some of the other devices and methods that are used for Terahertz detection are Golay

cell, bolometer and also CCD camera together with an analyzer and spectrometer. These methods are briefly introduced in 2.1.2.1 through 2.1.2.5.

#### 2.1.2.1 Detection by photoconductive antenna

In this method of detection, the pulse coming from the femtosecond laser is split between the THz source and the photoconductive antenna at the detector. This pulse gates the detecting antenna and thus generates carriers. Then, the generated Terahertz provides the bias field for these carriers and thus, a current is formed at the detector. If the detection antenna is connected to a lock-in amplifier via a current amplifier device and the delay of the gating pulse is monitored for a time interval, the electric field of the Terahertz pulse can be observed on the lock-in amplifier. [23]

#### 2.1.2.2 Detection by nonlinear crystal

In this method, the Terahertz electric field is incident on an optically transparent material and it undergoes a nonlinear effect. This effect causes a mixing in the frequency components of the THz pulse. This change in frequency component, which is proportional to the change in the THz electric field, is then detected to find the THz field. [27, 44]

#### 2.1.2.3 Detection by Golay cell

Golay cell is a metallic cylindrical cavity filled with xenon. This cylinder is covered by a blackened metallic plate from one side and a flexible metallic diaphragm from the other side. When the Infrared or Terahertz signal is incident on the blackened surface, the xenon gas inside begins to expand and deform the metallic diaphragm. There is also a lamp which lightens the diaphragm and a photocell which detects the reflected light from the diaphragm. The change in the deformity of the diaphragm thus changes the amount of light detected by the photocell. [48]

#### 2.1.2.4 Detection by high-temperature superconducting bolometer

High-temperature superconducting bolometers (HTSB) consist of two main parts: A radiation-absorbing part and another part which performs as a heat sink. These two parts are connected to one another with an insulating material. When the absorbing part absorbs the electromagnetic radiation, its temperature increases; while, the temperature of the heat sink remains constant. By measuring the difference in the temperature of the two parts, the absorbed energy from the radiation can be measured. Thin films of $YBa_2Cu_3O_{7-\delta}$ (YBCO) are used as the superconducting material in fabrication of HTSB. Some of the materials that have been used so far as the substrates in the structure of HTSC are MgO, $SrTiO_3$ and zirconia related materials. Bolometers are generally known

as ultra wide bandwidth and low noise detectors. They are considered as the most sensitive detectors at sub-millimetre wavelengths. This group of detectors are used mostly for radio astronomy applications. [45, 46]

#### 2.1.2.5 Detection by a CCD camera

The concept in this method of detection is to convert a Terahertz signal detected by a common detection method (such as nonlinear optical crystal) to an optical signal by using a cross polarizer and then take the image of the optical signal with a charge coupled digital camera. A realization of this method has been shown in 2.2.3. [44]

## 2.2 Examples of Terahertz transmitters and receivers in imaging set-ups

In this section, examples of the set-ups and devices which have been used for THz imaging research and have been presented in literature have been presented. The first five subsections are mainly about different types of sources and detectors that are available in Terahertz imaging set-ups. According to the articles published on Terahertz imaging, the most common emitters and receivers that have been used for research on Terahertz imaging are photoconductive antenna and ZnTe crystal. Moreover, the idea of using a CCD camera together with a ZnTe crystal detector has also been mentioned. Examples of set-ups in which these sources and detectors have been used are given in 2.2.1 through 2.2.5.

Apart from the pulsed Terahertz sources which are more commonly used due to their ability to perform time-of-flight measurement, employment of a continuous-wave source has also been reported for THz imaging, which is mentioned in 2.2.5.

The last subsection introduces a newly developed probe for near-field Terahertz imaging.

### 2.2.1 Set-up with Photoconductive antenna as transmitter and receiver

PDAs are one of the most commonly used transmitters and receivers in Terahertz imaging set-ups due to their advantages which will be discussed in 2.3. They can be used either in a set-up designed for transmission-mode imaging or for reflection-mode imaging.

#### 2.2.1.1 Transmission-mode imaging

In a common transmission-mode Terahertz pulsed imaging set-up, the beam generated by a pulsed laser is split between the Terahertz emitter and an optical delay line. The generated Terahertz beam is collimated and then focused on the sample with a pair of parabolic mirrors (or lenses) and then defocused and collimated through two other parabolic mirrors (or lenses) and is then incident on the Terahertz detector. The probe beam reflected from the delay line gates the detector. [26]

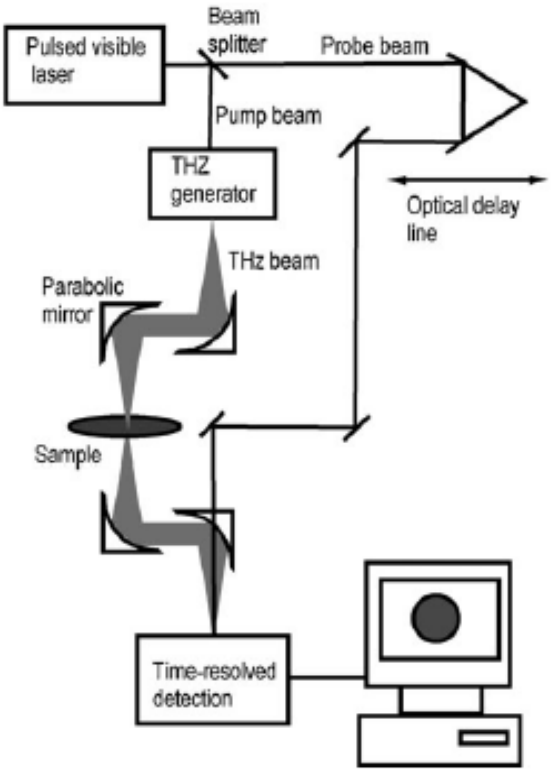


Fig. 2. 3 Configuration of a pulsed Terahertz imaging system in transmission-mode [26]

#### 2.2.1.2 Reflection-mode imaging

The reflection-mode Terahertz pulsed imaging set-up uses the same generation and detection concept as a transmission-mode set-up. The only difference between these two configurations is that in the reflection mode imaging, the source and detector are both at the same side of the object while in transmission mode imaging, they are located at two different sides of the object. The configuration of a reflection-mode Terahertz pulsed imaging set-up is shown in figure 2.4.

This system is an example of an imaging set-up (TPI Imaga1000) which is developed by Teraview Ltd, UK. The source of pulses is a Ti:Sapphire with 800nm of wavelength radiating 100fs pulses. The frequency range of the generated Terahertz signal in this set-up is from 0.1 to 4THz with an average power of around 100nW. Moreover, the SNR is about 4000:1. [1]

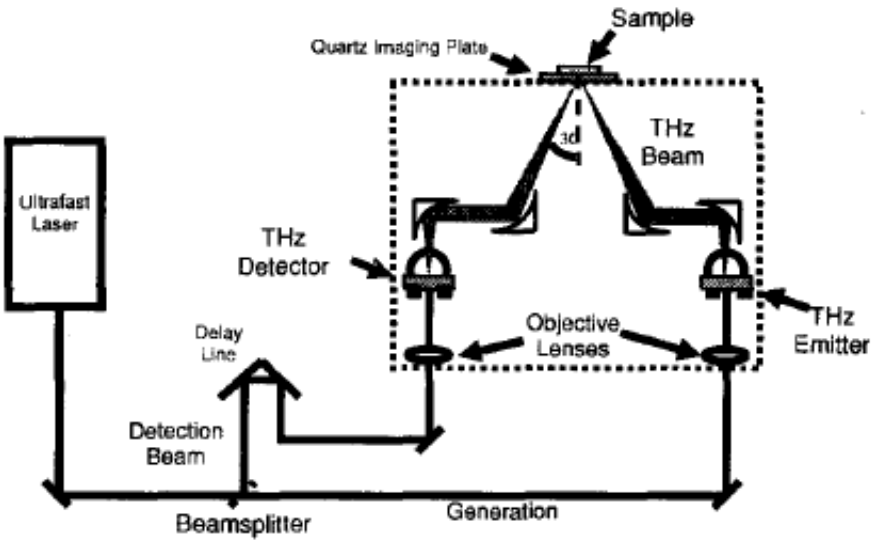


Fig. 2. 4 Configuration of a pulsed Terahertz imaging system in reflection-mode with PDAs as transmitter and detector [20]

### 2.2.2 Set-up with nonlinear optical crystal as transmitter and receiver

The source in this set-up is a coherent femtosecond laser producing 160fs pulses at 800nm central wavelength with 250 kHz repetition rate and average power of 1W. The set-up configuration is very similar to that of a common pulsed transmission-mode imaging set-up. The laser beam is split into two beams, one going to the Terahertz generator and one being used as a probe and passing through a delay line. The Terahertz generator in this example is a nonlinear ZnTe crystal. When the laser pulse passes through this crystal, it undergoes the process mentioned in 2.1.1 to generate Terahertz radiation. After becoming collimated and then being focused on the object, this radiation, together with the probe beam are incident on the detector which is also a nonlinear ZnTe crystal. [27]

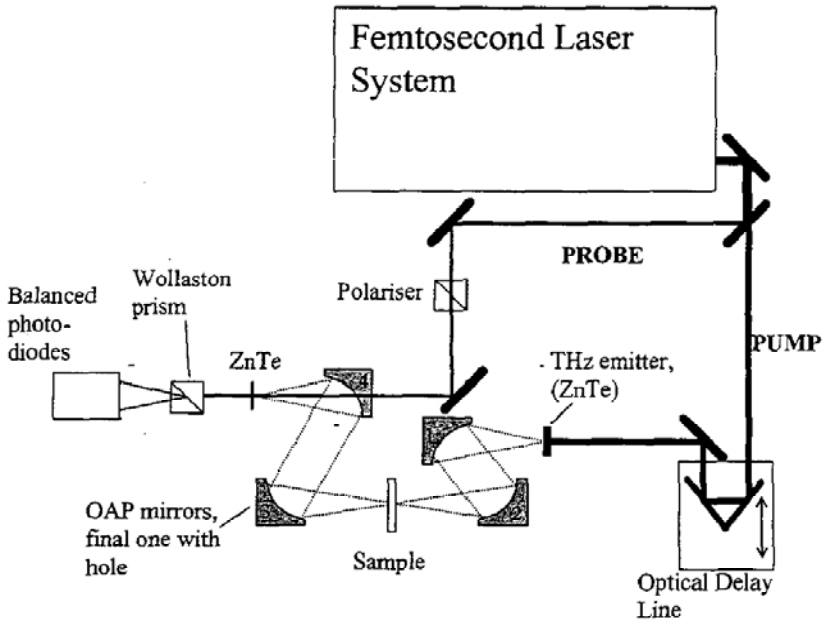


Fig. 2. 5 Configuration of a pulsed Terahertz imaging system in transmission-mode with nonlinear optical crystals as emitter and detector. [27]

A polariser is put in the path of the probe signal in order to circularly polarize it. The THz beam changes the birefringence of ZnTe which is at the detector side. Then, the circularly polarised probe beam would undergo a non-linear effect after passing through the detector which is called the Pockels effect. Pockels effect is the birefringence that occurs in materials because of the presence of an electric field. Because of birefringence, the refractive index of the crystal would be different for different components of the incident wave and thus one component is favoured over another and that causes the beam to become elliptically polarized. Afterwards, the probe beam passes through a Wollaston prism which separates the two components of the beam. These two separated beams go to a pair of photodiodes where their intensity is measured. The difference in the intensity of the two beams is calculated in the form of voltage. The change in this voltage indicates the change in the Terahertz field. [27]

### 2.2.3 2-D CCD imaging system

The overall configuration of the system is similar to that of a transmission-mode imaging system with ZnTe crystals as transmitter and receiver. The only difference is that a cross polarizer (analyzer) is placed after the receiver. The electric field of the 2-D Terahertz beam would be converted to a 2-D

optical intensity modulated signal after passing through this analyzer. A digital CCD camera is installed at the back of the analyzer to record the optical image. [44]

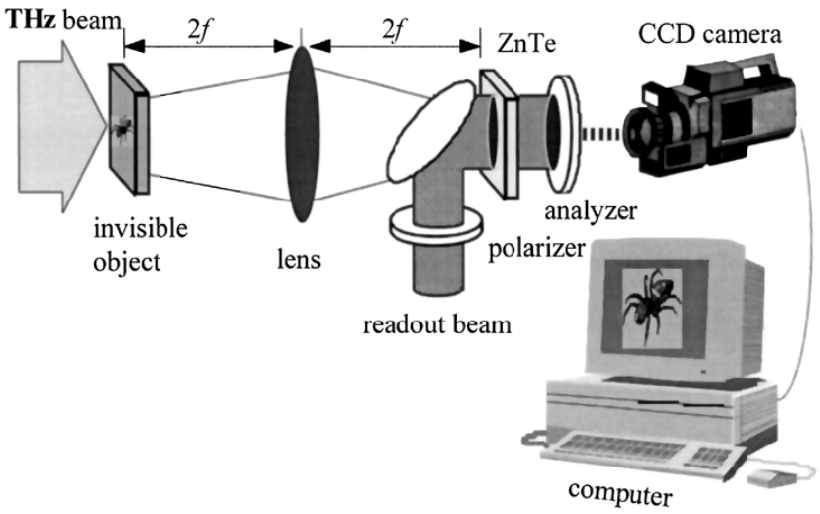


Fig. 2. 6 Detection with a CCD camera [44]

### 2.2.4 One-dimensional spatio-temporal imaging

In this method, the frequency of the probe beam is chirped using a grating pair so that the pulse duration would be stretched. When this chirped probe beam and the Terahertz beam reach the detector, due to the Pockels effect, different frequency components of the chirped pulse are modulated with different parts of the Terahertz signal, thus, resulting in a Terahertz output which has been encoded onto the spectrum of the probe beam. To measure the spectral distribution, a spectrometer and a CCD are used. Therefore, the whole spatio-temporal image can be taken with one shot using this method. [44]

### 2.2.5 Using photomixing as a continuous wave source in an imaging set-up

The source in this set-up is an external-cavity, two-line emission laser diode. The frequency difference between the two beams is adjusted by a V-shapes mirror. The two beams are then focused on a biased stripline dipole antenna where the THz narrowband signal is being generated. The THz beam is then focused on the sample and is then detected by a bolometer. In order to take the total image of the sample, the sample is raster scanned in two dimensions. [1]

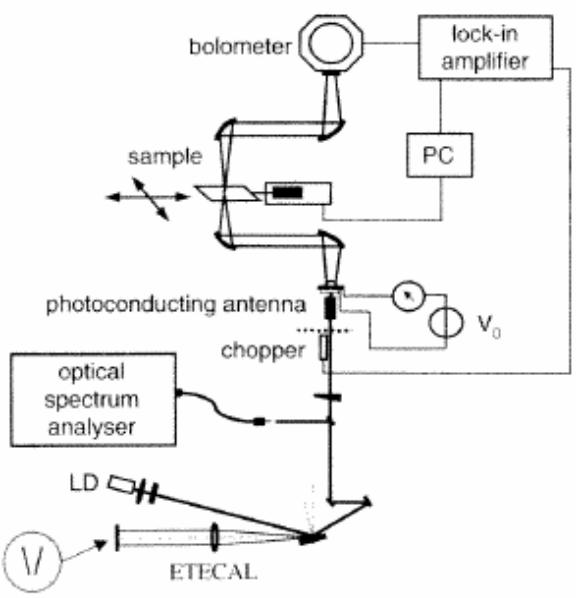


Fig. 2. 7 A CW THz imaging set-up with a laser-diode as the source and a bolometer as the detector [1]

### 2.2.6 Near-field probe: An application of a pulsed imaging set-up

In this probe, photoconductive antenna is used as transmitter and receiver. The transmitter photoconductive antenna is biased with an alternating square-wave voltage. The optical pulses are generated by a Ti-sapphire laser with 800 nm wavelength and a repetition rate of 100MHz. By using two off-axis parabolic mirrors, the THz beam, with a FWHM of approximately 2mm, is focused on the object which is much smaller than 2mm. In order to detect the THz beam, the detecting antenna is gated with a pulse from the same laser. By measuring the induced current through a lock-in amplifier, the Terahertz field can be calculated. The transmitter, receiver, optical elements and the object are all placed in a vapour-tight box purged with nitrogen to reduce the effects of water absorption. Note that an optical time delay can also be used if time-domain imaging is required. [15]

The aperture is a square hole of size 5-50μm made on a surface of a thin gold film. As shown in figure 2.7, the photoconductive antenna is designed between a thin layer of GaAs and a sapphire substrate. [15]

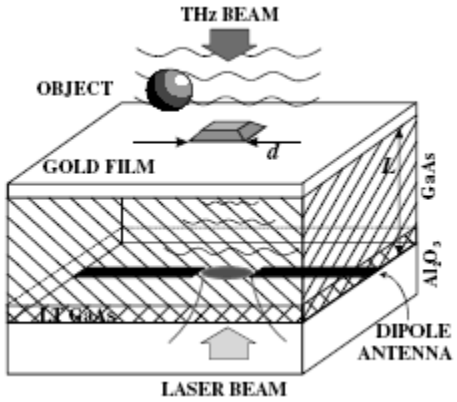


Fig. 2. 8 schematic of the near-field probe [15]

## 2.3 An overview of the application of Terahertz sources in medical imaging

Comparing to other imaging methods, Terahertz imaging is generally considered as a slow method because since Terahertz sources are costly, only one source is used in every set-up. For time-of-flight measurement with pulse set-up, this means that either the object or the detector must be moved on a stage for a complete scan which would be time-consuming. For CW source, however, a lens can be used to reshape the beam into a collimated beam with certain diameter larger than the object size and illuminate the object with that beam. An array of detectors can be used to take the image but this method would reduce the SNR.

The photonics based sources for THz generation are more ubiquitous in medical application due to their ability to generate broadband pulses over a wide range of frequencies as well as narrowband continuous wave around terahertz frequencies. Among this type of sources, lasers are less frequently used in medical application due to their size, cost and complexity while photomixing, photoconductive antenna and optical rectification are more often used, the former as a source for continuous wave around terahertz frequency and the two latter ones as broadband terahertz pulse generator. [21]

At this point, a comparison is made between the advantages and disadvantages of electro-optic and photoconductive methods of Terahertz generation and detection for imaging purposes which can be extended to medical imaging as well. Firstly, although PDA and electro-optics methods are used commonly in medical applications, they are both considered as expensive sources due to their need for a femtosecond pulse laser. [34]

Electro-optic emitters are characterized as low power emitters compared to photoconductive antennas. The output power in a photoconductive antenna increases by increasing the input pulse power or the bias voltage of the PDA. Electro-optic emitters are however, less limited in frequency compared to photoconductive antennas. The former can achieve up to 50THz while the latter's highest frequency is a few THz. Moreover, although the electro-optic detectors work at higher frequencies and they are easier to align than the photoconductive antennas, they have lower efficiency and are more vulnerable to noise. Using a lock-in amplifier can however cancel the laser noise (which is proportional to 1/f). [34]

Another major issue is that in an imaging set-up with an electro-optic detector, a CCD camera can be used which results in a faster imaging. From the other side, PDA detectors can be used in the form of an array to perform parallel processing and faster imaging. [34, 44]

The advantage of using electro-optic detector together with a CCD camera is that such system would be able to perform non-invasive imaging of moving objects or hidden objects. This detection configuration, although able to perform real-time imaging, has the disadvantage of recording merely one image per time delay. Moreover, as it isn't a phase sensitive method of detection, it reduces the signal to noise ratio. [34, 44]

## 2.4 Summary

In this chapter, electronics and photonics based sources of Terahertz radiation were introduced and it was mentioned that for medical imaging applications, the photonics based sources are favoured over the electronics based sources. The commonly used detectors for THz radiation detection were also specified. Moreover, examples of THz imaging set-ups in which some of the most ubiquitous sources and detectors, such as photoconductive antenna and nonlinear crystals had been used were mentioned. A near-field imaging probe was also introduced as an example for an up-to-date THz imaging set-up. Finally, the advantages and disadvantages of the most commonly used sources and detectors in THz imaging set-ups were pointed out.

# Chapter 3
# A review on the characteristics of Terahertz wave and the application in medical imaging

This chapter talks about the characteristics of THz waves, their interaction with tissue and their potential to be used in medical application. Some safety issues concerning the exposure to this range of frequency are also mentioned. Moreover, instances of research done so far on THz imaging of different biological samples are discussed and their results are demonstrated.

## 3.1 Characteristics of Terahertz waves

This section is an overview of the main characteristics of Terahertz radiation which makes it unique for certain applications. Moreover, a brief summary of the applications of Terahertz in medical imaging and spectroscopy has been given. More details about the works done in these fields by different research groups will be mentioned in 3.2.

### 3.1.1 Interaction of Terahertz waves with tissues

In Terahertz range of frequencies, the energies are of the order of discrete molecular vibrational, torsional and librational modes in solids and liquids. So, by using the Terahertz pulsed spectroscopy and Terahertz imaging, the torsional and vibrational motions in the molecules or between the molecules are detected. These motions can be the flexing of a molecule or intermolecular interactions due to their strong hydrogen bonds or other Van Der Waals forces. Therefore, polar molecules like water that have hydrogen bonds between molecules have an absorption peak at certain frequencies along the Terahertz range. For water, one of the absorption peaks occurs at 5.6 THz. Moreover, some materials (for example some constituents of tissues) are said to have “fingerprint” in this range of frequency which means that they have peak absorption at a certain frequency in this range and thus can be detected. Examples of such materials are DNA and proteins. Therefore, this range of frequency can give us a good deal of spectroscopic information. [18, 20, 28, 33]

Figure 3.1 shows the molecular transitions in the Terahertz as well as other frequencies along the electromagnetic range of spectrum.

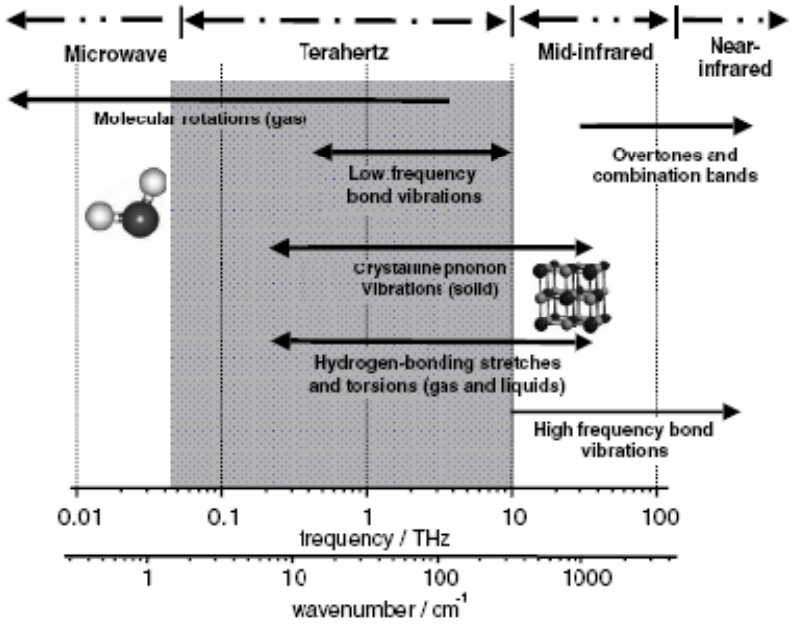


Fig 3. 1 The molecular transitions in the electromagnetic range of spectrum, [28]

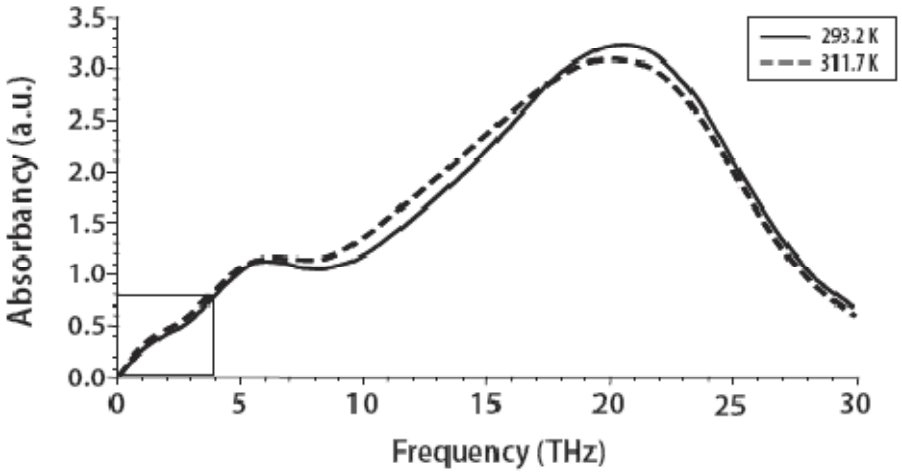


Fig 3. 2 The graph of water absorption at different frequencies, [30]

Another advantage of working in this range of frequency is that Rayleigh scattering in the tissues, which is the dominant scattering at IR and optical frequencies, is weak at Terahertz frequencies. Note that Rayleigh scattering occurs when the wavelength of the wave is comparable to the cell size and is

of order of $f^4$. The dominant scattering around Terahertz frequencies is proportional to $f^2$ (known as Mie and Tyndall scattering). [18, 30]

### 3.1.2 Safety concerns

According to the literature [18], the energy transmitted to the tissues at Terahertz frequencies is around 1 to 12 meV. At these orders of energy, strong resonant absorption in the tissues is less likely and the tissues would mostly be affected by generalized thermal effects which is much less harmful than the effects of resonant absorption. Moreover, Unlike X-ray, Terahertz doesn't have ionizing hazard for the biological tissues due to its location along the frequency spectrum.

The safety level for pulsed electromagnetic radiation is defined by a parameter called the maximum permissible exposure (MPE). MPE is calculated by using the following formula:

$$MPE_{PW} = \frac{A.MPE_{CW}}{F.t} \tag{3.1}$$

$A$ : Area of incident beam,

$MPE_{CW}$ : Maximum possible exposure for the continuous wave,

$F$ : Pulse repetition rate,

t : duration of a single pulse.

Then, in order to know the permissible power for each pulse, we need to know the total number of pulses during the exposure time (T) which we show with N.

As an example, we assume a typical laser source with 82 MHz repetition rate, 0.1ps pulse duration and a circular beam of 1mm diameter. Generally, the maximum possible exposure for the continuous wave for an area of 0.01m² is W/ m². If we assume that the total exposure time is 600s, then the limit for the power per pulse would be equal to 94W. The usual value of power of photoconductive or electro-optic Terahertz sources is about 1µm and even with amplification, this value can reach 1mW which is well below the safety limit. [26]

The only issue is that these formulas are derived for sources with larger wavelength and higher pulse duration which may not hold for Terahertz. Moreover, due to high water absorption at Terahertz range of frequency, more severe damages may occur to the body cells. [26]

Biological effects of exposure to THz and safety issues concerning THz radiation have been studied in the THZ-BRIDGE project[49] during 2001 to 2004. One of the most important results of this research was that damage to Lymphocytes occurs under certain THz exposure parameters. However, they have confirmed that using the appropriate exposure parameters is certainly harmless for single exposures to THz radiation. [40, 49]

Further hazard of the THz radiation on biological tissues is still under investigation.

### 3.1.3 An overview of the applications of Terahertz in medical imaging

Apart from the possibility of spectroscopic measurements in Terahertz frequencies due to the fingerprint of certain molecules, there are other certain applications which are mostly based on the possibility of coherent detection of pulsed Terahertz signal. This means that the amplitude and phase of the terahertz electric field can be detected at the same time which provides a great opportunity for depth detection.

Due to strong absorption of Terahertz radiation by the biologic tissues, Terahertz is suitable for near-surface imaging such as epithelial cancer; including breast, skin and colon cancer. It has been reported that a Terahertz pulse with an SNR equal to 500:1 can penetrate 1.5mm inside the skin. According to this property of Terahertz waves, in vivo imaging can only be done with a reflection-mode imaging system. Therefore, for in vivo imaging, the transmission-mode THz imaging systems cannot be used yet, due to the small depth of penetration of current THz sources. However, for prepared, in vitro tissue samples, both reflection and transmission-mode imaging can be used. [20, 21]

Consequently, spectroscopic characteristics of tissues and water absorption at Terahertz, together with the possibility of coherent detection makes Terahertz eligible for certain medical imaging applications. The most promising of these applications which have been repeated in the literature are as follows:

1. To locate Basal cell carcinoma (BCC), which is known as cancer of the lowest layer of the epidermis and is one of the most common forms of skin cancer, and give information about their size and shape. This results in less time-consuming and more efficient and precise surgeries for excising the tumour, due to the ability of the Terahertz wave to differentiate healthy cells from cancerous cells. The ability of Terahertz wave to differentiate healthy cells from cancerous cells is believed to be because of the difference in the water content of these two types of cells. [28, 30]

2. Evaluating the skin condition to reveal the hydration profile and properties of skin before and after using topical therapies to verify the effect of such therapies. In this application, THz spectroscopy and the sensitivity of the THz wave to water concentration of the tissue play an important role.[30]

3. Early detection of tooth caries due to the ability of Terahertz to differentiate between dentine, enamel and also various levels of calcification of the tooth. Generally, formation of caries starts with decalcification beneath the surface of the enamel and may grow into the dentine while no change may occur at the enamel's outer surface. The primary level of decalcification is a reversible process and can be avoided if detected early enough. This application, however, may need some time to become feasible due to lack of probe technology for imaging inside the mouth at THz frequencies and due to problems such as high water absorption and scattering inside the mouth.[13, 14, 29, 30, 31]

4. Since non-polar materials such as bandages and other wound dressings are transparent to Terahertz radiation, Terahertz can be used to monitor the healing process of the wound without the need for the dressings to be removed. Especially, in the last phase of wound healing which is the contraction of the wound, Terahertz can be of a great help. Currently used methods do not differentiate between wounds that heal with or without scar tissue formation while Terahertz is believed to be able to differentiate between these two types of scars and thus help the doctors to prescribe the medication needed for prohibiting the scar formation. [27, 30]

5. Diagnostic of depth and severity of skin burnings. THz spectroscopy and THz' sensitivity to water concentration are playing the major role in this application too. [1, 30]

## 3.2 A review on the works done on characterization of THz imaging set-ups and THz medical imaging

In this section a review is presented on the research and experiments that have been done on finding the imaging parameters of some THz imaging set-ups and also on THz medical imaging. A description is provided in each case about the methods that have been used and the results of the experiments. Before talking about these carried out experiments, a brief introduction into the meaning of resolution and how it is limited from an optical point of view is presented.

### 3.2.1 How do we define resolution in an optical imaging system?

In this section we go through the optical phenomena which confine the resolution of an imaging system, the most important of which is the diffraction. Therefore, first, a review on the definition of diffraction from physics and mathematics point of view is provided followed by the definition of Airy disk which is a common example of diffraction in systems that have a circular aperture. Afterwards, aberration is also mentioned as one of the resolution limiting factors in imaging set-ups. In the end, a number of recently used methods for obtaining sub-diffraction-limit resolution are introduced.

#### 3.2.1.1 Diffraction

Ideal imaging systems are those which are diffraction-limited. In these systems, the spherical wave generated from a point source would be reconverted to a converging spherical wave which converges towards a point in the image plane, by the imaging system.

Diffraction happens when a beam encounters an obstacle or an opening with dimensions comparable to the wavelength of the beam. The bending of the beam around the obstacle or the spreading of its lateral contents is regarded as diffraction. [2, 3]

##### 3.2.1.1.1 Kirchhoff's formulation for diffraction

The discovery of this phenomenon dates back to 1665. Since then, many scientists tried to find physical explanation and mathematical formulation for diffraction. One of the first approximations for diffraction was derived by Kirchhoff. In this approximation as well as many others which were introduced after Kirchhoff, Green function plays an important role. In his approximation, Kirchhoff defined the Green function at an arbitrary point $P_1$ as $G(P_1) = \frac{\exp(jkr_{01})}{r_{01}}$ (3.2) which is a spherical wave propagating from the point of observation $P_0$ and using the Green's theorem, he derived the following equation for the optical disturbance at point $P_0$ in terms of the boundary values of the wave at a closed surface around $P_0$. [3]

$$U(P_0) = \frac{1}{4\pi}\iint_S \left\{ \frac{\partial U}{\partial n}\left[\frac{\exp(jkr_{01})}{r_{01}}\right] - U\frac{\partial}{\partial n}\left[\frac{\exp(jkr_{01})}{r_{01}}\right]\right\} ds \qquad (3.3)$$

Where $r_{01}$ is the displacement vector connecting $P_0$ to $P_1$ and *n* is the outward normal direction to the surface S.

By choosing another form of Green function, the Rayleigh-Sommerfield diffraction formulation was derived as below. Note that this equations holds for the cases where $r_{01} >> \lambda$ . This formula has been used to calculate a number of diffraction approximations.

$$U(P_0) = \frac{1}{j\lambda} \iint_{\substack{within\\ aperture's\\ surface}} U(P_1) \frac{\exp(jkr_{01})}{r_{01}} \cos(\vec{n}, \vec{r}_{01}) ds \tag{3.4}$$

Other diffraction formulas have also been introduced by defining different Green functions or making simplifying approximations. Two of the most common approximations are the Fresnel and Fraunhofer diffraction equations which are discussed in 3.2.1.1.2 and 3.2.1.1.3. [3]

3.2.1.1.2 Fresnel diffraction approximation

Equation 3.4 can be rewritten in the rectangular coordinates according to figure 3.3 as below:

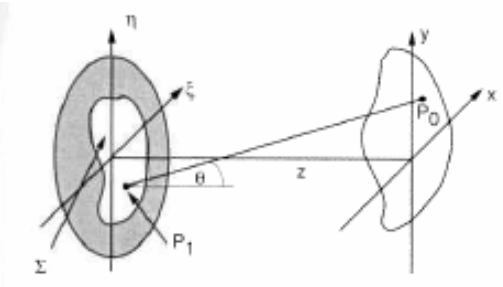


Fig 3. 3 A schematic of the aperture coordinates and observation point coordinates [3]

$$U(P_0) = \frac{1}{j\lambda} \iint_{\substack{within\\ aperture's\\ surface}} U(P_1) \frac{\exp(jkr_{01})}{r_{01}} \cos\theta . ds \tag{3.5}$$

By substituting the value of $\cos\theta$ and the position vectors with the parameters from figure 3.3, we can write equation 3.5 as:

$$U(x,y) = \frac{z}{j\lambda} \iint_{\substack{within\\ aperture's\\ surface}} U(\xi,\eta) \frac{\exp(jkr_{01})}{r_{01}^{\,2}} d\xi d\eta \tag{3.6}$$

Where $r_{01} = \sqrt{z^2 + (x-\xi)^2 + (y-\eta)^2}$ .

In Fresnel approximation, we rewrite $r_{01}$ as $z\sqrt{1 + (\frac{x-\xi}{z})^2 + (\frac{y-\eta}{z})^2}$ and by assuming that the second and third terms under the square root are much smaller than 1, the binomial expansion was used to rewrite $r_{01}$ as $z\left[1 + \frac{1}{2}(\frac{x-\xi}{z})^2 + \frac{1}{2}(\frac{y-\eta}{z})^2\right]$. Thus, the diffraction approximation can be rewritten in the following form:

$$U(x,y) = \frac{e^{jkz}}{j\lambda z} e^{j\frac{k}{2z}(x^2+y^2)} \int_{-\infty}^{\infty} \left\{ U(\xi,\eta) e^{j\frac{k}{2z}(\xi^2+\eta^2)} \right\} e^{-j\frac{2\pi}{\lambda z}(x\xi+y\eta)} d\xi d\eta \tag{3.7}$$

Equation 3.7 is known as the Fresnel diffraction integral. The term inside the integral can be regarded as the Fourier transform of the complex field right after the aperture multiplied by a quadratic phase factor. [3]

The final point that has to be reminded about the Fresnel approximation is that in order for this approximation to be valid, the third and higher terms of the binomial expansion of $r_{01}$ must be much less than unity. This imposes the following condition on the coordinates of the aperture and observing point [3]:

$$z^3 >> \frac{\pi}{4\lambda}\left[(x-\xi)^2 + (y-\eta)^2\right]^2_{\max} \tag{3.8}$$

3.2.1.1.3 Fraunhofer approximation

This approximation can be regarded as a special case of Fresnel approximation. The main assumption here is that the quadratic phase factor of the term under the integral of equation 3.7 equals unity. This condition requires that:

$$z >> \frac{k(\xi^2 + \eta^2)_{\max}}{2} \tag{3.9}$$

Or from antenna point of view, this condition is shown as $z > \frac{2D^2}{\lambda}$, where D is the dimension of the aperture.

Therefore, the diffraction approximation at the Fraunhoffer region can be written as:

$$U(x,y) = \frac{e^{jkz}}{j\lambda z} e^{j\frac{k}{2z}(x^2+y^2)} \int_{-\infty}^{\infty}\int U(\xi,\eta) e^{-j\frac{2\pi}{\lambda z}(x\xi+y\eta)} d\xi d\eta \tag{3.10}$$

Note that Fraunhofer region is also called as far-field region while Fresnel region is called as near-field region [3].

3.2.1.1.4 An example of Fraunhofer diffraction pattern for a circular aperture

Using equation 3.10 to find the diffraction equation for a circular aperture, we derive the following equation:

$$U(r) = \frac{e^{jkz}}{j\lambda z} e^{j\frac{k}{2z}r^2} B(U(q))\Big|_{\rho = r/\lambda z} \tag{3.11}$$

Where $q = \sqrt{\xi^2 + \eta^2}$ is the radius in aperture plane and $\rho = \sqrt{f_x^2 + f_y^2}$ is the radius in spatial frequency domain and *B* represents the Bessel function which can be shown as below:

$$B\left(circ\left(\frac{q}{w}\right)\right) = A\frac{J_1(2\pi w\rho)}{\pi w\rho} \tag{3.12}$$

Therefore, by using equations 3.11 and 3.12 we can write the intensity distribution after the aperture as:

$$I(r) = \left(\frac{A}{\lambda z}\right)^2 \left(2\frac{J_1(2\pi w\rho)}{\pi w\rho}\right)^2 \tag{3.13}$$

Therefore, for a diffraction-limited system including a circular aperture, the image of a point source would have the shape of Bessel function and is called the Airy disk. The radius of the main lobe of the Airy disk represents the limit of the resolution for such system. This radius can be calculated from the following equation:

$$r = 1.22\frac{\lambda z}{D} \tag{3.14}$$

Where $z$ is the distance between the aperture and the image plane and $D$ is the size of aperture.

Note that the resolution of a diffraction-limited imaging system is also equal to the radius of Airy disk.

An important that must be reminded here, is that the size and distance in equation 3.14 must satisfy a certain condition in order for the diffraction approximation to be valid. Therefore, we cannot declare that equation 3.14 results in an infinite resolution if we increase D to a great extent. Because then, due to equation 3.14, z must also be increased so that the Fraunhoffer approximation holds and that avoids resolution to become infinity [2, 3, 6].

Therefore, we can see that diffraction sets limits on the resolution; however, new methods have been introduced in order to achieve sub-diffraction-limit resolution. These methods are discussed in 3.2.1.3.

#### 3.2.1.2 Aberration

A common effect which is present in many imaging systems is called aberration. Aberrations happen when the beam deviates from being ideally spherical. Such deviations can occur because of different factors such as some properties of the aperture or even a perfectly spherical lens while they can also occur because of misalignment of the imaging set-up. In such case, a complex amplitude transfer function is defined for the aperture in which a phase-shifting term is present and takes care of the phase deviations from the ideal spherical wave. The transfer function of the imaging system for a system with aberrations is the complex amplitude transfer function of the aperture multiplied by the Fraunhofer diffraction pattern. Therefore, the real amplitude of the incident beam doesn't change comparing to the diffraction-limited case, while, a phase distortion occurs in the pass band of the transfer function of the system with aberrations. Aberrations can have a negative effect on the MTF and the resolution of an optical imaging system to a great extent. Therefore, the imaging resolution of a set-up can be gravely reduced when it suffers from aberrations comparing to when it is diffraction-limited. A simple equation cannot be derived for the resolution limit of an imaging system suffering

from aberrations; however, there are equations which can be used to find out the point spread function of the system when the complex amplitude transfer function of the aperture is known [3].

#### 3.2.1.3 Approaching resolutions better than the diffraction limit

Recently, some techniques have been used in order to enhance the resolution of imaging systems up to more than the diffraction limit. Some of these techniques are based on image processing techniques and are called super-resolution (SR) techniques, an example of which is extrapolation of low-resolution images by assuming them as analytic functions. Near-field imaging with certain apertures in order to detect the evanescent field, which is mentioned in section 2.2.6, is another technique for obtaining resolutions below the diffraction-limit [3, 15].

The most controversial of all, however, is the concept of using materials with negative permittivity or permeability such as metamaterials for manufacturing lenses in imaging set-ups. In this case, the loss of evanescent field can be compensated, resulting in capturing details beyond the diffraction limit of the system [38].

### 3.2.2 Works done on finding the imaging parameters of THz imaging set-ups

In this section, the experiments that have been done by different research groups on finding the imaging parameters of some THz imaging set-ups are introduced. The result of each of the measurements are shown and analyzed. Moreover, a discussion on the trade-off between different imaging parameters of the set-up is stated.

#### 3.2.2.1 Resolution

The results obtained from [26] and [29] shows that generally, the lateral resolution in a Terahertz pulse imaging system depends on the diffraction limited beam waist of the Terahertz signal except for near-field imaging system which depends only on the dimensions of the aperture. Moreover, the depth resolution is a function of the bandwidth of the Terahertz signal. [26, 29]

One of the methods used to obtain higher resolution was to perform near-field imaging. In this method, an aperture, which is smaller than the diffraction limit of the Terahertz wave, is put between the source and the object. In order to satisfy the near-field condition, the distance between the aperture and the object must be of the same order of the wavelength. By applying this method, the resolution has been reduced to ten times less than before. This, however, has been achieved by the expense of losing the SNR. Spatial resolutions of 39μm for a 30μm aperture and 7μm for a 5μm aperture have been reported. Meanwhile, the SNR has reduced by a factor of $d^3$ for an aperture of dimension $d$. [26]

A method that has been used to determine the spatial resolution of a Terahertz imaging system (as well as for any other imaging system) is to implement a phantom object by depositing some strips of gold with different widths on a material transparent to Terahertz and then measuring the transmission of signal along the line of strips of different lengths. [26, 29]

Fig 3. 4 Phantom sample used for finding resolution [26]

In a research done by scientists at the University of Leeds, UK and Geothe-Universitat, Germany, the same phantom sample has been designed with strips of width 0.5 to 4 mm. The time-domain image of each set of these lines has been taken with a time pulse imaging system by collecting 32 points at an interval of 0.1 ps. Then, this data was Fourier transformed and the relative transmittance image was formed for frequencies of 0.62, 1.25, 1.87 and 2 THz. Then, the graph of the amount of transmitted power through different strips for different frequencies was plotted, which is called modulation transfer function (MTF) and the spatial resolution of the system was determined from this graph. The result of this measurement is shown in figure 3.5. [29]

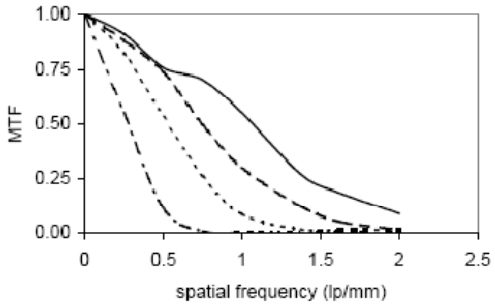


Fig 3. 5 The modulation transfer function at 0.62THz (dash-dot-line), 1.25THz (dotted line) and 2.5 THz (solid line). [29]

### 3.2.2.2 Imaging a step wedge for noise characteristics

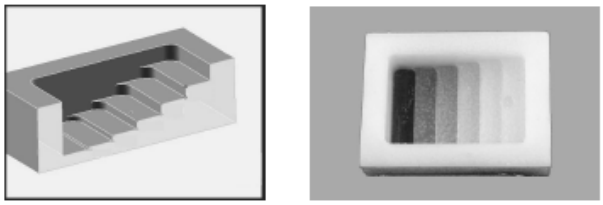

Fig 3. 6 Diagram of a step wedge made from Duraform polyamide for measuring the noise of the Terahertz pulse imaging system. [29]

In this work, a wedge was made out of Duraform polyamide with six different thickness steps. The values of thickness were 0.1mm, 0.5mm, 1.5mm, 3mm, 5mm and 7mm. At each pixel, 128 data points were collected, with 0.15ps interval between each two data, by a time-domain pulse imaging system. The images were then Fourier transformed and the image at certain frequencies was then extracted for a number of parameters such as relative transmittance, time delay, absorbance and dual frequency. In order to generate the relative transmittance, time delay and absorbance images at a certain frequency, they calculated the transmitted to incident power, phase component of the Fourier transform and logarithm of the inverse of relative transmittance, respectively. To measure the dual frequency, the following formula has been used:

$$DF(f_i) = \frac{RT(f_i) - RT(f_i + 5\Delta f)}{RT(f_i) + RT(f_i + 5\Delta f)} \tag{3.15}$$

Where *RT(f)*is the relative transmittance at frequency *f* [29].
Figure 3.7 shows these parametric images.

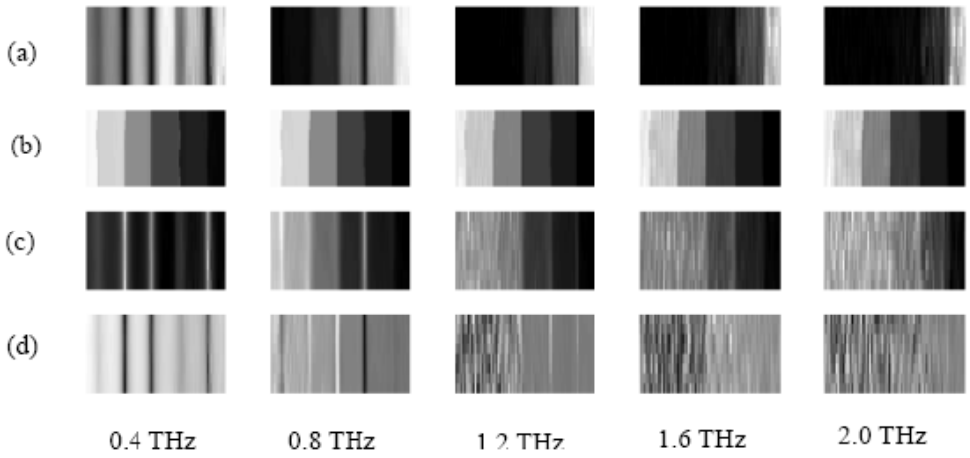


Fig 3. 7 Parametric images of the step wedge. (a) relative transmittance, (b) time delay, (c) absorbance and (d) dual frequency for five different frequencies. The thicknesses of the steps are 0.1, 0.5, 1.5, 3, 5, 7mm from right to left. [29]

The following figure illustrates the difference in the mean value, standard deviation and noise of these images for three different thicknesses of the wedge.

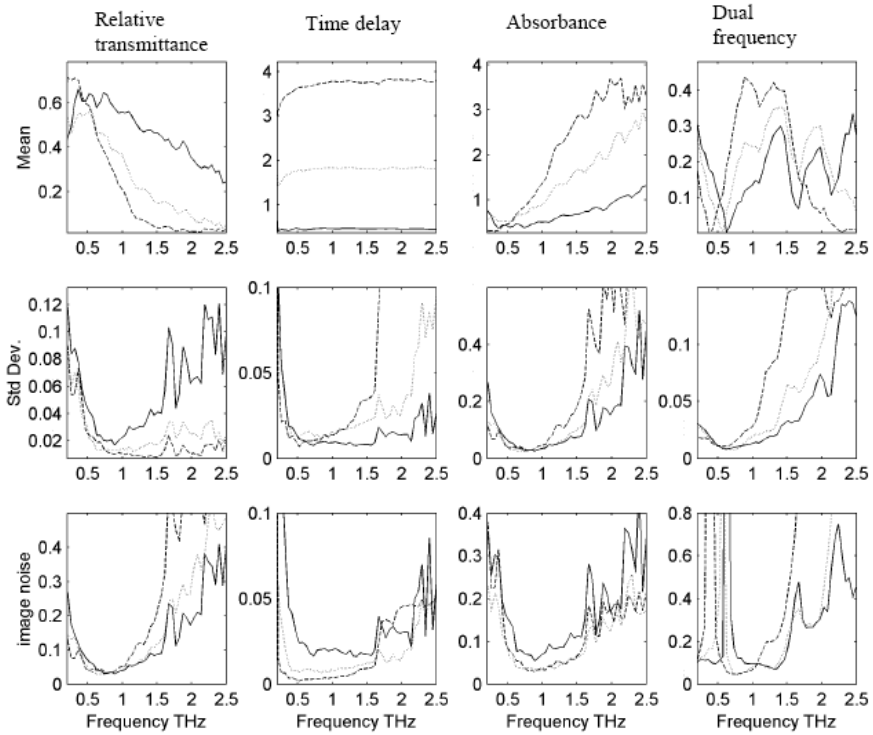


Fig 3. 8 Mean, standard deviation and image noise of the parametric Terahertz images of the step wedge. [29]

According to these results, the noise in absorption images is higher at larger frequencies and for higher thicknesses. Moreover, the noise has mostly affected the magnitude-related parameters such as relative transmittance, absorbance and dual frequency, while time delay images are affected by less noise at higher frequencies. Another fact is that the dual frequency images are noisier than other parametric images. The reason is that the absorption coefficient of Duraform polyamide increases with frequency and as shown in the first relative transmission image, because of the same reason, the transmittance decreases at higher frequencies. Therefore, in equation 3.2, the second term of the nominator and denominator would decrease to a great extant while the first term is relatively large and this increases the whole ratio. [29]

#### 3.2.2.3 Trade-offs between scan time, SNR and bandwidth to reduce the acquisition time

One of the most important issues of THz imaging is to decrease the acquisition time while keeping the SNR and bandwidth as high as possible. Some works have been done by different groups on optimizing these parameters, which are mentioned here.

A common method to reduce the acquisition time is to use multi-array detectors; which would be at the cost of decrease in the SNR because of the decrease in the signal that each pixel receives. Another trade-off for decreasing the data acquisition time would be losing the bandwidth. Mittleman et al. [43] proposed a delay line which oscillated at 100 Hz frequency and can reduce the acquisition time from a few minutes up to 25μs. This would however, decrease the noise filtering capabilities of the system and would result in SNR reduction. Note that source of noise in a Terahertz imaging system is the fluctuations of the laser and the detectors' Johnson noise. The acquisition time of an imaging system using a CCD camera as detector has been reported to be 25 ms. In another system which has gained acquisition time of about a few milliseconds at the expense of lower spectral resolution and reduced SNR, a chirped laser pulse has been used instead of a mechanical delay line [26].

In order to recover the lost SNR in these systems, averaging methods can be used, but it has been proved that the time required for averaging in the fast systems is comparable to the acquisition time needed in slower systems. [26]

### 3.2.3 Works done on THz medical imaging

In this section, a number of works that have been done in the field of Terahertz medical imaging are introduced. The first example (water content of a leaf), mentioned in 3.2.3.1, is however, unrelated to medical imaging; but since it was one of the first Terahertz images taken from a living sample, I considered it as a valuable example to mention in this section. Before going through these examples,

an introduction into parametric THz imaging is stated in the following paragraph in order to give a vision on the different parameters of THz images that are of interest to different THz medical imaging cases.

According to the application, different image parameters can be examined in Terahertz images, each of which reveals certain information about the object. These parameters are usually categorized into two groups: Time-domain parameters and frequency-domain parameters.

Examples of time-domain parameters are pulse amplitude, pulse time delay, pulse width and instantaneous electric field. By looking at the pulse amplitude we can determine the portion of the transmitted Terahertz signal at each pixel while the time delay of the pulse reveals information about the thickness and refractive index of the object. Measuring the pulse width would tell us about the object's absorption profile for different frequencies. Finally, in order to have the instantaneous electric field, we need to measure the amplitude of the electric field at different times, which would determine the propagation of the field through the object.

The most commonly used frequency domain parameters are transmittance (or absorbance), time delay, dual frequency, dispersion and thickness-independent parameters. Transmittance (absorbance) would give us the amount of the transmitted (absorbed) wave at a certain frequency. Similar to the time-domain case, the time delay measurement in the frequency-domain would reveal information about the thickness and refractive index of the object. Dual frequency parameters show the ratio of a certain parameter at two different frequencies. Dispersion-related parameters measure the change in transmittance with respect to frequency. The thickness-independent parameters can be in different forms; however, one of the most common forms is:

$$\frac{\alpha(f)}{(n(f)-1)} \tag{3.16}$$

In which dividing the value of absorption coefficient by the real refractive index would cancel out the thickness dependence. Thus calculating this value together with measuring the time delay would give us information about the refractive index of the object.

### 3.2.3.1 Water absorption profile of a leaf [22]

Figure 3.9 has been taken with a pulsed Terahertz imaging source by Hu and Nuss and is considered as one of the Terahertz images. In this image, only the magnitude of the Terahertz signal has been detected at each pixel and no phase information has been extracted.

The leaf shown on left is a freshly cut leaf as can be recognized by its high attenuation of Terahertz radiation due to high concentration of water. The image on right, however, shows the same leaf 48 hours later which except for its stems has lost all its water.

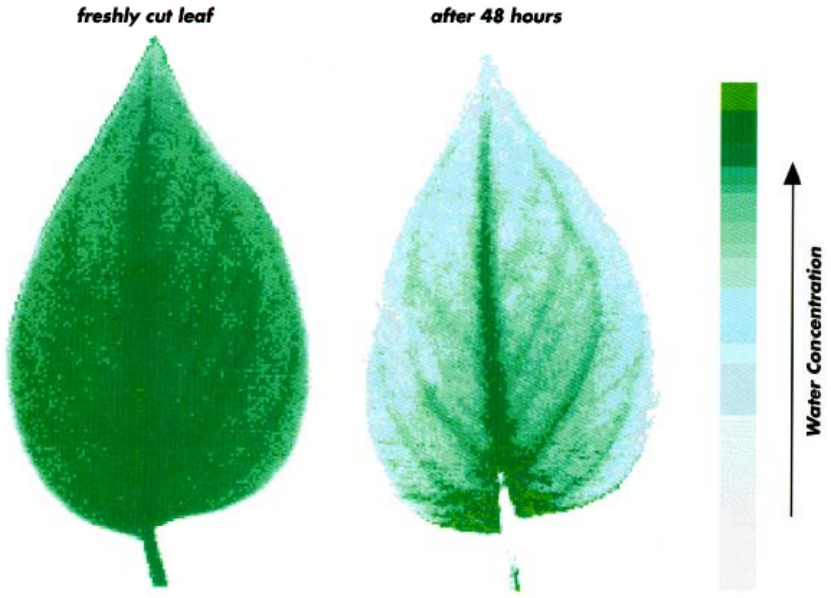


Fig 3. 9 Water absorption profile of a (left) freshly cut leaf and (right) the same leaf after 48 hours. [22]

### 3.2.3.2 Imaging of a pig's larynx sample [1]

In a research by Koch [1], Terahertz image of a larynx sample from a pig and a liver sample of human has been taken. The size of these prepared samples was 67 by 42 by 7mm and 50 by 40 by 4mm respectively. These samples were put in a formalin solution in order to fix the protein structure. Then, some solutions were used to dehydrate them and they were finally put in paraffin wax.

Figure 3.10 shows three different images of the larynx sample. The first is an optical image and the next two are Terahertz time-domain images taken at two different frequency windows. As we can see in figure 3.10(a), the difference between the soft tissue and cartilage is hardly distinguishable. In

figure 3.10 (b) which is imaged using a frequency window from 1 THz to 1.5 THz, the same problem exists. In figure 3.10 (c), however, the difference between the soft tissue and cartilage is recognizable with dark areas showing high absorption corresponding to cartilage and bright areas showing high transmission corresponding to soft tissue (in the middle) and wax (at the surrounding). This image has been taken using a window frequency from 0.2 THz to 0.5 THz.

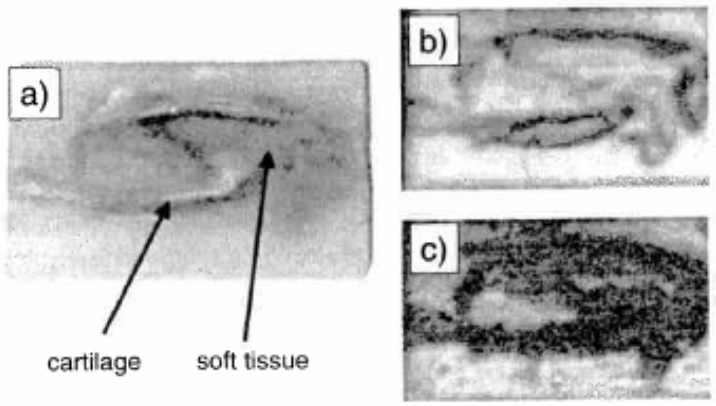


Fig 3. 10 Image of a pig's larynx sample; (a) Optical image, (b) THz transmission image in frequency window of 1 to 1.5 THz, (c) THz transmission image in frequency window of 0.2 to 0.5 THz [1]

In order to understand the reason for the high contrast in the lower frequency window, we must observe the absorption profile of soft tissue and cartilage at different frequencies. As shown in figure 3.11, the difference in absorption of soft tissue and cartilage is higher for frequencies of about 0.2 to 0.5 THz resulting in higher contrast in the images taken around these frequencies.

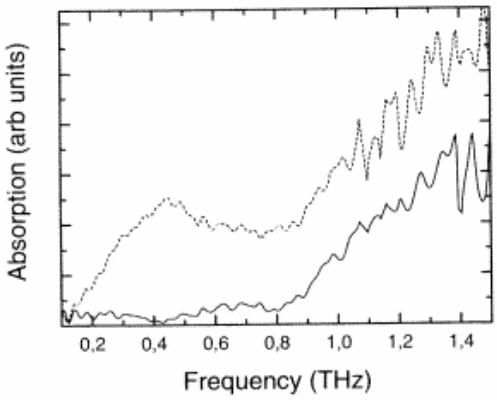


Fig 3. 11 Absorption profile of soft tissue (full line) and cartilage tissue (dashed line) [1]

### 3.2.3.3 Imaging a human liver sample [1]

Figure 3.12 shows the images taken from human liver. The first figure is the optical image. Figure 3.12 (b) has been imaged using a frequency window from 0.2 to 0.5 THz. We can see the high contrast between the regular liver tissue (brighter regions) and the metastasis (darker regions). This difference the absorption of healthy and cancerous tissue can be because of either change in density or change in chemical composition. It is reported that the densities of the two types of tissues are believed to be the same therefore the contrast is more likely to be because of the change in chemical contents.

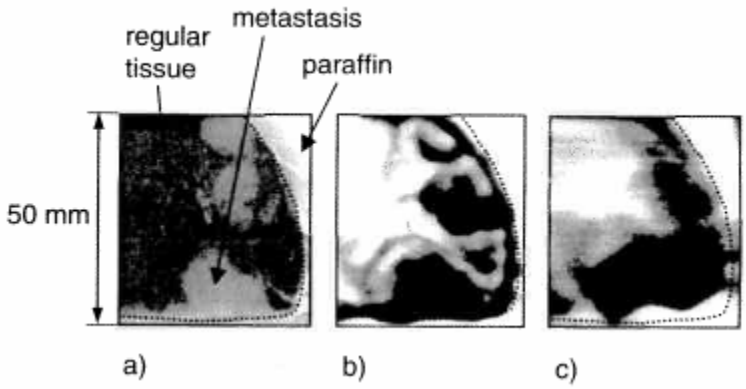


Fig 3. 12 Image of a cancerous liver sample of a human; (a) Optical image, (b) THz transmission image in frequency window of 0.2 to 0.5 THz, (c) THz transmission image at 230 GHz [1]

Figure 3.12 (c) is imaged at 230 GHz with the continuous wave Terahertz source introduced in section 2.2.5. Although the contrast between the regular tissue and metastasis is almost the same as figure 3.12(b) but the image has been degraded due to decrease in the value of frequency components of the Terahertz wave.

### 3.2.3.4 Imaging of an in vitro melanoma sample [26]

Melanoma is one of the rare types of skin cancer. In a Terahertz imaging research, different parameters of an in vitro melanoma sample was imaged which are shown in figure 3.13. The first two transmission images are taken at 0.5 THz and 2 THz respectively and the last one is the transmission at 1 THz relative to transmission at 1.5 THz, which shows the higher absorption by the tumour at larger frequencies. The phase angle image at 1 THz is shown in figure 3.13(c) which shows the difference in refractive index and thickness of the tumour and its surrounding tissues. A thickness-independent demonstration of the tumour is shown in figure 3.13(d), which shows the ratio

$\alpha(f)/(n(f)-1)$. Figure 3.13 (e) is a dispersion image at 1THz which shows the change of transmission from the tumour to the surrounding tissue.

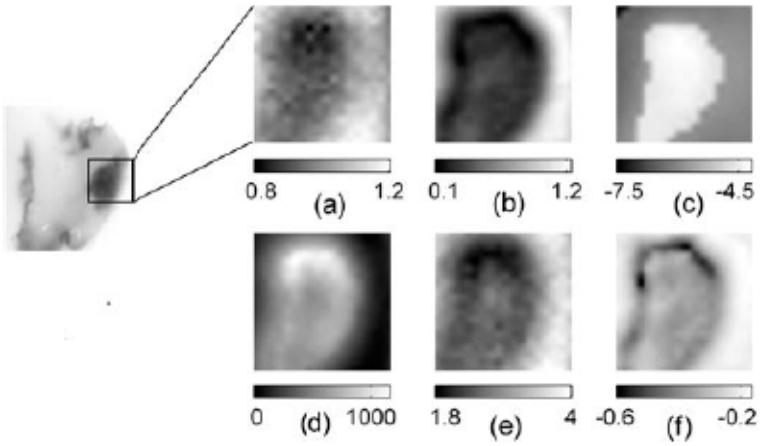


Fig 3. 13 Parametric Terahertz images of an in vitro melanoma sample. (a) Transmittance at 0.5THz, (b) Transmittance at 2THz, (c) phase angle at 1THz, (d) $\boldsymbol{\alpha(f)/(n(f)-1)}$, (e) dispersion at 1 THz, (f) Dual frequency image (transmittance at 1THz relative to transmittance at 1.5THz). [26]

### 3.2.3.5 Terahertz imaging for burn diagnostics [1]

In order to verify the capability of Terahertz pulse imaging for burn diagnostics, a chicken breast sample is burnt with an argon ion laser. A terahertz reflection image (figure 3.14) has been taken with a Terahertz pulse system. The figure shows minimum reflection at the center where the burn is most severe and the surrounding contours with different greyscale levels, each correspond to a certain amount of damage to the tissues.

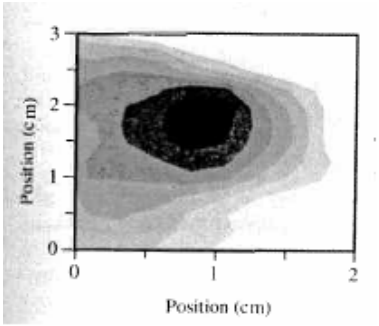


Fig 3. 14 The burnt chicken tissue sample [1]

Figure 3.15 shows a series of Terahertz pulses each taken at a point of the sample. These points are located at 250μm distance from one another. The pulse at the center which corresponds to the center of the burnt is the most distorted one.

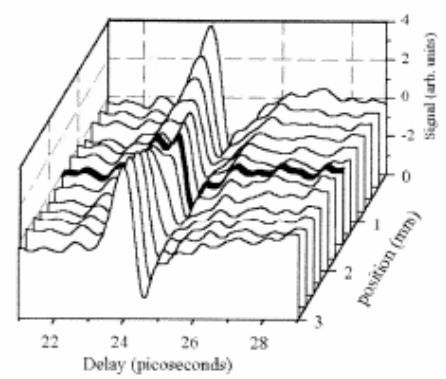


Fig 3. 15 The reflected pulse from different points of the burnt chicken tissue showed in figure 3.14. The pulse being reflected from the center of burnt is shown in black [1]

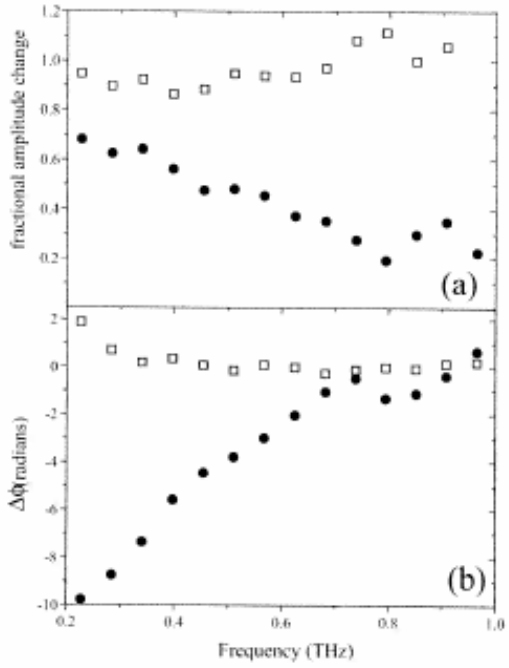


Fig 3. 16 The graphs of the (a) fractional amplitude. The squares show the amplitude measured at one edge (the healthy tissue) of the sample relative to the other edge (a healthy tissue as well) and the circles show the amplitude measured at one edge (the healthy tissue) of the sample relative to the amplitude measured at the center of the burnt and (b) phase difference. The squares show the phase difference between one edge (the healthy tissue) of the sample relative and the other edge (a healthy tissue as well) and the circles show the phase difference between one edge (the healthy tissue) of the sample and the center of the burnt [1]

Figure 3.16 shows the relative amplitude and phase (dark circles) of the central pulse, which passes through the center of the burn, to the pulse passing through the surrounding healthy tissue. The empty squares correspond to the amplitude (figure 3.16(a)) and phase (figure 3.16 (b)) of the pulse passing through the healthy tissue.

By comparing the circles and squares in figure 3.16(a), we see that the amplitude has decreased at the location of burning, with more decrease at higher frequencies which is because of increase in noise at higher frequencies. In figure 3.16(b), especially at lower frequencies, we can see a noticeable difference between the phase of the reference pulse and the pulse passing through the center of the burning. This is due to the change in real refractive index and absorption coefficient at the site of burning compared to the healthy tissue. Although loss of water can be a reason for such change, it is believed that this cannot be the only reason.

#### 3.2.3.6 Terahertz imaging of the tooth

##### 3.2.3.6.1 Detecting different layers of the tooth [31]

A Ti:Sapphire laser with 800mW average power, 82 MHz pulse repetition rate and 100fs duration pulses has been used in a pulse Terahertz imaging system to image the dentine, enamel and pulp regions in a premolar sample. This sample was cut into half and dehydrated in order to increase the amount of transmitted power through it. The sample was placed at the back of a ZnTe emitter in a quasi-near field configuration. The sample was moved with a translation stage and at each point of the sample, data was captured by moving the delay line. The beam waist and the SNR right after the source were 200μm and 1000:1 respectively.

The premolar sample was imaged from the surface through the enamel layer. A sample pulse passing through the enamel has been shown in figure 3.17(a) and comparing this pulse to a reference pulse, the displacement of the pulse due to change in refractive index is obvious. The third image of figure 3.17(a) is a sample pulse passing through a section consisted of both dentine and enamel. Here, the pulse has been displaced less than the second figure, which proves that the Terahertz beam has passed through a region with a refractive index less than that of the enamel. The measurements agree with this statement since the refractive index of the enamel and dentine has been reported to be 3.2 and 2.6 respectively. Due to a very small change in the thickness of the tooth, the pulse displacement is believed to be mostly affected by the change in the refractive index.

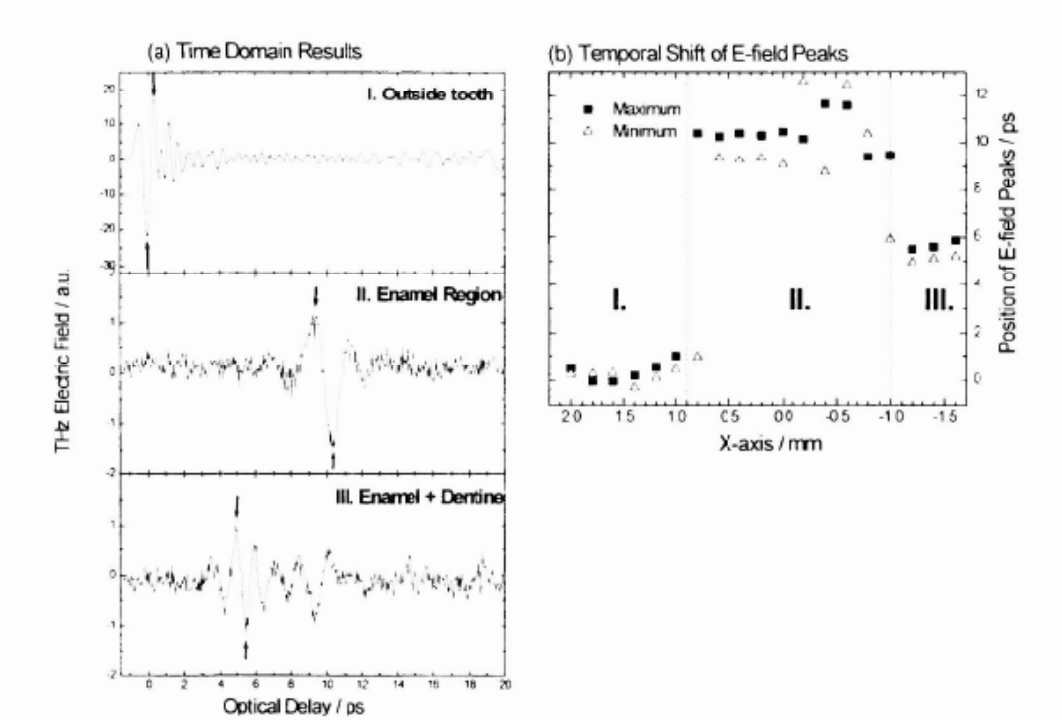


Fig 3. 17 The displacement of Terahertz pulse after passing through different layers of tooth. In figure (a) we can see the larger displacement of the Terahertz pulse when it passes through the enamel region than when it passes through the enamel and dentin region with the same thickness. [31]

Another experiment that was done by the same imaging system was to image the pulp chamber of the tooth [28]. For an extracted tooth, the pulp chamber is empty and thus shows less absorption than a real tooth. This can help us in revealing the state of the pulp chamber.

Moreover, another research team has done the same measurements on a tooth sample with a crack. The result of their measurement is shown in figure 3.18.


Fig 3. 18 A Terahertz image of different layers of the tooth. Enamel, dentine and pulp regions are shown with E, D and P respectively. [28]

3.2.3.6.2 Detection of early caries of the tooth [31]

A Ti:Sapphire laser with 750mW average power, 250 KHz pulse repetition rate and 250fs duration pulses has been used in a pulse Terahertz imaging system to image the early caries in the enamel and distinguish them from Hypomineralisation. The three samples used in this measurement were 200µm-thick sections of tooth. They were stored in physiological saline solution to keep the hydration level equal to that inside the mouth. During the measurements, they were kept in sealed plastic box as close to the back of the emitter as possible (Quasi-near field) to obtain high resolution. One of the three samples has two caries on it; the other one has one caries and the third one has a region of Hypomineralisation. The caries on the first two samples are at early stage, which means they are present in the enamel layer and have extended through the dentine-enamel layer but the outer surface of the enamel isn't still infected by them and thus they are not visible. The visible image, TPI absorption image and TPI Time-of-flight image of these samples are shown in figure 3.19.

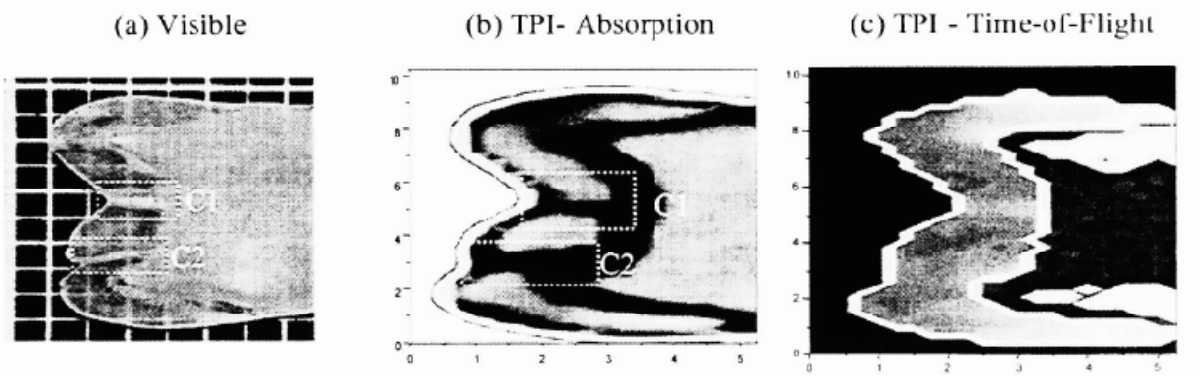


Fig 3. 19 A 200µm thick section of human tooth containing two early caries. [31]

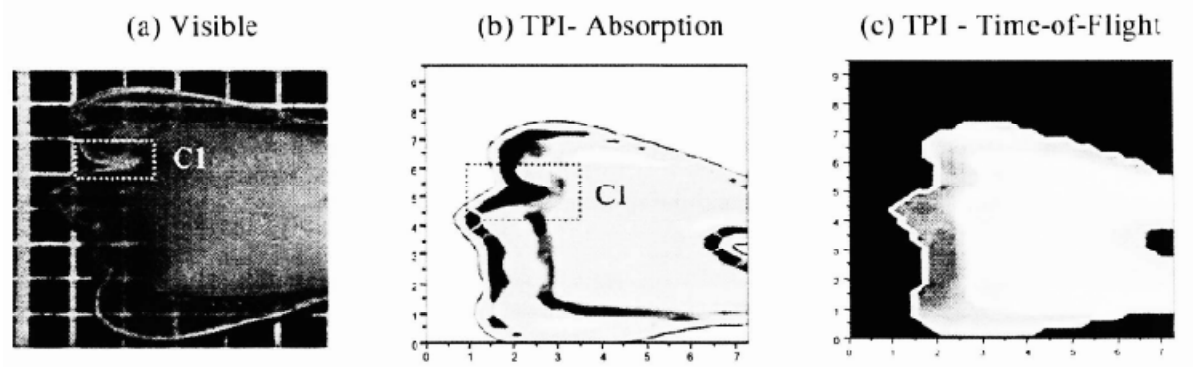


Fig 3. 20 A 200µm thick section of human tooth containing one early caries. [31]

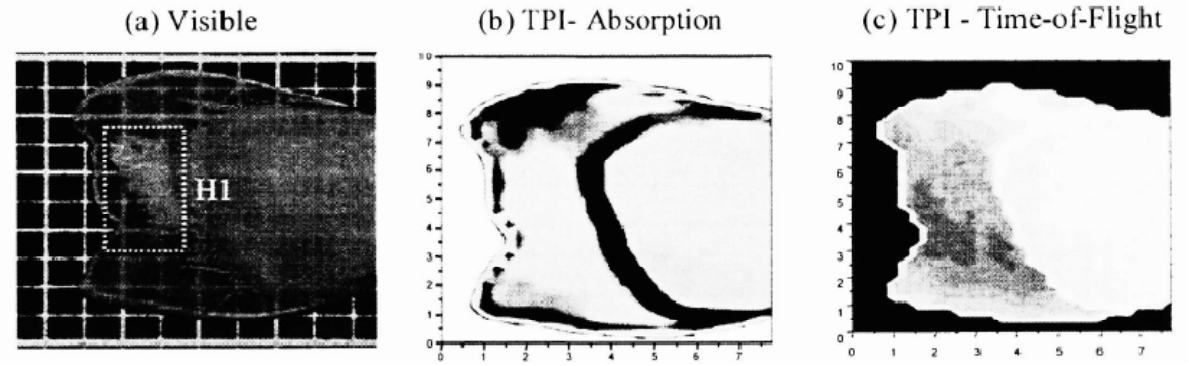


Fig 3. 21 A 210μm thick section of human tooth with Hypomineralisation. [31]

In figures 3.19 (b) and 3.20 (b), the caries can be easily distinguished in the absorption image; while in figure 3.21(b) the region of Hypomineralisation is not distinguishable through the absorption image, which proves the ability of Terahertz in precise detection of early caries and not mistaking it for Hypomineralisation. In all TPI time-of-flight images, different layers of the tooth have been detected. For samples with regions of caries, this image together with the absorption image can give us an idea of whether certain features in the image represent caries or they only represent an interface of two different layers of the tooth.

### 3.2.3.7 Breast cancer detection [28]

In this research, a Terahertz pulse imaging system was used to image an excised human breast tissue. The image of various time-related parameters of this sample was taken to form a meaningful Terahertz image. Figure 3.22 shows the visible and Terahertz image of this sample.

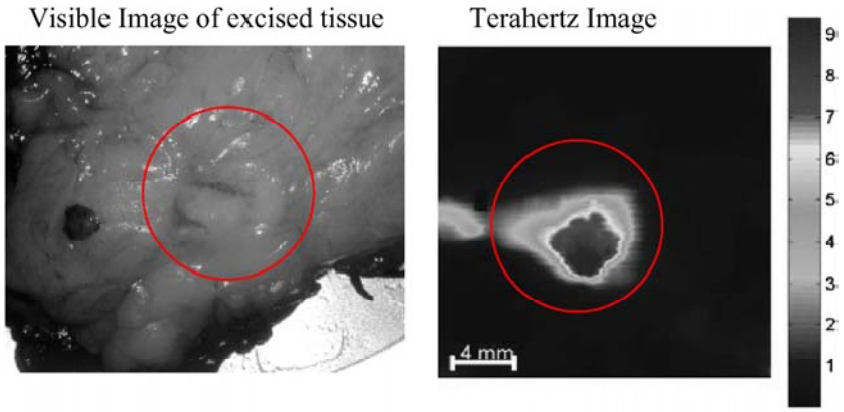


Fig 3. 22 Image of an excised human breast tissue with invasive lobular carcinoma [28]

Moreover, with the same system, a measurement of absorption coefficient and refractive index of normal skin, BCC, normal breast and breast carcinoma has been performed which is summarized in the table 3.1.

| | $\alpha$ (mm$^{-1}$) | $\alpha$ (mm$^{-1}$) | $n$ | $n$ |
|---|---|---|---|---|
| | 0.5 THz | 1 THz | 0.5 THz | 1 THz |
| Normal skin | 11.0 | 16.8 | 2.20 | 2.06 |
| BCC | 13.1 | 19.3 | 2.26 | 2.09 |
| Normal breast | 10.5 | 16.4 | 2.01 | 1.90 |
| Breast carcinoma | 12.5 | 18.6 | 2.23 | 2.08 |
| Breast adipose | 1.3 | 2.2 | 1.56 | 1.54 |
| Water | 16.3 | 23.0 | 2.28 | 2.09 |

Table 3.1 absorption and refractive index of normal and cancerous skin and breast tissue. [28]

## 3.3 Summary

In this chapter, major characteristics of Terahertz waves were remarked. It was shown that many materials (such as some biological tissues) have a “fingerprint” in this range of frequency. All of these led us to the conclusion that Terahertz radiation has the potential to be used in medical spectroscopic and imaging applications. Also, some points regarding the safety issues of exposure to THz radiation was stated. Moreover, the focus put on the medical imaging application of THz radiation and a definition of parametric THz imaging was provided as well as instances of research that had been done on THz imaging of different biological tissues. Through all these examples, it was shown that THz proved to be able to distinguish certain features in tissues as well as reveal unique information about them.

# Chapter 4
# The imaging set-ups used for thesis experiments

In this chapter, the imaging set-ups that have been used for my experiments are introduced, the task of different parts of these set-ups is discussed and the imaging methods that have been used are presented. Moreover, it is discussed that in order to obtain better imaging performance, what considerations must be taken into account about the parameters of the set-up elements. Finally, a short description of the samples that were used for imaging is presented.

## 4.1 Terahertz imaging set-ups

In this section, the set-ups that I have used for imaging are introduced. First, the method of Terahertz generation and detection has been described for each of the pulse and CW imaging systems. Then, the optical elements that are used for aligning the Terahertz beam path in these set-ups have been mentioned. Afterwards, the electronic equipment that is used for SNR enhancement, data acquisition or moving parts of the set-up is introduced. Finally, the software aspects of the imaging project are discussed.

### 4.1.1 THz pulse imaging set-up

In our transmission-mode pulse imaging set-up, as shown in figure 4.1 the beam from the IR laser is split before arriving at the emitter. One portion is incident on the emitter and generates Terahertz; while the other portion arrives at the dipole detector after passing through a delay line and being reflected from a number of mirrors, and helps through the procedure of Terahertz detection. The Terahertz beam is generated by a dipole antenna and then, after passing through the silicon lens in front of the dipole, its directivity increases. Afterwards, this diverging beam would be reflected as a collimated beam after hitting the parabolic mirror on the source side. The reflected THz beam is then focused on the object by L2. After passing through the sample, it is again collimated by L1. This collimated beam is reflected as a focused beam on the detector dipole after hitting the parabolic mirror on the detector side. At this stage, after the interactions that are described in section 3.1.1.2 took place, the photocurrent of the detector dipole is detected through a current amplifier and is shown on a lock-in amplifier which is connected to a PC in case of any need for data transfer or data

recording. Note that the data captured in this case is the photocurrent; therefore the power of the Terahertz signal would be proportional to the squared valued of this data.

In this set-up the source and detector are at fixed positions but since the Terahertz emitter is a point source and the object must be imaged all over its surface, a motorized stage has been developed in order to raster scan the object. Therefore, the only moving parts of this set-up are the object and the delay-line. A picture of the Terahertz pulse imaging set-up is shown in figure 4.1.

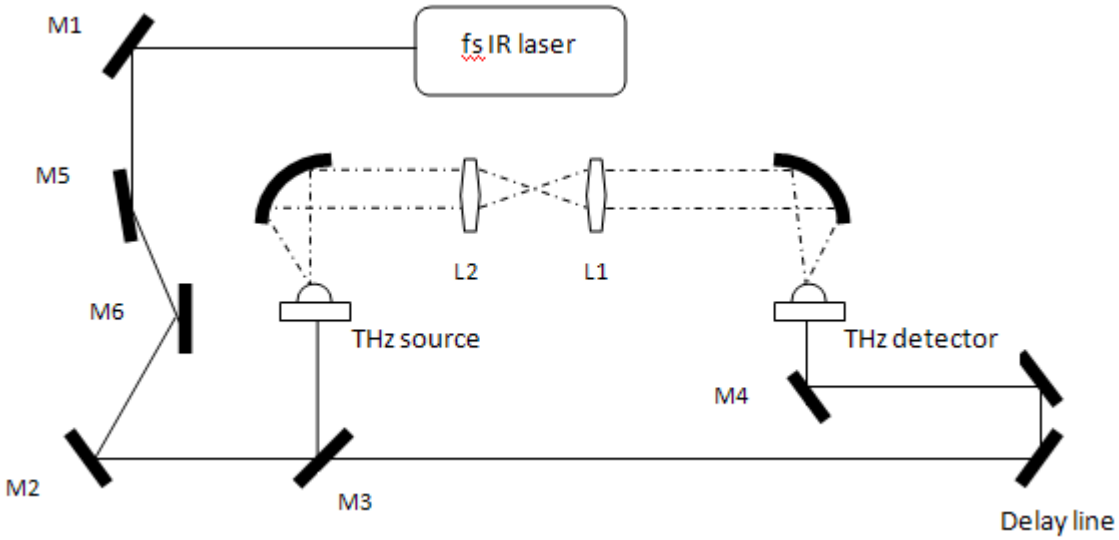


Fig. 4. 1 A schematic of the THz pulse imaging set-up used for the experiments of this thesis

#### 4.1.1.1 Terahertz source

In our THz pulse imaging set-up, a dipole antenna was used as the source of THz radiation. The source of IR radiation was a Ti:Sapphire short pulse laser with pulse duration of 100fs and repetition rate of 80MHz which lased at 780nm. The average power of the laser was 100mW at 780 nm [35].

A dipole antenna is a dipole with a gap much shorter than the wavelength. In order to bias this dipole, a DC voltage is connected to it. When the laser beam is incident on the gap between the two arms of the dipole, because of the presence of a bias voltage, it generates a photocurrent in the dipole which

causes a radiation around the Terahertz frequencies. The equation of the electric field of a dipole of length $\Delta z$ at far-field is shown below [4]:

$$E_\theta = \frac{j\omega.\mu.I.\Delta z.sin\theta}{4\pi r} e^{-jkr} \quad (4.1)$$

The dipole antenna that was used for part of my measurements was a photoconductive dipole antenna on a low-temperature-grown GaAs (LTG-GaAs) with 80μm arm length and 6μm gap between the arms. A 10 Vpp bias was applied to this dipole. The power of the IR beam incident on the dipole was 14mW.

#### 4.1.1.1 Terahertz detector

In our Terahertz pulse imaging set-up, a photoconductive dipole antenna made on LTG-GaAs with 80μm arm length and 6μm gap between the arms was used as the detector.

As mentioned earlier, the IR beam from the laser is split between the emitter and the detector. This IR probe beam gates the dipole and generates carriers at the detector. When the generated Terahertz beam is incident on this detector dipole, it serves as the bias for the dipole which causes the generated carriers to produce photocurrent at the detector. This photocurrent is the parameter that is measured by the lock-in amplifier through a current amplifier.

#### 4.1.1.2 Optical elements, electronic devices and motorized stages

The optical elements that have been used in the set-up were beam-splitters, parabolic mirrors which operated in the Terahertz range of the spectrum and attenuators. Attenuators were used to reduce the power transmitted from the femto-second laser to either the emitter or the detector. Moreover, a number of flat mirrors were used in order to align the beam emitted by the IR laser.

Additionally, a number of electronic devices were used in the set-up such as current amplifier, which amplifies the photocurrent generated by the photoconductive detector before it enters lock-in amplifier and the lock-in amplifier which increased the SNR and displayed the detected signal.

Moreover, motorized stages were used, one for moving the delay line and two for moving the object in two perpendicular directions. The details about controlling the motion of these motorized stages are mentioned in 4.2.1.

#### 4.1.1.3 Software interface

There were a number of tasks which required software programming of some kind. For instance, the motion of the motorized stages which moved the object needed to be programmed so that it was synchronized with the data acquisition system (lock-in amplifier), in order to take the sample of the object at certain times. Moreover, the data recorded by the lock-in amplifier had to be read by the PC and be stored for further processing and image formation.

Therefore, with the help of LABVIEW and MATLAB, a program was written in order to control the motors' motion, control the data acquisition system (GPIB in our case) and synchronize motor motion with the data acquisition system.

### 4.1.2 Continuous-wave imaging set-up

The CW Terahertz imaging set-up consists of a backward-wave oscillator (BWO) as the main source. A series of ×2 and ×3 frequency multipliers are designed to be attached to the output of the BWO in order to generate narrowband signal of frequencies between 85.4 GHz and 1.59 THz. The diverging output beam of the BWO then enters a collimating lens and is chopped with a mechanical chopper. The collimated Terahertz beam is focused on the object by a lens and collimated by another lens after passing through the object. Before being detected, the beam has to be attenuated in order not to damage the detector, therefore, a series of attenuators are placed on the path of the beam. Afterwards, a lens focuses the beam on the detector. In order to detect Terahertz signal at lower frequencies, which normally have higher power, a Pyro-electric is used while for signals at higher frequencies with lower power, a Golay-cell is preferable [35].

In the quasi-optical CW set-up, similar to the pulse imaging set-up, the source and detector are fixed and the object is moved with a pair of perpendicular motorized stages. In this set-up, unlike the pulse imaging set-up, the output of the detector is the power value, therefore, it is connected to the lock-in amplifier directly without the need for a current amplifier.

The software programs that are required for motor motion and for data acquisition are same as those written in LabVIEW and MATLAB for the pulse imaging set-up.

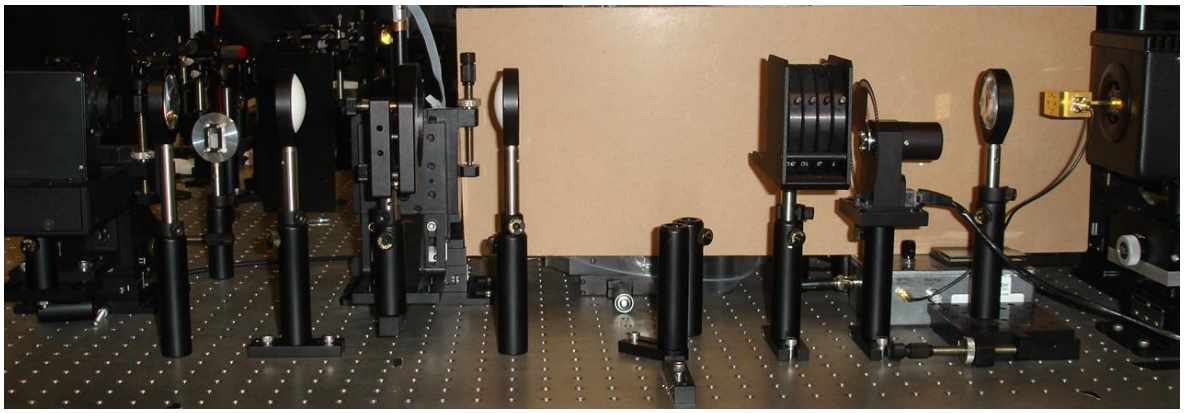

(a)

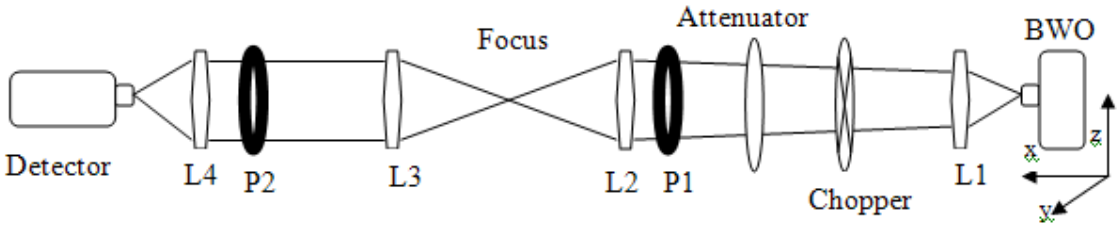


(b)

Fig. 4. 2 (a) A picture of our THz CW imaging set-up with a backward wave oscillator as the source, (b) The schematic of the CW imaging set-up

## 4.2 Imaging methods

Depending on the type of object, I have used two types of imaging in my experiments: either imaging in two dimensions all over the surface of the sample perpendicular to the beam direction, or time-of-flight measurements in addition to a two dimensional imaging, which can be regarded as a three dimensional imaging. The former method can be used in both the THz pulse and THz CW set-ups; while the latter can only be used in the THz pulse imaging set-up because the signal in this set-up is a narrow pulse in time domain and its time delay would change with any change in the medium through which it is passing.

### 4.2.1 Imaging in two dimensions

I used the first method in order to image samples with significant features on their surface and no information along their depth; such as the T-shaped phantom object. To find the beam profile and characteristics of the imaging set-ups, I also used a two dimensional imaging.

In this method, the object is placed on a pair of motorized stages which move in perpendicular directions to one another and also to the direction of the Terahertz beam, in order to raster-scan all over the object's surface with the Terahertz beam. One motor moves the object horizontally and the other moves it vertically. In order to control the motor movement and to control the data acquisition system, LabVIEW was used. The sequence of motor motion and data acquisition is that when the horizontal motorized stage moves the object along a horizontal line, the lock-in has been set to collect data with a certain sampling frequency with a certain time-constant. When the movement along a horizontal line is finished, the vertical motor has been programmed to move vertically for a distance equal to one step-size (pixel size). The value of the step-size (pixel size) is determined by the sampling frequency of the lock-in amplifier and the velocity of the motorized stage along the horizontal direction. While the vertical motor is moving, the lock-in has been paused in order not to collect any data. After the vertical motor finishes its motion, it means that the system is ready for scanning the next horizontal line; therefore, the horizontal motor begins to move and the lock-in amplifier is reset by the LabVIEW program to collect data of the new line.

### 4.2.2 Spatio-temporal imaging

In two dimensional imaging, the image of just one point of the Terahertz pulse is taken at all of the points on the object's surface. In spatio-temporal imaging, however, the image of the whole Terahertz pulse is taken at every point of the object's surface. This method is used, when some information is hidden in the depth of the sample and is needed to be extracted.

The horizontal and vertical motorized stages function as in the previous method: They are moved so that a point on the sample's surface would be in the path of the Terahertz beam. Then, while these two motors have stopped at that point, the motor that moves the delay line begins its motion. As this motor moves, the lock-in takes samples with a constant rate. These samples display different points of the Terahertz pulse which have arrived at the detector with different delays. Therefore by monitoring them on the lock-in, we can see the pulse shape.

The main advantage of this method is that the location of the pulse's peak and the bandwidth of the pulse would change if the beam passes through different materials with different thicknesses and different refractive indices. Thus, this is a powerful method for inspecting the thickness of various layers in a structure, the change in the refractive index of a structure, verifying the presence of an abnormality in a structure and any feature which is present in the depth of an object. In my experiments, I used this method in order to take time-of-flight images of a tooth crown sample.

### 4.2.3 A discussion about the imaging parameters of our set-ups

There are a number of parameters related to motor motion and the data acquisition of lock-in that must be chosen or calculated properly before imaging. This must be done either due to limitations of the equipment or in order to enhance the quality of imaging and reduce unwanted effects such as noise or blurring. These parameters are listed below:

Maximum velocity of the motorized stages: The velocity limit for the motorized stages is 0.5 mm/s.

Time duration between spatial samples in two dimensions: Ideally, we want to spend the least possible time on scanning the object. That's why the time between spatial samples should be minimized. From the other side, this time duration is limited by the time constant of the lock-in amplifier; because the time interval between samplings must be at least 4 to 5 times the time constant of the lock-in amplifier in order to provide the lock-in with enough averaging time before recording each sample. The time constant of the lock-in amplifier determines the bandwidth of the measurements of the lock-in. Generally, it is preferable to have larger bandwidth and smaller time constants; this would, however, increase the noise of the system. Therefore, there is an optimal value of time constant for each measurement. Due to these considerations, I chose 100ms time constant for my measurements. Therefore, I needed the time duration between spatial samples to be at least 500ms. Note that the inverse of this value is set as the "sampling frequency" on the lock-in amplifier.

The spatial step-size or the pixel size: This parameter is calculated by plugging the two previously mentioned parameters in equation $\Delta x = V_{motor} . \Delta t$. It is important to choose the pixel size so that it would be less than half of the smallest feature in the object, according to the Nyquist criteria. At the same time, we must take into account that as long as this value is more than the beam waist of the Terahertz Gaussian beam, reducing pixel size would result in a better resolution while after passing this limit, reducing the pixel size does not necessarily improve the resolution but it increases the total scanning time as in such case, more data should be collected for the same object. Therefore, it must be considered if the small improvement in resolution is worthy of the increase in the number of stored data. Therefore, in the above equation, each pair of these three parameters should be chosen in order to optimize the characteristics of the imaging system [26].

Total number of sampled data in two dimensions: This number is limited by the lock-in amplifier because for a lock-in amplifier, the total scanning time multiplied by the sampling frequency is a constant number. Moreover, although higher resolution images demand for more data, collecting more data would increase the total scanning time. In my experiments, as the objects weren't large and I was sure that the number of data would be less than the lock-in's limit, I first calculated the

appropriate pixel size from the above equation and then calculated the number of required data points by dividing the object dimensions by the pixel dimensions.

Time duration between spatial samples in the third dimension: This parameter must only be considered in spatio-temporal imaging. Due to Nyquist criteria, the time duration between spatial samples must satisfy equation $\delta t \leq \frac{1}{2 f_{\max}}$ where $f_{\max}$ is the bandwidth of the Terahertz pulse. Again, the time duration can't be chosen very small due to the increase in total number of data and hence the total scanning time.

## 4.3 Imaging samples

In this section, the aperture and the samples that have been used in the experiments are demonstrated.

### 4.3.1 T-shaped sample

This sample is a "T" shape made of copper tape adhered to a polyethylene disk with the thickness of 5.5 mm and the radius of 14 mm. This was the first sample we used in order to see if the imaging set-ups can differentiate between the absorbing and transparent media. It was also used as a phantom in later imaging experiments since its shape was known and the taken images could be compared to it in order to figure out the aberrations of the imaging system [35].

A photo and a schematic of this sample with its dimensions are shown in figure 4.4.

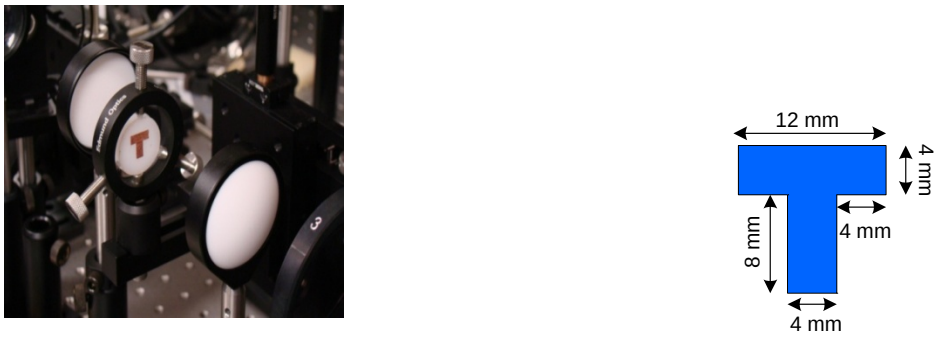


(a) (b)

Fig. 4. 3 (a) Picture of the T-shaped sample mounted on the motorized stages. (b) Schematic of the T-shaped sample with dimensions

### 4.3.2 Aperture

The pinhole that is used to find the beam profile of the imaging set-ups is a circular aperture of 2.2cm diameter and with a variable pinhole whose diameter can be changed between 1.2cm and 0.8mm. This aperture is made of a material which blocks Terahertz radiation.

Fig. 4. 4 The pinhole used for finding the beam profile of the Gaussian beam

### 4.3.3 Tooth crown sample

Our tooth crown sample was a crown produced by Procera® for posterior teeth. This sample is a shell which looks like a tooth from outside but is empty inside and it has a two-layered wall: The inner wall is made of zirconia with refractive index equal to 2.15 [48] and the outer wall is made of porcelain with refractive index equal to 1.5 (The frequency at which these values of refractive were measured weren't specified in the literature; therefore, these values are used as approximations in the calculations that are shown in the next chapter) [47]. A picture of the sample and a schematic of its dimensions and the thickness of each of its layers are shown in figure 4.6.

(a)

(b)

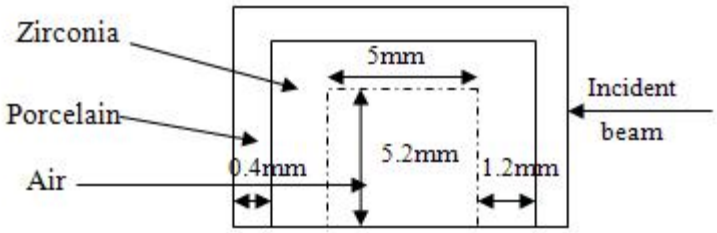


(c)

Fig. 4. 5 (a) Tooth crown sample (from top), (b) Tooth crown sample (empty inside), (c) Schematic of the thickness and material of different layers of the sample

## 4.4 Summary

In this section, the two imaging set-ups that were used for the experiments of this thesis were introduced together with the source, detector and other elements that were used in them. Moreover, the two-dimensional and spatio-temporal methods of imaging, which were used in the thesis experiments, were reviewed. Finally, the different samples that were used for measuring different parameters of the two set-ups were shown.

# Chapter 5
# Methods and results

This chapter includes the experiments, theoretical relations and simulations which were designed for finding the imaging parameters of both of our imaging set-ups as well as taking the image of certain samples. The result of these experiments, simulations and theoretical calculations are demonstrated, afterwards. Analysis of the derived results together with a comparison between the results calculated from different methods has also been presented.

## 5.1 Experiments and methods used

After an introduction into the imaging set-ups and samples that were used in the previous section, in this section, the experiments that were done are discussed. Firstly, the methods used for imaging the T-shaped sample and also certain parameters of the images taken of this sample are mentioned. Afterwards, the experiments and methods that are done to find the characteristic parameters of our imaging set-ups are discussed. In order to make our methods more clear, the general definition of the parameters that are used to characterize the imaging set-ups, together with their mathematical equation is presented. Then, these definitions are used to derive certain methods that I used to do the measurements. As the last experiment, the imaging method that is used for imaging a tooth crown sample is discussed.

### 5.1.1 Imaging of the T-shaped sample

This sample was made by adhering a copper tape as a shape of "T" on a polyethylene disk. The shape and dimensions of this sample are shown in figure 4.4. It was the first sample we designed for imaging. The structure is relatively simple: The polyethylene region is transparent to Terahertz radiation while the copper region is highly absorbent. The main objective for the design of such structure was to verify the possibility of taking an image of it by the pulse and continuous-wave set-ups.

In both set-ups, the sample was fixed on a two dimensional translation stage and was raster scanned by the stage so that the incident beam scanned it and the image was detected point by point at the detector. Note that in both set-ups the sample must have been placed at the focus of the beam between two object lenses. In the pulse set-up, however, the delay-line had to be changed as well so that we have the peak of the THz pulse at the surface of the sample, because when we put the sample on the

beam's path, the position of the THz peak changes due to the change in the refractive index of the path its passing through. At this point, the thickness of the sample was assumed to be homogeneous, so the position of the delay-line didn't need to be changed while scanning.

This experiment was repeated with the pulse imaging set-up for different sampling rates, which was analogous to pixel size of the image, in order to see if the resolution of the images changes by changing the pixel size. Generally, when the speed of the translation stage is constant, higher sampling frequency results in a noisier image because the averaging time over each pixel decreases. Moreover, higher sampling frequencies mean storing and processing higher number of data points which would be time-consuming. Therefore, it is desirable to have low sampling frequencies as long as the resolution is not diminished. Therefore, the objective of these series of experiments was to conclude how far the change in sampling frequency affects the resolution in order to find out an appropriate value for sampling frequency and the speed of the stage or the pixel size ( $\frac{\text{speed of the stage}}{\text{sampling frequency}} = pixelsize$ ) for our next experiments.

The same experiment was also repeated with the CW imaging set-up at different frequencies in order to investigate if the resolution of the images in this set-up changes noticeably with the change in frequency of the incident wave.

In addition to achieving the two objectives mentioned above, these series of measurement also provided a brief comparison of the images taken with the pulse and CW imaging set-ups. However, this comparison has been made more precisely in the experiments that are going to be discussed in 5.1.3.

### 5.1.2 Finding the beam profile

The objective of this experiment was to find out the beam profile for the pulse set-up and at different frequencies for the CW set-up in order to see how symmetrical and how close they were to the profiles predicted from the theory. Measuring parameters such as the beam waist was also helpful in obtaining some idea about the resolution of the pulse set-up or at different frequencies of the CW set-up.

In order to find the beam profile, a pinhole with a hole of radius equal to 0.4mm was placed at the focal point of the two object lenses. The surface of the pinhole around the hole was made of a material which absorbed the incident beam completely and the pinhole was fixed on a translation stage. The stage and the pinhole were moved in the horizontal direction so that the pinhole scanned the incident beam in the horizontal direction. The transmitted signal through the hole which was

detected at the detector, revealed the beam profile in the horizontal direction. The same experiment was done in the vertical direction in order to obtain the vertical beam profile.

#### 5.1.2.1 Beam profile in CW imaging set-up

At the output end of the source of our continuous wave imaging set-up, the backward wave oscillator, there is a wave guide whose radiation pattern can be estimated by a Gaussian beam. This estimation provides a less complicated model of this imaging set-up. Moreover, the results of the measurements on finding the beam profile and beam size, confirms that the incident wave in this set-up can be approximated as a Gaussian beam. According to such assumption, in order to discuss the methods that were used to find the size of the beam by the results of measurements and by theory, a brief review of the properties of Gaussian beam is going to be mentioned here.

A Gaussian beam that is traveling along the z-direction is a 2-dimensional Gaussian function with an axis along the z-direction. The complex amplitude of such wave can be shown as [2]:

$$U(r) = A_0 \frac{W_0}{W(z)} \exp\left[-\frac{\rho^2}{W^2(z)}\right] \exp\left[-jkz - jk\frac{\rho^2}{2R(z)} + jtan^{-1}\left(\frac{z}{z_0}\right)\right] \quad (5.1)$$

Where

$$W(z) = W_0\sqrt{1 + \left(\frac{z}{z_0}\right)^2} \quad (5.2)$$

$$R(z) = z\left[1 + \left(\frac{z}{z_0}\right)^2\right] \quad (5.3)$$

$$W_0 = \sqrt{\frac{\lambda z_0}{\pi}} \quad (5.4)$$

Where $W_0$ and $z_0$ are called the waist radius and Rayleigh range respectively. $2W_0$ is the size of the beam at the center of a Gaussian wave where the intensity on the beam axis is maximum and the phase of the beam is constant over a perpendicular surface to the z-axis which makes the Gaussian beam equivalent to a plane wave at this point. $z_0$ is a point on the axis of the Gaussian beam where the intensity on the beam's axis is half its peak value and the phase is retarded by 45 degrees relative to the phase of a plane wave. At this point, the Gaussian beam has its maximum curvature.

The power of a Gaussian beam is concentrated along the z-axis but this concentration reduces as we travel farther from the center of the beam (z=0) in both directions of z axis. Therefore, the intensity distribution of the beam at any plane transverse to z-direction has a two dimensional Gaussian profile where the waist of the Gaussian profile gets larger as the distance from the center of the beam grows. Equation 5.1 can be used in order to write the following intensity equation for a Gaussian wave:

$$I(\rho, z) = I_0[\frac{W_0}{W(z)}]^2 \exp\ [-\frac{2\rho^2}{W^2(z)}] \tag{5.5}$$

Figure5.1 shows the beam width of a Gaussian beam along z-direction:

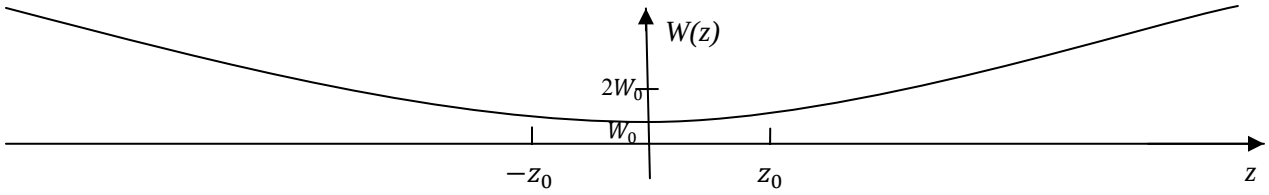


Fig 5. 1 Beam width of a Gaussian beam at different points along its direction of propagation

By looking at equation 5.5 we can see that if we plot the intensity of the Gaussian wave versus its radius at a certain z (say z=0), it would have a Gaussian profile with an intensity equal to $I_0$ at x=0 and $\frac{I_0}{e^2}$ at $\rho = W_0$. This is the property that was used in the experiments I did, in order to find the beam waist. In the experiment, as mentioned earlier, the intensity of the beam transmitted through a pinhole located at the focus of the beam (z=0), was measured and plotted versus the horizontal position of the pinhole. This Gaussian profile was then analyzed in order to find the point along the horizontal axis at which the intensity was $\frac{1}{e^2}$ of its maximum value. The distance from this point to the center point would give us the value for $W_0$ [2].

A theoretical method was also used in order to calculate the beam waist at the focus in this CW set-up. As shown in figure 5.2, by placing the phase center of the BWO's waveguide at the focus of L1, a Gaussian beam with a larger waist would form at the back of L1 which can be regarded as a collimated beam. This beam is focused and transformed to a Gaussian beam with a smaller beam waist when it passes through L2. For such case, where a collimated Gaussian beam is reshaped to a Gaussian beam with a smaller size, the following equation can be used to find the beam waist at the focus of the lens:

$$W_0 = \frac{D}{\sqrt{1 + (\frac{z_0}{f})^2}} \tag{5.6}$$

$$z' = \frac{f}{1 + (\frac{f}{z_0})^2} \tag{5.7}$$

Where $f$ and $D$ are the focal length of the lens and the half beam waist of the incident beam on the lens respectively and $z_0$can be calculated from equation 5.4.

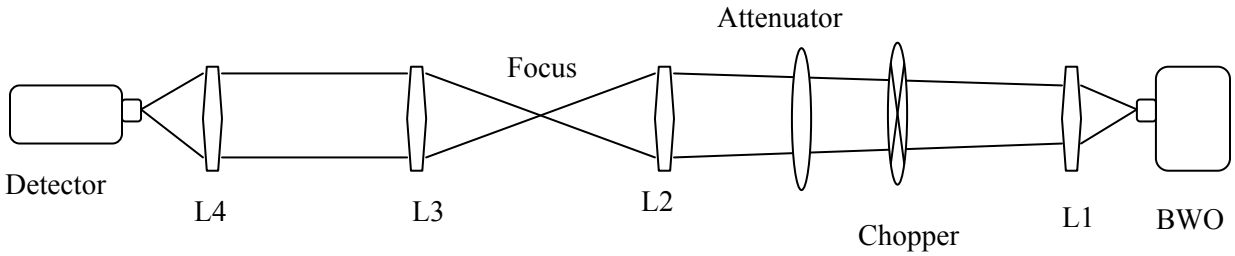


Fig 5. 2 A schematic of the beam propagation in the THz CW imaging set-up

A more detailed description of Gaussian beam reshaping is offered in appendix A.

A comparison between the results of the measurement of the beam waist for different frequencies and that obtained from theory is presented in the results section.

#### 5.1.2.2 Beam profile in pulse imaging set-up

The radiation pattern of the dipole antenna used in our imaging set-up is a spherical wave. The silicon lens in front of it is expected to increase its directivity and also add side lobes to it. This radiation pattern can also be estimated with a Gaussian beam which becomes a collimated Gaussian beam with a larger beam waist after being reflected from the parabolic mirror. Afterwards, this collimated beam is reshaped into a Gaussian beam with a smaller beam waist after passing through L2 (figure 4.1). The location of the beam waist of this beam is the surface of the sample (the focus of L2).

Based on this approximation, we can find the beam waist of this Gaussian beam at the focus of L2 by using the explanations and definitions which were presented in 5.1.2.1 for the Gaussian beam in the CW imaging set-up. The result of calculating the beam waist of the pulse set-up from both theory and measurement is shown in 5.2.2.2.

### 5.1.3 Modulation Transfer Function (MTF)

One of the parameters that is used for description of the performance of an optical imaging system is the OTF. Optical transfer function (OTF) gives us all the required information about the amplitude

and phase of the transfer function of an optical imaging system. In many cases, however, the amplitude of the transfer function which is called the modulation transfer function (MTF) is enough for extracting many properties of the imaging system.

In this thesis, two methods have been used to calculate the MTF of our pulse and CW imaging set-ups in order to show their performance. Before discussing those two methods, two functions must be introduced.

Line spread function (LSF) and edge spread function (ESF) are two more functions that are used to determine the performance of an imaging system. LSF is the image of a narrow slit that is put in front of the imaging source and ESF is the image of the boundary between a highly absorbing and highly transparent medium. For an ideal imaging system, ESF must be a step function, while for real systems this step function smoothens. Therefore, ESF shows how well the system can show the sharpness of an edge. LSF and ESF are related according to the following equation [5, 8]:

$$LSF = \frac{d}{dt} ESF \tag{5.8}$$

Now, we can use LSF in order to define the modulation transfer function. MTF is generally defined as [5, 8]:

$$MTF = \frac{image\ contrast}{object\ contrast} \tag{5.9}$$

And the optical transfer function is defined by using LSF through the following equation [5, 8]:

$$OTF(s) = \mathcal{F}T[LSF(x)] = \int_{-\infty}^{\infty} LSF(x) \exp(-i2\pi xs)\, dx \tag{5.10}$$

Therefore, using the relation between OTF and MTF, we can define MTF as a function of LSF as [5, 8]:

$$MTF(s) = \frac{\left|\int_{-\infty}^{\infty} LSF(x) \exp(-i2\pi xs) dx\right|}{\int_{-\infty}^{\infty} LSF(x) dx} \tag{5.11}$$

This method is used when either LSF or ESF has been calculated.

Another method to calculate MTF is to find the maximum and minimum intensity of the image and of the object in order to calculate the contrast of the image and of the object separately according to the following equation [5, 8]:

$$Contrast = \frac{I_{max} - I_{min}}{I_{max} + I_{min}} \tag{5.12}$$

Then, by dividing the image contrast by the object contrast, the MTF can be calculated.
In order to use the latter method for calculating MTF, usually an object with a sinusoidal pattern is used which includes patterns of different frequencies. It is easier to calculate the maximum and minimum intensity of such an object because of its simple pattern. After taking the image of this object, the contrast and then the MTF for each pattern of a certain spatial frequency can be calculated. By plotting all these MTF values at different spatial frequencies, the MTF graph is plotted.
In this thesis, both methods were used in order to find the MTF. The first method was used to find the MTF from experiments and the second method to calculate the MTF from the results of simulation in HFSS.

#### 5.1.3.1 Finding MTF by using the LSF

In order to apply the first method, the LSF of the imaging set-ups was required and that was calculated by finding the ESF. To capture the image of ESF, a metal, which could absorb the incident beam completely, was placed in front of the beam on a horizontal translation stage. By moving the stage, the metal sheet unblocked the beam gradually until no obstacle was in front of the beam anymore. After finding ESF by this experiment, it was differentiated in MATLAB to obtain the LSF. Then, by taking the amplitude of the fast Fourier transform of LSF in MATLAB and normalizing the resulting function, the MTF was derived. This experiment was done for the THz pulse imaging set-up and at different frequencies for the CW set-up. The results of which are presented in 5.2.3.

#### 5.1.3.2 Finding MTF by finding the contrast

The MTF of the CW set-up was also calculated using HFSS simulation. A cubic structure was designed with metal stripes on top which were located at a distance equal to their width from one another. The distance between each two metal stripes was filled with vacuum which is transparent to signal generated by the BWO. Therefore, these stripes represent a certain spatial frequency at which the contrast is being measured. Then, a Gaussian beam of a certain size was put as a source to this structure and the Poynting vector of the transmitted signal from the structure was measured on a

surface located at a short distance from the back of the structure. In order to find the maximum intensity of the transmitted signal, the integral of the real Poynting vector was calculated on a stripe on the measurement surface right at the back of one of the transparent stripes of the structure. The same parameter was measured on a stripe on the measurement surface right at the back of one of the metal stripes in order to find the minimum intensity. The contrast of the image at that certain spatial frequency was then computed by using the two calculated intensities through equation 5.12. The same simulation was repeated for the same Gaussian waves but for different sizes of striped patterns to find the contrast and so the MTF for different spatial frequencies. By plotting all the acquired MTF values for different spatial frequencies on a single graph, the MTF function of the CW set-up at a certain frequency versus the spatial frequency was obtained. The same MTF graphs were plotted by doing the same procedure for a Gaussian beam of a different spot size, which corresponded to another frequency of the BWO source.

The first method used for calculating MTF was closer to the real MTF of the imaging set-up while the second method was very close to the ideal case. The results of measurement and calculation with both methods are presented in 5.2.3.

### 5.1.4 Tooth crown sample

One of the objectives of our research on THz imaging is to take in vitro images of the tooth using a THz time domain pulse set-up. THz pulse set-up can be used in either transmission or reflection mode in order to take images from a tooth sample. In our set-up, the transmission mode was used. There are some challenges that must be coped with in tooth imaging. Before mentioning these challenges, let's see what happens when a tooth sample is placed in front of a THz beam in a transmission mode imaging set-up.

The incident beam on the sample would be partly transmitted, partly reflected and partly absorbed. The absorbed part cannot be detected. The transmitted part is the portion that is detected in transmission mode set-ups. The reflected portion can be detected only if it is reflected again from one of the interfaces of the different layers of the tooth and is directed to the detector side, otherwise, if it is reflected in the direction of the source, it cannot be detected. The detected pulse is therefore a combination of the transmitted and reflected portions of the THz incident pulse and is different from the pulse that is detected in absence of the sample. The differences can be in displacement of the major peak of the pulse, added reflections to the pulse and also broadening of the major or minor peaks of the pulse. The displacement of the major peak happens because the refractive index along the path that the THz signal was taking changes after putting the sample at focus. Therefore, this

displacement depends on the refractive index of all the layers of the tooth as well as the thickness of each. Added reflections to the pulse shape occur because of the reflection of the incident THz beam from the interface of each two layers of the tooth, which have different refractive indices, and therefore depend on the refractive index and thickness of the layer that it is reflected from. The broadening of the THz pulse can mainly occur because of the dispersion phenomena. Generally, the refractive index of most of the dielectric material, such as the components of the tooth, is dependent on the wavelength of the incident wave. Since the THz pulse is a wideband signal, the refractive index of the layers of the tooth is different for each of the wavelengths of this pulse, which results in a different group velocity for each of them and therefore a pulse broadening effect.

#### 5.1.4.1 Challenges of tooth imaging with the THz pulse set-up and their corresponding solutions

There were some problems associated with tooth imaging in our transmission mode pulse imaging set-up. Firstly, since the transmission mode imaging was being used, it had to be confirmed that the THz source generated a beam strong enough to penetrate the tooth sample and be detected by the detector at the other side of the sample.

Secondly, in tooth imaging, there are different parameters that can affect the detected signal. For example, changes in the refractive index or the thickness of the dentine or enamel are two factors that cause difference between various samples. Since the change of each of these two parameters may lead to a certain defect in the tooth –existence of caries or crack, for instance-, it's important to know what contribution each of these parameters has on the detected signal.

Moreover, as a third challenge, a change in the direction of the incident THz beam can also affect the detected signal. This happens due to change in curvature of the tooth. In this case, the THz beam which was perpendicularly incident on the center of the tooth may hit the corners of the tooth with an angle other than 90 degrees and lead to incorrect results.

The first challenge wasn't an important issue for our case because due to the simulations done with HFSS software, and also due to the transmitter and detector that were used, the amount of the transmitted power was enough to be detected with the detector. As for the second issue, controlled tests were designed in order to show the effects of change in refractive index separately from the effects of the change in thickness on the detected THz signal. In order to figure out the relation between the detected THz beam and a change in the thickness of the tooth, a tooth crown produced by Procera® was chosen as the sample for imaging. Because in this sample, unlike a real tooth, the thickness of each layer was known; therefore, together with knowing the refractive index of each

layer, we could predict how the THz beam would act after passing through the sample. Finally, for the third issue, some simulations were done in HFSS software in order to see if the effects of the change in the angle of the incidence of the THz beam were negligible for this sample or had to be precisely modeled.

Before starting the imaging experiments on real in vitro tooth samples, I performed those experiments on tooth crown samples. The reason was that the tooth crown sample has a simpler structure and its dimensions and thicknesses can be easily measured, unlike a real tooth. This would help us at the beginning, because the results of the experiments could be compared to the measured parameters and could help us through better understanding of the imaging procedure. In the following section, the methods and simulations I used for imaging the tooth crown sample and obtaining a better understanding of its behavior against the THz pulse are presented.

#### 5.1.4.2 The methods used for simulation and measurement

The simulations were done mainly in order to find an answer to the first and third challenges mentioned in 5.1.4.1 and the measurements were done in order to find out about the effect of change in thickness and refractive index on THz pulse characteristics. Giving a definite solution to the second challenge mentioned in 5.1.4.1 requires more time and appropriate measurements.

##### 5.1.4.2.1 Using simulations to find the transmitted power

For the reason that is going to be explained eventually, the problem of power transmission through the tooth crown sample was simplified to the following form: The wall of the sample was assumed as a planar, two layered structure. The incident THz beam on the structure was assumed to be an ideal Gaussian beam -with spot size of 1mm-. This beam is perpendicularly incident from the free space on the structure. First, the Spectral Domain Method was used to find the transmitted electric field through the sample and to calculate the transmitted power at a certain distance from the sample. Afterwards, the same problem was solved with HFSS software. This was done in order to make sure that the results of HFSS software are reliable for such problems.

The total transmitted power calculated with both methods was of the same order of magnitude and the shape of the transmitted electric field was Gaussian in both cases. After this test, the rest of the simulations were done using HFSS.

##### 5.1.4.2.2 Using simulation to find the direction of the transmitted Poynting vector

Due to the limitations of the HFSS software, instead of the exact shape of the tooth crown sample, I modeled it once as a two-layered empty cylinder and once as a two-layered empty box. The Gaussian

beam was shone from different points on a certain surface on both models to see the amount of transmitted power; and more importantly, the direction of Poynting vector after passing through each of the models.

The direction of the transmitted Poynting vector is important in measurements involving tooth sample because as mentioned before, in our method of imaging, the location of the source and detector are fixed and to take an image, the sample is moved, so, in order to detect the transmitted beam as accurately as possible, it would be best if the sample wouldn't refract the incident beam at all. This means that the incident beam takes a straight path from the source to the detector which is equivalent to having the transmitted Poynting vector in the same direction as the incident Poynting vector for every incident beam in HFSS simulations. This is important because as will be discussed in 5.2.4.2.2, the thickness of the tooth was calculated assuming that the beam takes the shortest path through the sample.

#### 5.1.4.3 Measurement method

As shown in figure 5.3, the crown sample was fixed on a Teflon pod on a translation stage between the THz transmitter and detector. The THz beam was focused on the sample with a lens. The method used here was the one explained in section 4.2.2 which reveals information about the position of the THz peak and its reflections. In order to obtain this information, the sample kept fixed while the delay line was continuously moved with a translation stage along a certain range of position. During the movement of the delay line, the detected signal was sampled with a lock-in amplifier. The same procedure was repeated for different points of the sample along a horizontal line which in the end provided a time-of-flight image from which the change in the thickness can be detected by studying the displacement of the THz peak at different horizontal points of the crown sample.

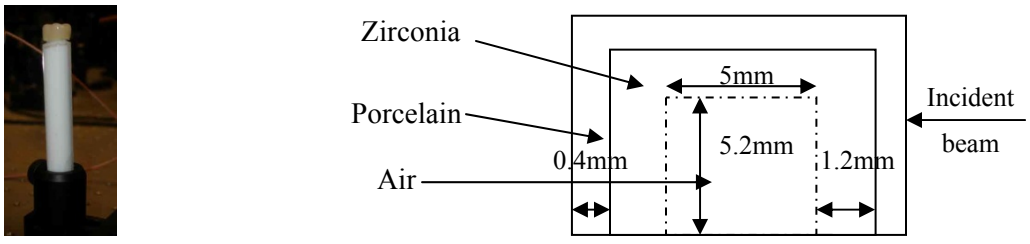


Fig 5. 3 Left: The crown sample on a Teflon pod on the translational stage; Right: Schematic of the thickness and material of different layers of the sample

## 5.2 Results

### 5.2.1 Imaging of the T-shaped sample

#### 5.2.1.1 Results of imaging with the THz Pulse set-up

As mentioned in 5.1, one of the first experiments was to take the image of the T-shaped sample with different sampling rates which led to images with different pixel sizes in order to see if reducing the pixel size would result in a higher resolution or not. Figure 5.4 shows the images of the T-shaped sample taken at three different pixel sizes: 1mm, 500µm and 250µm. It can be recognized from these images that reducing the pixel size up to 250µm resulted in a better resolution, even though; the presence of blurring effect avoided good edge detection.

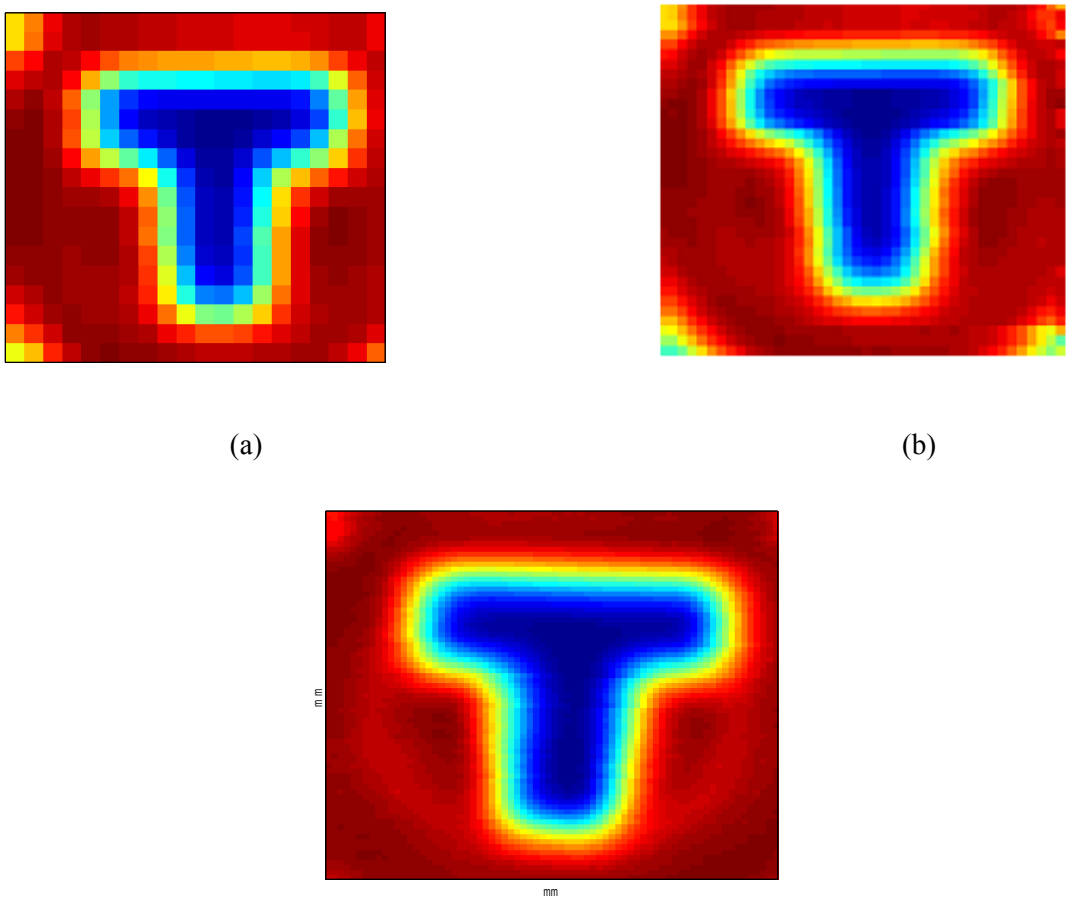


(a) (b)

(c)

Fig 5. 4 Images of the T-shaped sample taken with the pulse imaging set-up with (a) 1mm pixel-size, (b) 500µm pixel size, (c) 250µm pixel size

In order to compare the resolution of the images taken by the THz pulse imaging set-up with different pixel sizes, the MTF of the pulse set-up was also measured using the first technique discussed in 5.1.3.1. Therefore, first, the ESF of the set-up was measured for pixel sizes of 500μm, 250μm and 125μm and then the MTF was calculated. The graph of MTF versus spatial frequency (resolution) is shown in figure 5.5.

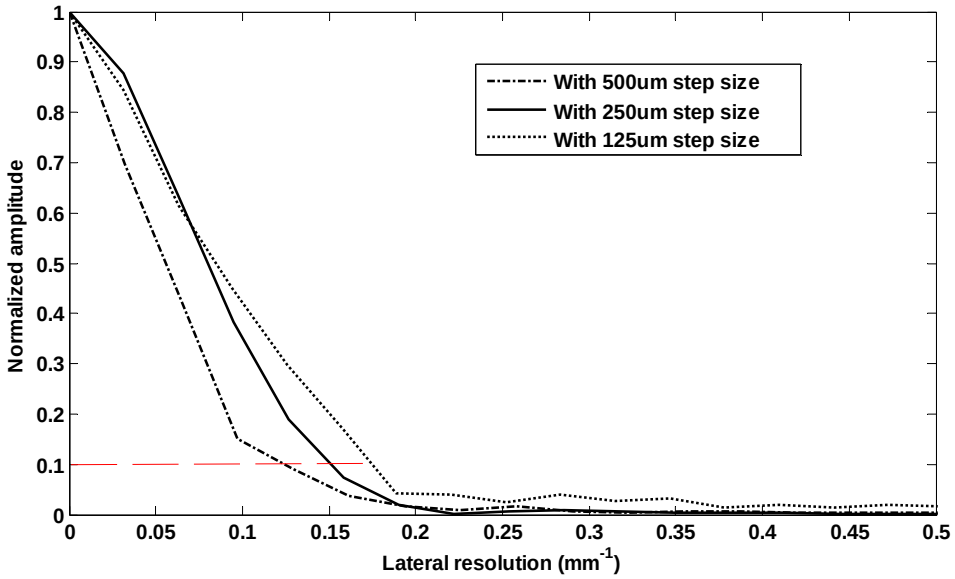


Fig 5. 5 The MTF of the pulse imaging set-up measured for images taken with different pixel sizes

According to this graph, the limiting resolution (the value on the horizontal axis corresponding to MTF=0.1 on the vertical axis) for pixel sizes of 500μm, 250μm and 125μm is 0.13/mm, 0.16/mm and 0.185/mm respectively which shows that the resolution improves by increasing the sampling rate (decreasing the pixel size) at least up to the step size of 125μm. This means that the resolution of this set-up can be improved but at the cost of more time and higher number of data points.

In 3.2.1.1, a short review was presented about the Airy disk and how this diffraction limit limits the resolution of a system which includes an aperture such as a lens. As mentioned there, the resolution of a system is expected to be smaller than one over the radius of the Airy disk. According to the measurements done to find the beam profile of the THz pulse imaging set-up, which is presented in 5.2.2.2, the radius of the Airy disk of the pulse set-up is 3.07mm which results in a resolution of 0.32/mm. A question that may occur at this point is that if the radius of the Airy disk is 3.07mm and we know that the resolution cannot be better than this value, why we do the sampling at such high rates resulting in pixel sizes much less than the resolution. Wouldn't that be a superfluous sampling?

According to the results of measurement, the answer is negative. The results show that sampling at such high rates has improved the resolution. The reason is that because of the large beam size, the intensity of a pixel detected at the detector is a weighted sum of the intensities of the neighbouring pixels. Then, for the next pixel, even though the beam is much greater than the pixel size, the weighting factors have changed slightly which results in a new intensity detected at the detector. However, despite the improvement in the resolution, the blurring effect would be one of the major defects of these images due to the averaging procedure which happens because of the large beam size.

#### 5.2.1.2 Results of imaging with the CW set-up

Images of the T-shaped sample were also taken with the continuous-wave set-up at three different frequencies: 150GHz, 450GHz and 1270GHz. These images are shown in figure 5.6. Note that the pixel size for all three images is 500μm.

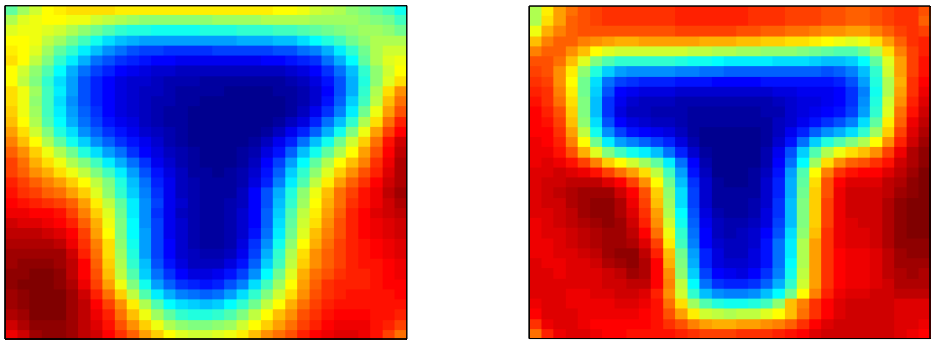

(a) (b)

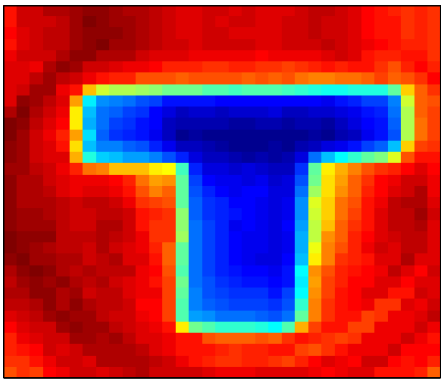

(c)

Fig 5. 6 Images of the T-shaped sample taken with the CW imaging set-up at (a) 150GHz, (b) 450GHz, (c) 1270GHz

In this figure, the improvement of image resolution with increasing the frequency can be easily recognized. Another noticeable feature in these images is that even though the pixel size is the same for all three images, the blurring decreases as the frequency increases resulting in better edge detection. The reason is that with increase in frequency, the beam size decreases as shown in 5.2.2.1. Therefore, as the frequency increases, the intensity detected at the detector for each pixel is less weighted by the neighbouring pixels and is closer to the intensity at that certain pixel, which results in a more precise image. For the beam at 1270GHZ, the beam size is much closer to the pixel size and that is why the image taken at this frequency is almost deprived of blurring, shows sharp edges and even reveals details such as patterns on the polyethylene surface which is not detectable in any other image.

#### 5.2.1.3 Comparison of images taken with pulse and CW set-ups

Comparing the images taken with the two set-ups, we can see that the effect of increasing the frequency of the incident beam in the CW set-up on enhancing the resolution of the image is more than the effect of decreasing the pixel size in the pulse set-up. The reason is that by increasing the imaging frequency, the beam size decreases, which has a greater effect on increasing the resolution than merely increasing the number of imaging samples but use a large beam for imaging.

Now, if we compare the image taken by the pulse set-up with step-size of 500um with the three images taken by the CW set-up with the same step-size, we can see that the closest image taken by the CW to the image taken with the pulse set-up is the one taken at 450GHz (figures 5.4(b) and 5.6(b)) The pulse set-up generates a wideband THz signal which has frequency components from zero to 1THz GHz. Therefore, each image includes all these frequency components to some extent, however, if we look at the profile of the THz signal of the pulse set-up (figure 5.7), we can see that the maximum energy of the signal is concentrated between 300GHz and 390GHz, which is quite close to 450 GHz and that is the reason why the image taken with the pulse set-up resembles that of the CW taken at 450 GHz.

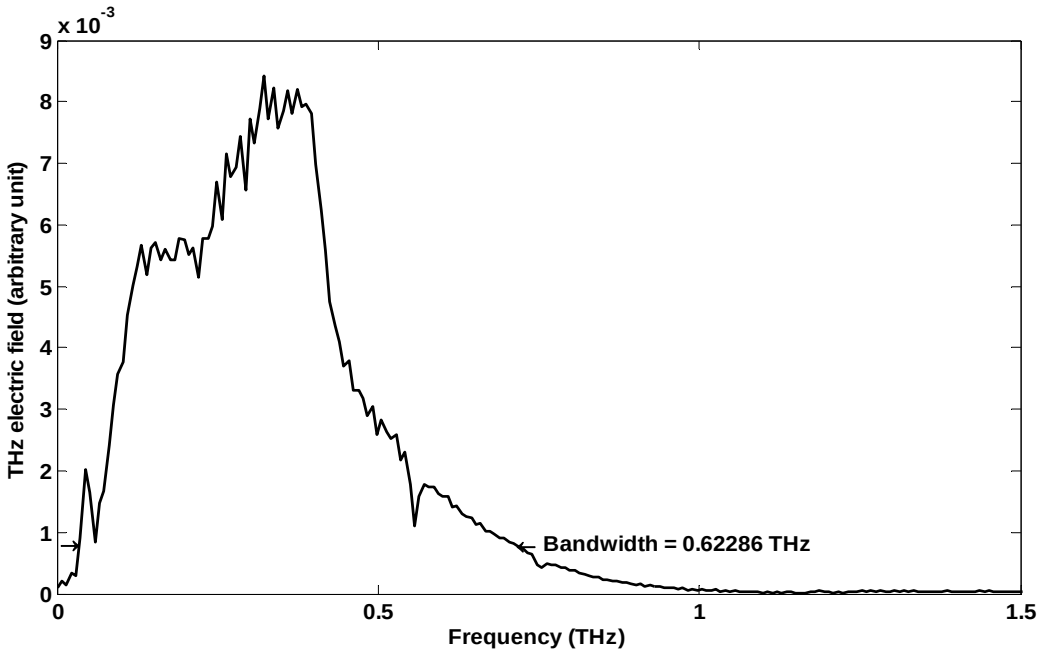


Fig 5. 7 The frequency content of the THz pulse of the pulse imaging set-up

In order to compare the performance of the two set-ups as well as their resolution, the images of the T-shaped sample are not sufficient and we must look at the MTF of these two set-ups. A comparison of the modulation transfer function of these set-ups is presented in 5.2.3.1 which is calculated based on the method introduced in 5.1.3.

### 5.2.2 Results of beam profile measurement

#### 5.2.2.1 Beam profile in the CW set-up

As mentioned in 5.1.2.1, the output beam of the BWO has been considered as a Gaussian beam and its beam waist at the focus of the CW imaging set-up has been found using both measurements and theory. The results are shown in table 5.1. In this table, the second column represents the values of the beam waist calculated from the measurements and the third column represents the values of the beam waist calculated by substituting f=10cm in equation 5.6. In order to find the value of D (the beam radius before entering the lens) to use in that equation, a pinhole was put right before L2 in the CW imaging set-up and by changing the size of its hole, I tried to find the smallest size of the pinhole for which the detected signal would stay equal to its maximum value and wouldn't decrease. This value was approximately equal to 2.5cm for all frequencies except for 150GHz at which point, the radius of

the beam seemed to be bigger than the maximum size of the pinhole; therefore, I took D equal to the diameter of L2 which was 5cm.

| Frequency (GHz) | Measured beam waist (mm) | calculated beam waist (mm) |
|---|---|---|
| 150 | 6.13 | 5 |
| 450 | 3.4 | 3.4 |
| 730 | 2.28 | 2 |
| 840 | 1.77 | 1.82 |
| 950 | 1.74 | 1.6 |
| 1270 | 1.3 | 1.2 |

Table 5.1 Comparison of the measured and calculated beam waist for a number of frequencies

The small difference between the measured values and calculated values in table 5.1 shows that approximating the beam in the CW set-up as a Gaussian beam was a valid assumption.

#### 5.2.2.2 Beam profile in the pulse set-up

The beam profile in this set-up was measured by using the method mentioned in 5.1.2. This profile was assumed to be Gaussian as mentioned in 5.1.2.2. Calculating the beam waist in this case is, however, slightly different from that of the Gaussian beam in the continuous-wave set-up.

As mentioned earlier, the variable that is measured by the detector in pulse set-up is the photocurrent, which is proportional to the electric field of the THz wave and is proportional to the square root of the power. Therefore, in this case, in order to find the point at which the value on the vertical axis has been divided by $e^2$ in the graph of the detected signal, we must look at a point where it has been divided by $e$. Moreover, equation 5.6 cannot be used to find the beam waist in theory because here, the signal is wideband while equation 5.6 is valid for a single frequency. Two solutions were found for this problem.

The first one was to substitute the wavelength in equation 5.6 with the wavelength at which the pulse has its maximum energy, which gave an approximately close result to the measured beam waist. If we substitute f=5cm (the focal length of the lenses used in this set-up) and D=2.5 (the beam size before entering the lens) in equation 5.6, the beam waist would be equal to 2.2mm while from the measurements the beam waist was calculated to be 2.4mm. Note that as the maximum energy of the pulse was concentrated between 300GHz and 390GHz, I used the middle frequency of this range in equation 5.6 for the pulse set-up.

The second solution I came up with was to decompose the beam of the pulse set-up to many single frequency Gaussian beams. Each of these beams was of a frequency equal to one of the frequency components of the pulse and its amplitude was equal to that of the pulse at the same frequency. Then, equation 5.6 and 5.7 were used in order to find the size of the beam waist and its position after passing through the lens for each of those Gaussian beams. By knowing the beam waist and its position for each of the single frequency beams, I found the magnitude of the electric field of each of them at the focus of the lens (equation 5.1). Afterwards, by adding up all these electric fields, I found the total electric field at the focus. This function had a Gaussian shape with a beam waist of 2.24mm. We can see that the size of the beam waist calculated from the two different approaches are very close to each other and close to the beam waist measured through the experiments. Therefore, based on these results, the assumption that a THz pulse can be approximated as a single frequency Gaussian beam with the same frequency as the average frequency at which the pulse's energy is concentrated, is a valid assumption, at least for finding the beam waist of the beam.

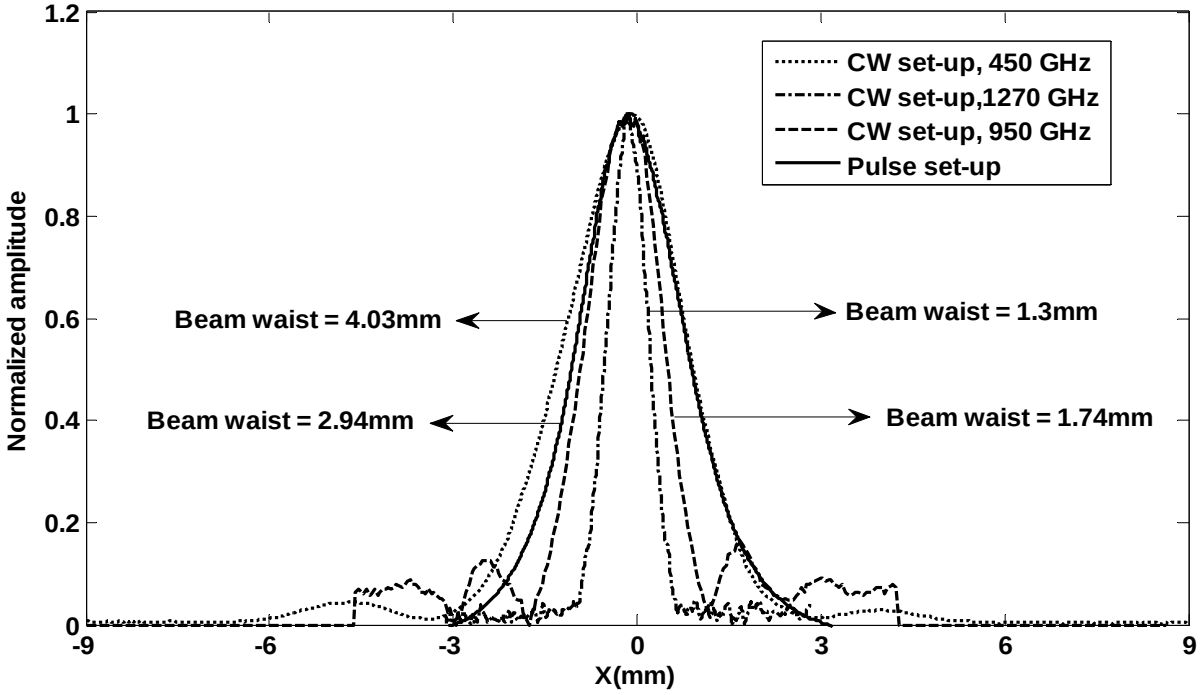


Fig 5. 8 The beam profile and size of the beam waist of the CW set-up at different frequencies and in the pulse set-up

### 5.2.3 MTF calculations

The two methods that were used for finding out the MTF of the imaging set-ups were explained in 5.1.3. The first method was used to find the MTF from the ESF measurements of both set-ups and the second method was used to find the MTF from the simulations in HFSS.

#### 5.2.3.1 Finding MTF from the measurements

Generally, by looking at an MTF graph, two main properties of the imaging system can be extracted: the limiting resolution and the performance of the system along a wide band. The limiting resolution is the resolution at which the amplitude of the modulation transfer function is equal to 0.1 and is regarded as the best resolution the system can offer. Although obtaining high resolution is one of the major goals of any imaging system, having a large limiting resolution doesn't guarantee a good system performance. In order to have an acceptable performance, the imaging set-up must have higher amplitude along the range of resolutions less than the limiting resolution. In other words, for two systems with the same limiting resolution, the performance of the system which has a higher resolution corresponding to MTF=0.5 is better. One of the outcomes of a better performance in an imaging system is showing higher contrasts. By looking at figure 5.9, we can compare the resolution and performance of the pulse and CW imaging set-ups using the definitions provided above.

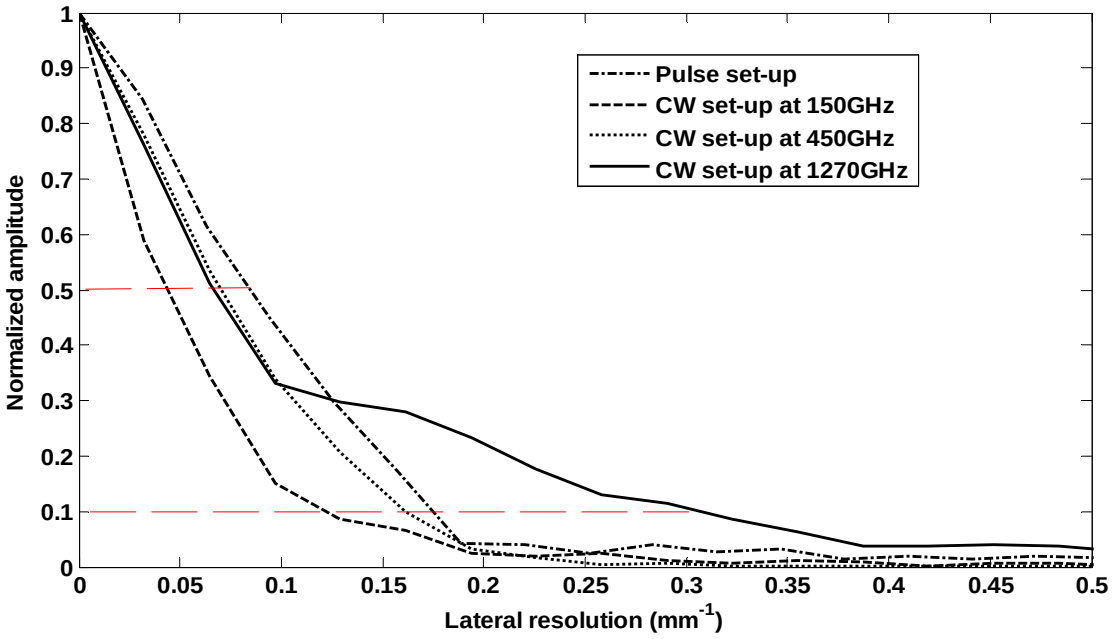


Fig 5. 9 The MTF and limiting resolution of the CW imaging set-up at different frequencies and of the pulse imaging set-up

Comparing the MTF of the CW set-up plotted for incident waves of different frequencies, we can see that the limiting resolution has increased from 0.135/mm at 150GHz to 0.165/mm for 450GHz and 0.32/mm for 1270GHz. This increase in resolution, which was also apparent in the images taken of the T-shaped sample, was expected. However, the values calculated for the limiting frequency of the CW set-up from this MTF graph, show some variation from the values calculated by the formulations of a diffraction-limited system. For a diffraction-limited system, the resolution is expected to be close to the radius of the Airy disk; while in our CW set-up, the resolution seems to be reduced by parameters more dominant than just the diffraction. A more complete discussion of the parameters that limit the resolution in our imaging set-ups is presented in 5.2.3.3.

It can be seen that the performance of the CW set-up has generally improved by increasing its operation frequency especially in the range of MTF=0.1 to 0.3. There's, however, a deviation from this pattern at MTFs around 0.5 for the 1270GHz signal. This statement can also be verified by looking at the images of the T-shaped samples at these three frequencies where the best contrast belongs to the images taken at 1270 GHz.

According to this figure, although the limiting resolution of the pulse set-up is much less than the best resolution of the CW set-up (which occurs at 1270GHz), the performance of this set-up is better than that of the CW set-up at any frequency. This characteristic of the pulse set-up may become useful in imaging cases where contrast and performance is of higher priority than the resolution.

Another point is that the limiting resolution of the pulse set-up is close to that of the CW set-up at 450GHz. This resemblance was also noticeable in the images of T-shaped sample taken with the CW set-up at 450GHz and the pulse set-up and the reason is the concentration of the energy of pulse set-up between 300GHz and 390GHz (figure 5.7) which are relatively close to 450GHz.

#### 5.2.3.2 Finding MTF by using HFSS simulations

As mentioned in 5.1.3.2, HFSS simulation was used in order to calculate the MTF of the CW set-up at three different frequencies using a different method from the one used before. The result of these simulations is shown in figure 5.10.

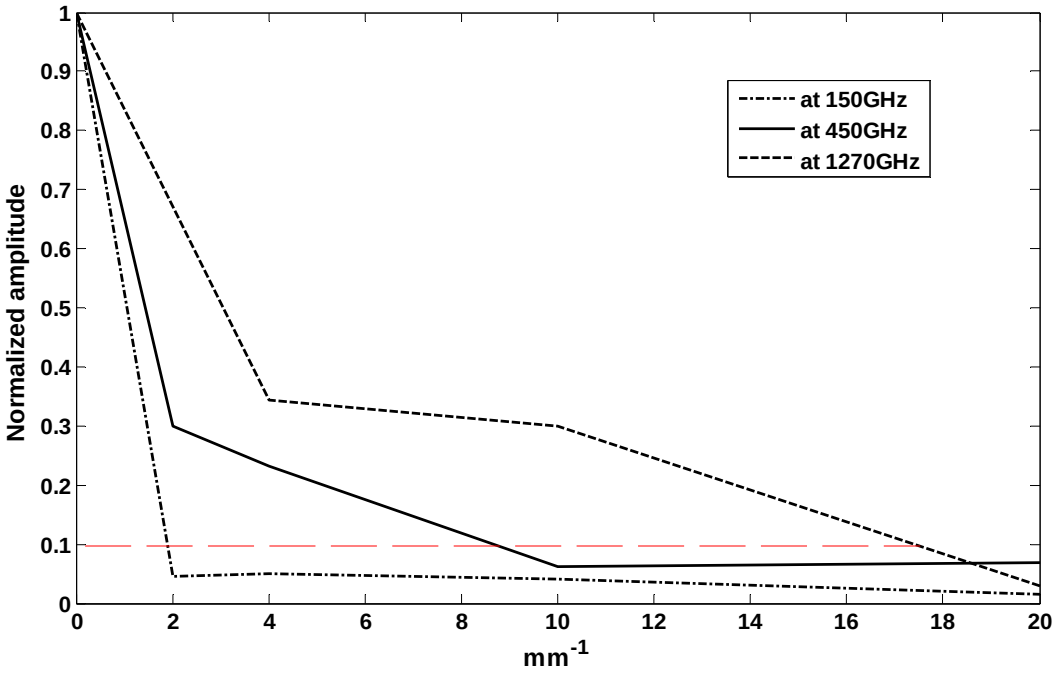


Fig 5. 10 The MTF of the CW imaging set-up for different frequencies calculated from the results of simulation with HFSS

As expected, these results show much better performance and resolution comparing to those obtained from measurements. Doing the simulations for a very simplified model without any lens or optical components and using an ideal Gaussian source are the main reasons for acquiring results close to that expected from theory.

#### 5.2.3.3 A discussion on the resolution limit of the two set-ups

In 3.2.1, a brief introduction into the diffraction-limited imaging systems was presented. We saw that in diffraction-limited imaging systems with a circular aperture, the resolution is limited by the radius of the Airy disk. In order to analyze the performance of our set-ups and verify if they are diffraction-limited or they include aberrations, the width of the main lobe of the beam profile is measured and is compared with the diffraction limit that can be calculated from equation 3.14. These values are shown in the third and forth columns of table 5.2 for the pulse set-up and different frequencies of the CW set-up. Moreover, for a more complete comparison, the limiting resolution calculated from the MTF function is also shown in the fifth column for each case.

As we can see in this table, the measured width of the major lobe of the beam profile is higher than the values calculated for a diffraction-limited system, which proves that both set-ups are not diffraction-limited. According to these results, both our pulse and CW imaging set-ups suffer from aberrations. The reasons may be the presence of THz lenses, properties of some of the optical elements of the set-ups or slight misalignment of the set-ups.

Moreover, the limiting resolution measured from the MTF graph shows even a greater difference with the resolution expected due to the diffraction limit. One reason for obtaining such small resolutions may be because the metal edge that was used for measuring the ESF wasn't sharp enough and resulted in introduction of noise to the measurements. As we know, when noise is present in the system, the measurement must be low-pass filtered to diminish the effects of the noise which would also result in loosing data at high frequencies and thus a reduction of the resolution of the system. Moreover, any source of noise in the set-ups, such as Johnson noise may result in the same problem.

| Set-up | Frequency (GHz) | Diffraction limit, calculated from equation 3.14 (mm) | The radius of the Airy disk from the measurements (mm) | Limiting resolution measured from the MTF function (mm) |
|---|---|---|---|---|
| pulse | wideband | 2.12 | 3.07 | 5.88 |
| CW | 150 | 4.88 | 5.52 | 7.4 |
| CW | 450 | 1.62 | 2.9 | 6.06 |
| CW | 1270 | 0.58 | 1.5 | 3.125 |

Table 5.2 A Comparison between the calculated diffraction limit, the radius of the Airy disk measured from experiment results and the limiting resolution of the set-ups measured from the MTF graph

One way of improving the resolution through image processing techniques is to deconvolve the point spread function of the system from the captured images.

### 5.2.4 Results of simulations and measurements on tooth crown sample

#### 5.2.4.1 Results of simulation

As mentioned in 5.1.4.2.1, simulations have been done in HFSS on a planar model of the tooth crown sample to verify the transmitted power through it. The result was that the transmitted power through such structure was enough for our imaging purpose. Moreover, the value of this power was close to

the results obtained by using the Fourier transform method for the similar structure, confirming that this modeling in HFSS is accurate and can be used for other problems of this nature.

Simulations were also done on the same structure to verify if the angle of the transmitted beam is close to the angle of the incident beam. We can see that in figure 5.11, the output Poynting vector for the left structure is much more directed to the same direction as the incident Poynting vector than the right structure. Moreover, for the left structure, the maximum transmitted power is more concentrated around the same horizontal coordinate as the incident power than for the structure on the right. Therefore, the more the sample is cubic, the more accurate would be the results of our method. As our tooth crown sample was for a rear-tooth and was more cubic shaped than cylindrical, it was more probable that the angle of incidence would remain about 90 degree after passing through our sample.

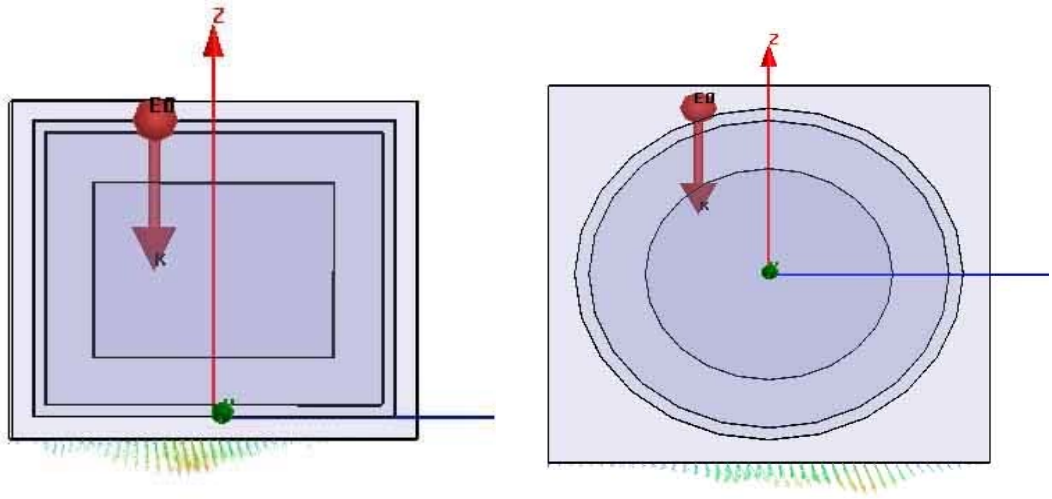


Fig 5. 11 Results of simulation with HFSS for two models suggested for the tooth crown sample: a box (left) and a cylinder (right). The thick red arrow in both figures is the direction of incident Poynting vector and the colored vectors at the bottom surface are the direction output Poynting vector.

### 5.2.4.2 The result of measurements on the tooth crown sample

Displacement of the major peak, extra reflections in the pulse graph and pulse broadening are three parameters that can reveal information about the thickness of the sample. In this section, the result of measurement of these three major parameters and the information provided by these results are discussed.

Generally, for imaging the different layers of a sample structure along its depth, reflection-mode imaging is considered as a better choice than transmission-mode imaging; because the amount of the signal reflected from different layers of the sample and then detected at the source side of the sample is larger than the same reflections detected after transmission through the sample. However, for a simple structure such as the one that has been used in our measurements, the transmitted signal was powerful enough to show the reflected signal from different layers of the structure which were then then transmitted all the way to the detector.

5.2.4.2.1 Displacement of the main peak

Figure 5.12 shows the THz pulse detected at three different points of the tooth crown sample, while the delay line was moved along its full range at each of these points. These points were located 0.5mm from one another. In this figure we can see that the major peak has been displaced from one graph to another. The location of the peak has changed from 13.33ps for the reference pulse to 13.5ps, 13.54ps and 14.92ps at the other three points of the sample. Since the change in refractive index can be assumed equal for all three points on the sample, we can deduce that the displacement is due to the slight change in the thickness of the layers of the sample from one point to another.

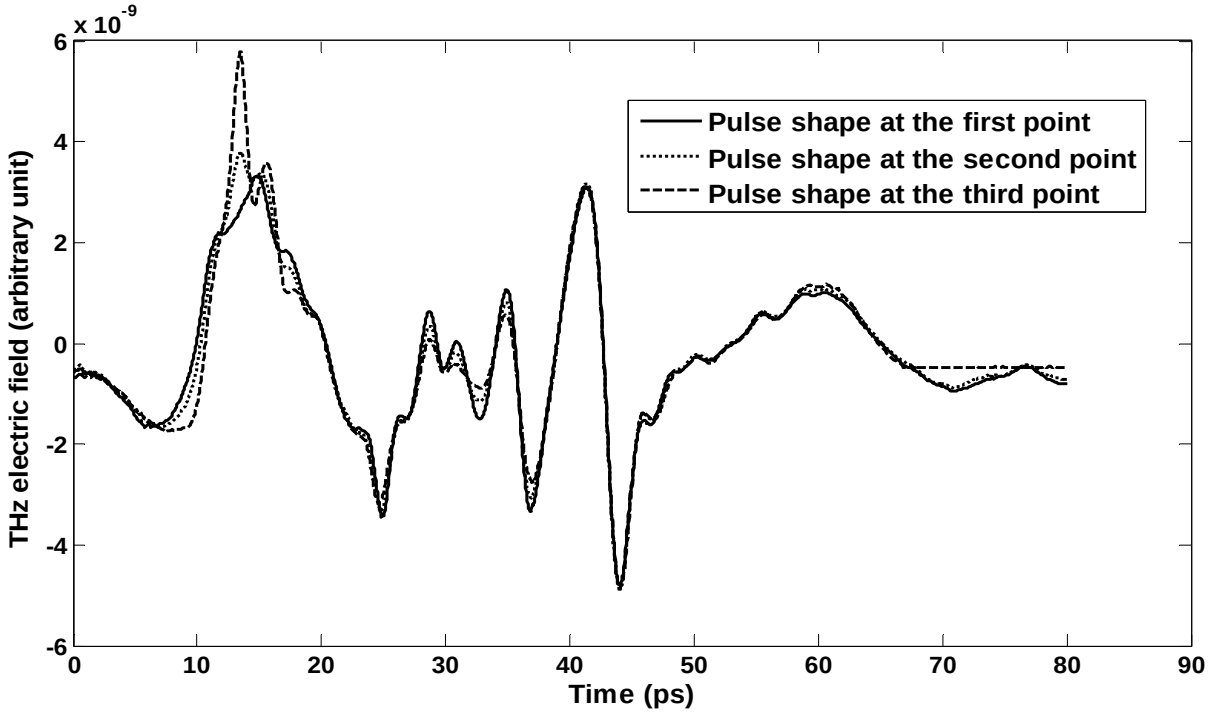


Fig 5. 12 THz pulse scanned at three different points of the tooth crown sample 0.5mm apart from one another

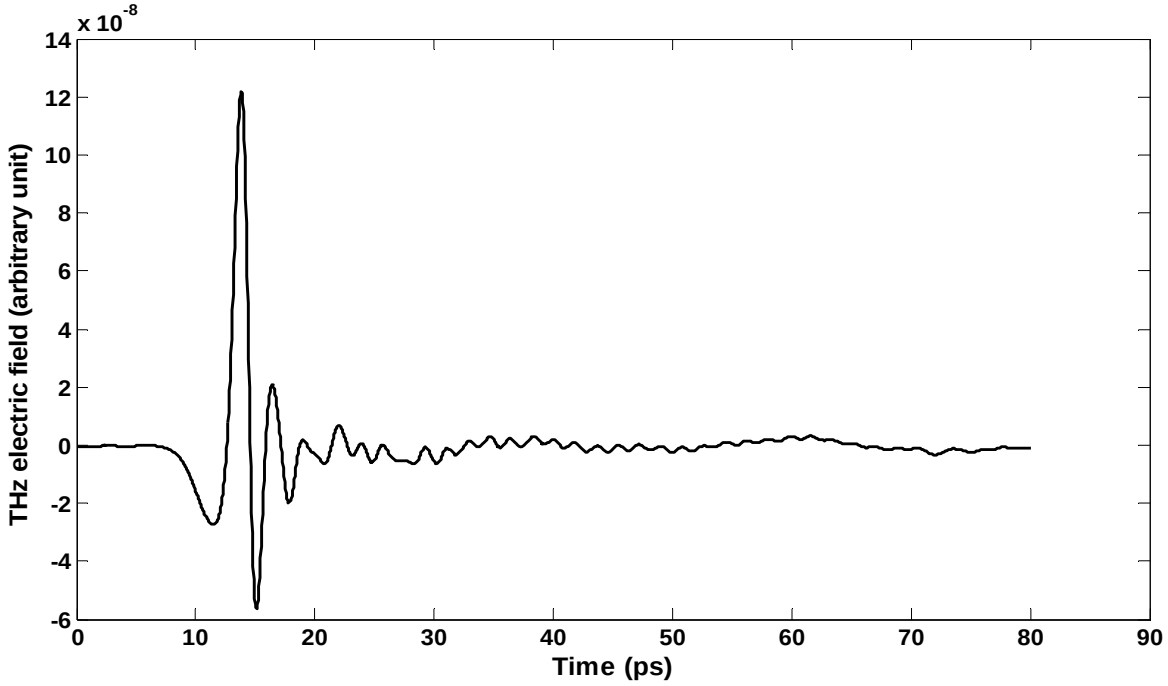


Fig 5. 13 Time domain graph of the THz pulse in absence of the tooth crown sample

5.2.4.2.2 Added reflections to the pulse shape

Another property that can be recognized in this figure is the reflections that have been added to the reference pulse shape. A very strong assumption is that these reflection peaks are mainly due to the reflections from the interface of different layers of the sample and this assumption is based on the calculations that are going to be presented shortly. However, occurrence of such reflections may be because of some other phenomena. If the peaks observed in figure 5.12 are due to reflections, it means that the THz beam has been reflected from one of the walls shown in figure 5.14 as W1 to W6, traveled a distance in the opposite direction and then again reflected by another wall directly to the detector.

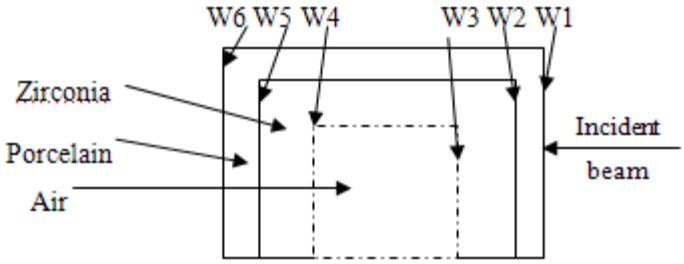


Fig 5. 14 A schematic of the tooth crown sample with different layers and interfaces highlighted

Therefore, in order to calculate the time delay between the major pulse and its reflection, the following equation can be used:

$$2d = \frac{c}{n}.\Delta t \Rightarrow \Delta t = \frac{2dn}{c} \tag{5.13}$$

This says that the delay of the reflected beam depends on the extra distance that it has travelled and on the speed of light in the medium where the beam travelled.

Using this concept, there are a few possibilities of reflection from different walls of the sample which are going to be analyzed below:

If we assume that the THz pulse was reflected from W3 and again reflected from W2, then by using equation 5.13 together with the values for thickness from figure 5.3 and the values for the refractive index of different layers of the sample, we can find the time delay:

$$\Delta t_1 = \frac{2x_2 n_2}{c} = \frac{2(1.2)(2.15)}{c} = 17.2\,ps \tag{5.14}$$

If we assume that the THz pulse was reflected from W3 and again reflected from W1, then the delay time would be:

$$\Delta t_2 = \frac{2x_1 n_1}{c} + \frac{2x_2 n_2}{c} = \frac{2(0.4)(1.5)}{c} + \frac{2(1.2)(2.15)}{c} = 21.2\,ps \tag{5.15}$$

If we assume that the THz pulse was reflected from W4 and again reflected from W3, then the delay time would be:

$$\Delta t_3 = \frac{2t.n_0}{c} = \frac{2(5)(1)}{c} = 33.3\,ps \tag{5.16}$$

If we assume that the THz pulse was reflected from W3 and again reflected from W1, then the delay time would be:

$$\Delta t_4 = \frac{2t.n_0}{c} + \frac{2x_2 n_2}{c} = \frac{2(5)(1)}{c} + \frac{2(1.2)(2.15)}{c} = 50.5\,ps \tag{5.17}$$

Now, if we assume that the peak of the THz pulse in the graphs of figure 5.12 is the transmitted signal which hasn't gone under any reflection, then we can find the time delay between this major peak and the reflected pulses in the measurements as shown in the figure below:

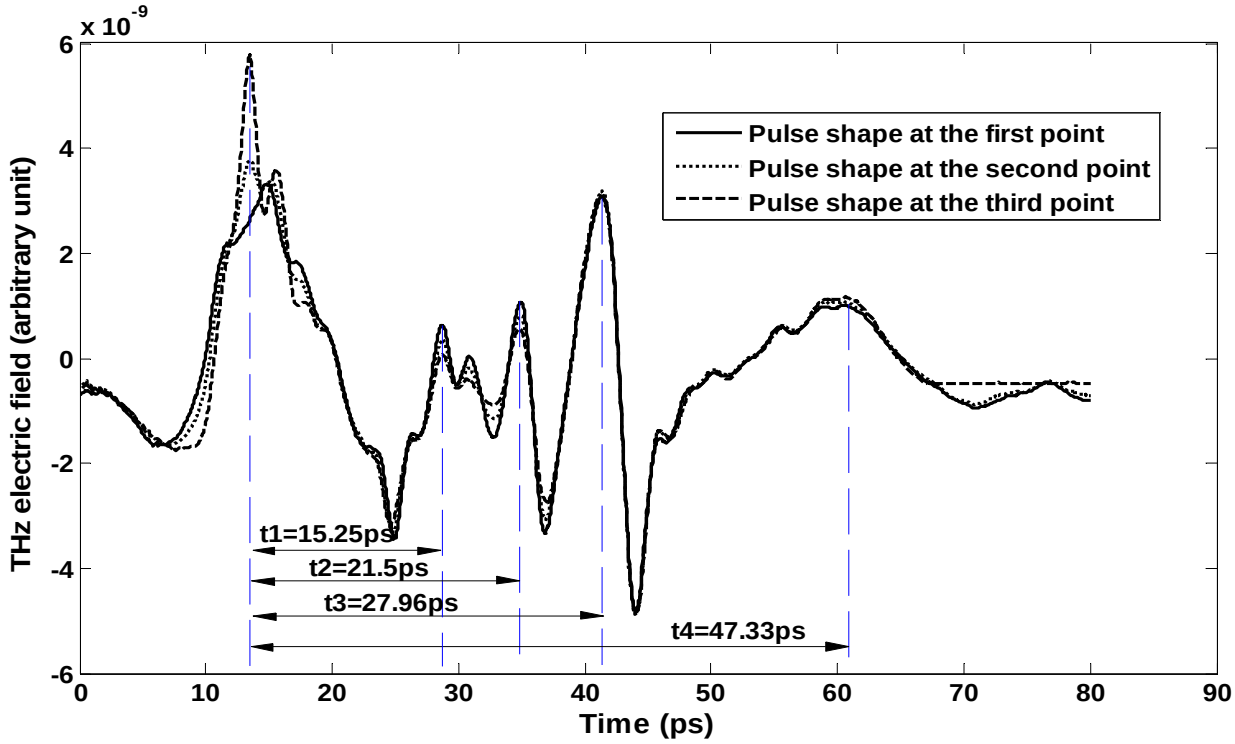


Fig 5. 15 The time delay between the major pulse and the reflected pulses for three points on the tooth crown sample located 0.5mm from one another

Note that the value used as the refractive index for the two different layers of the tooth crown sample, made of zirconia and porcelain, has been found from literature. The change of refractive index with

wavelength has been neglected in the above calculations. Moreover, the thickness used in these equations is the average thickness of each layer.

By comparing the values that are found from the measurement ($t_1$, $t_2$, $t_3$, $t_4$), with the values obtained from equations 5.14 through 5.17 ($\Delta t_1$, $\Delta t_2$, $\Delta t_3$, $\Delta t_4$), we can see that the measurement agrees with the theoretical result to some extent.

5.2.4.2.3 Pulse broadening

The other effect that can be recognized in these graphs is pulse broadening, especially for the graph shown in full line. In the graph of the reference pulse, in the absence of the sample, we can see a minor reflection after the major peak which is quite distinguishable from the major peak. Since this reflection is present in the absence of the sample, we can deduce that this reflection is a reflection from the source and is not due to the change in the refractive index of the sample. The same reflection is also present in the pulses detected in presence of the sample but we can see that this peak has overlapped with the major peak of the THz signal especially for the graph in full line. This shows that the major pulse has been broadened because of dispersion and has overlapped with the next peak. This phenomenon, as mentioned before, generally occurs when the refractive index changes with wavelength. As we can see here, the graph in full line shows a greater pulse broadening than the other graphs. One explanation for this can be that this graph corresponds to a point of the sample which is close to the lateral edges of the sample where the THz beam travels mostly inside the tooth crown sample material and not through the empty space between its two walls. Therefore, because of traveling a longer distance in a material with a refractive index much more than that of the free space, the pulse broadening is more noticeable in the graph in full line, while the other graphs correspond to the case in which the beam is traveling around the center of the tooth and mostly through the free space and less through the sample's material. This can be confirmed by the fact that more attenuation can be distinguished in the major pulse of the graph in full line which has happened because the THz beam travels a longer distance in the tooth crown sample's material and thus is more attenuated.

## 5.3 Summary

In this chapter the methods that had been used to perform the experiments of this thesis were discussed. The methods of measurements such as 2D imaging of a phantom sample, spatio-temporal imaging of a tooth crown sample, finding the beam profile and the MTF with the THz pulse and THz continuous-wave set-ups were explained. The methods that were applied to obtain results from the

theory or from simulations in HFSS were also shown. Moreover, the results of the measurements, theoretical calculations and simulations were presented and have been compared together to represent imaging parameters of both of the imaging set-ups. The captured images of the samples were also demonstrated to either reveal certain information about the structure of the sample or to highlight the imaging parameters of the set-ups.

# Chapter 6
# Summary and conclusion

Owing to characteristics of Terahertz wave such as being nonionizing and performing less Rayleigh scattering than infrared wave, together with the behavior of a number of polar molecules such as certain biological tissues at these frequencies have madeTerahertz one of the novel eligible candidates for spectroscopy and imaging in medical applications.

So far, several research groups have done experiments on THz imaging of biological tissues. The examples of these series of experiments which were also discussed in the review sections of this thesis are tooth imaging for detection of early caries, burn diagnostics and in-vitro imaging of skin and breast cancer. Due to some advantages of THz imaging in distinguishing certain details in some biological tissues, it is believed that Terahertz radiation has the potential to become a conventional medical imaging method either to be used independently or as a complement to other common imaging methods such as MRI and X-ray.

As the initial steps towrds developing a THz medical imaging system, this thesis focuses on the imaging capabilities and imaging parameters of the two experimental set-ups: THz pulse imaging and THz continuous-wave (CW) imaging set-up. Experiments on finding the imaging parameters such as resolution, MTF and beam profile of both of the set-ups were done and the results were compared to the results obtained from theoretical calculations. Simulations in HFSS were also done to verify some of the assumptions and results. Some experiments were also performed on a tooth crown sample in order to prove the ability of the THz pulse imaging set-up to reveal information of the sample's thickness by time-of-flight imaging.

The first set of experiments performed on the T-shaped sample, showed that the effect of using beams of higher frequency in the CW set-up on improving the resolution is much more than the effect of increasing the sampling rate (decreasing the pixel size) in the THz pulse imaging set-up, which confirms the direct dependence of resolution on the beam size. Moreover, comparing the MTF of the CW set-up at different frequencies with the MTF of the pulse set-up, although the limiting resolution of the pulse set-up is less than that of the CW at higher frequencies, shows that the performance of the pulse set-up is better than the CW set-up at resolutions less than its limiting resolution. This means that for the cases that obtaining better performance is of higher importance than obtaining higher resolution, the pulse set-up may be a better option.

Another set of experiments were done to find the beam waist in both of the imaging set-ups. In the thesis, it had been shown that the beam at the focus of both of the set-ups can be approximated as a Gaussian beam. With this assumption, the beam waist was measured for both of the set-ups throughout the experiments as well as by using the formula for the beam waist of a Gaussian beam mentioned in the thesis. The results obtained from the two methods were close, both for the pulse set-up and for most of the frequencies of the CW set-up. This confirmed that approximating the beam profile at the focus of the imaging systems as a Gaussian beam was a moderate assumtion.

Throughout another experiment which was to find the MTF of both of the imaging set-ups, the resolution was improved in the CW set-up with an increase in frequency. Moreover, the limiting resolution of the pulse set-up was very similar to that of the CW set-up at 450GHz which was mainly because of the concentration of the energy of the pulse around a close range of frequency (350GHz); however, as mentioned earlier, the performance of the pulse set-up at resolutions less than the limiting resolution was better than that of the CW set-up. Moreover, the width of the main lobe of the Airy disk was measured from both the theoretical formula (diffraction limit) and from the beam profile which was obtained throughout the experiments. These two values were compared to each other and to the limiting resolution extracted from the graph of the MTF. A relatively large difference can be distinguished between the calculated diffraction limit and the measured width of the main lobe of the beam profile which showed that the resolution of our imaging set-ups was confined by more parameters than just the diffraction limit. In addition, The limiting resolution obtained from the MTF graphs was much less than the diffraction limit of the set-ups. One main reason was the presence of the noise in the system which demanded for low-pass filtering the MTF results in MATLAB before plotting and this reduced the bandwidth and the resolution as well as the noise. To conclude, it is obvious that both of the imaging set-ups are not diffraction-limited and sources of noise (such as the chopper or the detector) and sources of aberrations (misalignment or the spherical lense) have caused the resolution to drop below the diffraction limit.

The objective of developing a THz imaging set-up was to eventually use it for imaging of in-vitro biological samples and among them, tooth was of more interest to me. Generally, pulse imaging set-up is considered as a better choice for tooth imaging because of its ability in depth measurements. However, CW imaging set-ups have also been used in literaure for tooth imaging. As the first step towards THz tooth imaging with the pulse imagig set-up, I used a tooth crown sample and as the final experiment of this thesis, I captured the image of an in-vitro cross-section of a premolar tooth with the CW imaging set-up.

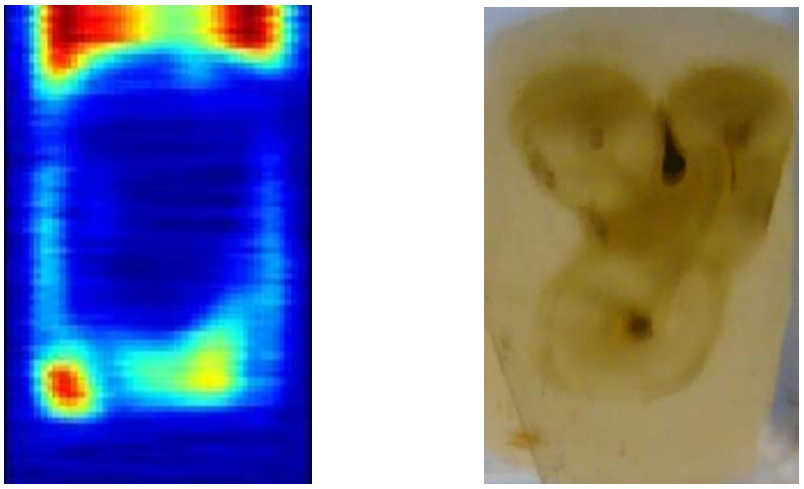

Fig. 6. 1 Images of a dried premolar tooth cross-section with thickness of 700µm. Left) The THz image at 950GHz captured with the CW set-up; Right) Optical image. The blue region shows the tooth and the red region shows the polyethylene around the sample. The dark blue region in the middle is the dentin which has a higher absorption than enamel (the lighter blue around the center)

Based on the experiments done on the tooth crown sample with the THz pulse imaging set-up in this thesis, it was shown that the thickness of different layers of such sample could be measured by measuring the time-daley between the main THz peak and its reflections after passing through the sample and also by measuring the displacement of the THz peak of the pulse that passed through the sample and the THz peak of the reference pulse that was detected in the absence of the sample.

The experiments performed on the tooth crown sample with the pulse imaging set-up and on the tooth cross-section by the CW set-up have proved the ability of our imaging set-ups to provide meaningful information about the sample. This opens the door to many nobel future works that can be done with these set-ups especially in the field of tooth imaging. In my opinion, future work can be focused on first calibrating the two imaging set-ups in order to obtain more precise images. Then, the calibrated set-ups can be used to capture images from cross-sections of tooth in order to identify the regions including caries. Moreover, imaging experiments can be performed on in-vitro samples of cancerous tissues to verify the ability of our pulse and CW imaging set-ups in differnciating between cancerous and healthy tissues.

# Appendix A: Gaussian beam shaping [2]

When a Gaussian beam passes through a thin lens, its amplitude doesn't change but its phase changes. This means that the complex amplitude of the beam is multiplied by the complex amplitude transmittance of the lens which is shown as exp ($\frac{jk\rho^2}{2f}$). By applying this phase change to the incident Gaussian wave, we can find out the shape of the beam that comes out of the lens and its corresponding parameters. According to equation 5.1, the phase of the beam can be shown as $kz + \frac{k\rho^2}{2R} - \zeta$ which after passing through the thin lens changes to $kz + \frac{k\rho^2}{2R} - \zeta - \frac{k\rho^2}{2f}$. This can be rewritten in the following form:

$$kz + \frac{k\rho^2}{2R} - \zeta - \frac{k\rho^2}{2f} = kz + \frac{k\rho^2}{2R'} - \zeta \tag{A.1}$$

Where $\frac{1}{R'} = \frac{1}{R} - \frac{1}{f}$.

This means that the output beam is also Gaussian with a radius of curvature equal to $R'$.

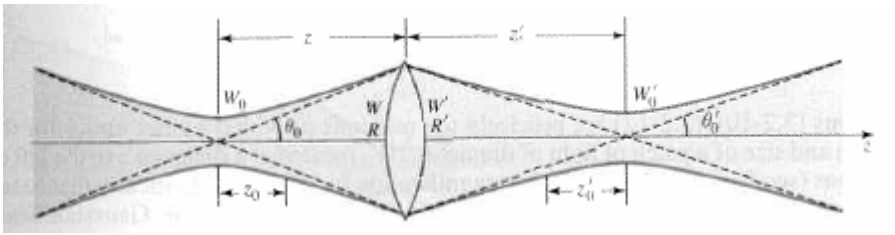


Fig. A. 1. Gaussian beam reshaping using a thin lens [2]

For a Gaussian beam, there are two equations (A.2 and A.3) which relate the radius of curvature and beam width to the Rayleigh range and beam waist.

$$z = \frac{R}{1 + (\frac{\lambda R}{\pi W^2})^2} \tag{A.2}$$

$$W_0 = \frac{W}{\sqrt{1 + (\frac{\pi W^2}{\lambda R})^2}} \tag{A.3}$$

Substituting $R$ with $R'$in these two equations, the values of $W_0{}'$and $z'$ can be calculated for the beam which has passed through the thin lens. Then by using those two equations together with $\frac{1}{R'} = \frac{1}{R} - \frac{1}{f}$ and equation 5.3, we can find $W_0{}'$in terms of z. Then, by substituting z with zero, we find the following equation for the beam waist of a Gaussian beam after passing through a thin lens.

$$W_0 = \frac{D}{\sqrt{1 + (\frac{z_0}{f})^2}} \tag{A.4}$$

This formula is used in chapter 5 to calculate the Gaussian beam waist in theory and compare it to the results of the measurement.

# Appendix B: Alignment of the CW set-up

Our CW imaging set-up consists of a Backward wave oscillator as the source, Golay cell or Pyroelectric as the detector, a chopper, an attenuator and a number of lenses for focusing, defocusing or collimating the beam. A picture of our CW set-up has been shown in figure B.1 and a schematic of this system is shown below.

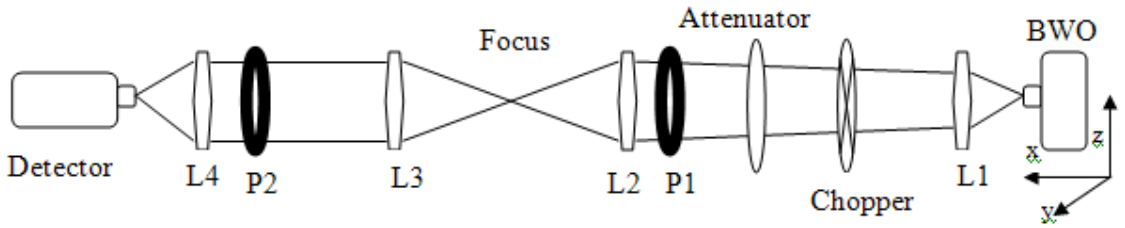


Fig. B. 1. A schematic of the CW imaging set-up

Through the alignment procedure, different parameters of the elements of the set-up–such as position of the elements, the tilt of lenses or mirrors, etc- must be changed in order to adjust the beam along the desired path. This procedure is iterative; meaning that after each time that the system was better aligned by changing all the variables, the procedure must be repeated by changing the same parameters in the same order. Generally, it is better to reduce the number of variables of the set-up by fixing some of them in order to avoid too many degrees of freedom and making the procedure more controllable. Note that the attenuator can be put anywhere in the set-up without causing much change in the received power at the detector but the chopper should be put as far as possible from the detector because otherwise it would chop the noise as well as the signal and the signal to noise ratio would decrease.

In different set-ups, different techniques may be used in order to make sure that the beam is aligned; for example, using certain instruments to view the beam along its path (such as IR-viewer which is used to view infrared beam), maximizing the signal received at the detector, or using irises. In our continuous-wave set-up, we need to align the beam generated by the BWO along a straight path.

Since there is no way to directly view the beam at the frequencies generated by BWO, the general idea we can use to align our set-up is to use irises and try to maximize the signal at the detector at the same time.

The first step is to know the parameters of our set-up and to see how we can reduce the number of variables by fixing some of them and changing the others throughout the alignment. All four lenses, chopper, attenuator and the detector can be moved freely along x, y and z-direction. According to some manufacturing problems of the BWO that we use in our set-up, the phase plane of our BWO is not perpendicular to the xy and xz-plane, that is why we had to put the BWO on a tilt stage which moves parallel to xz-plane and on a rotation stage which moves parallel to xy-plane. Therefore, the BWO is free to move only in y-direction and can be tilted in xz and xy-plane.

To start, we take the sample and the two object lenses (L2 and L3) out of the set-up. The reason is that L2 and L3 are just used for focusing the collimated beam on the sample, so we first need to align the set-up in absence of L2 and L3 so as to have a collimated beam along the path between the BWO and the detector. Since at the frequencies generated by BWO the beam cannot be viewed with any instrument, the best way to control the beam path is to fix the detector, attenuator, chopper, L1 and L4 along the same y-coordinate and then set the height of all these elements to the same height as the waveguide of the BWO. But first, we have to make sure that by using the tilt stages, we have adjusted the surface of the waveguide parallel to the zy-plane. Moreover, L1 must be placed at a distance approximately equal to its focal length from the BWO and L4 must be placed at a distance approximately equal to its focal length from the detector. These two distances would be finely tuned during the procedure. The surface of L1, L4, attenuator, chopper and detector must also be tilted to be parallel the zy-plane. At this point, the position of the attenuator and chopper are fixed and wouldn't be changed during the procedure. L1 and L4 have a fixed position along y and z but their x-position must be changed slightly during the alignment. The most efficient way to do this is to put L1 on a translation stage which can be moved along the x direction while fixing L4 at a certain x-position. Whenever we needed to change the distance between L4 and the detector, we can do so by changing the x-position of the detector. Even though the position of the detector is approximately tuned at the same y and z as the other elements of the set-up, these two parameters may be changed very slightly during the alignment.

At this point, there are five major and two minor variable parameters in the set-up which can be changed in this iterative alignment method. The major variables are the y position and tilt in xy and xz-plane of the BWO, x position of L1 and the x position of the detector and the minor ones are the y

and z position of the detector. Now we put an iris with a diameter equal to that of the lenses at P1 and set its height so that its center would be along the same line as the optical center of L1 and L4. By changing the y position of the BWO, the x position of L1 and the x,y and z- position of the detector and repeating the procedure in a periodic manner, we can find the configuration at which the maximum power is received at the detector. Note that at this point, we do not change the tilt of the BWO because the iris located at P1 is close to the BWO and thus a change in the tilt of the beam would not be recognized. To adjust the tilts of the BWO, we must put an iris at P2. At this location, as the iris is relatively far from the source, a slight change in the tilt of the beam would have a large effect on the power detected at the detector. Therefore, by changing the tilts of the BWO in the xy and xz-plane, the x position of L1 and the x, y and z- position of the detector and repeating the procedure in an iterative manner, we can find the configuration at which the maximum power is received at the detector. Then, we can put the iris at P1 again and repeat the same procedures as done before and keep repeating the alignments with the iris at either P1 or P2 until system begins to converge. Note that changes in the y and z position of the detector must be very small so that its y and z-position would be the same as that of the optical center of the lenses.

At this point, we are sure that the beam is passing through a pinhole as big as the diameter of the lenses while the beam waist of the beam at the frequencies at which we're doing the alignment is a few times less than this. Therefore, in order to do fine tuning, we need to reduce the size of the irises to about one centimeter and by just changing the parameters of the BWO (y-position, xz and xy tilt) we try to maximize the power detected at the detector. A further step would be to cover half of an iris with an absorbing material and see if the detected power is divided by two; if not, we first have to change the tilt of L1 (if the beam is tilted to the right or left) or change the height of L1 (if the beam is tilted to up or down). If this didn't solve the problem, then it means that the tilt of the BWO in that direction must be changed. Note that at this stage, the only parameters which must be changed to maximize the output power are that of the BWO. So, the detector or lens positions should not be changed.

At this point, the beam is collimated along a certain line. In order to use this collimated beam to scan a sample, we need a couple of identical lenses, one for focusing the collimated beam on the sample and the other for collimating the beam transmitted through the sample. Therefore, the lenses must be placed apart at a distance equal to the summation of their focal length. The best way is to first align the y and z-position of the center of the lenses to the center of other lenses of the set-up, then, completely fix one of the lenses (say L2) and move the other one along the x- direction (and very

slightly along y and z-directions) in order to get the maximum power at the detector. Note that due to the experiments, a standing wave is formed between the surface of the detector and L4. After adding L2 and L3 to the system, because of the change in the beam's path, the phase of the beam changes, which may cause a phase shift in the standing wave formed between the detector and L4. Therefore, a reduction in the output power may not mean that L3 needs to be realigned but may be because the detector is no more at the peak of a standing wave. So, besides changing the position of L3, the x-position of the detector must also be changed in order to achieve the maximum power at the detector. Note that the face of the two object lenses must be always parallel to zy-plane.

Now that the optimum configuration of the object lenses has been achieved, we need to find the focus point of L2 and L3 in order to put the sample there. The sample must be placed on a three dimensional stage which can be moved in x, y and z directions. In order to find the focus point, we put a small pinhole opened at its largest size on the 3D manual stage and by moving the three stages along each of the three possible directions with the screws; we try to find the position at which the output power is maximized. When such position was found, we decrease the size of the pinhole and repeat the same procedure but by using those screws of the stages which are designed for fine-tuning. If we continue to decrease the size of the pinhole, when the output power was maximized for the smallest pinhole size, we can be sure that the focus has been found with a good approximation. In order to scan the sample, we need to replace the pinhole with the sample and make sure that the x, y and z of the center of the sample is placed exactly at the position of the center of the pinhole.

# Appendix C: Alignment of the pulse set-up

The problem that occurs in sensitive set-ups such as our pulse THz set-up is that their alignment may change after some time (maybe a few days or weeks) due to room environmental fluctuations such as temperature and then, the THz pulse can't be detected anymore. There are some steps that must be taken in order to correct the alignment and retrieve the THz pulse. The procedure is described below.
There are two categories of optical elements in a pulsed set-up. The first are those used for aligning the IR beam and the second are those used for aligning the THz beam. A schematic of our THz pulsed set-up is shown in the figure below. In this figure the IR beam is shown with a solid line and the THz beam is shown with a dashed line.

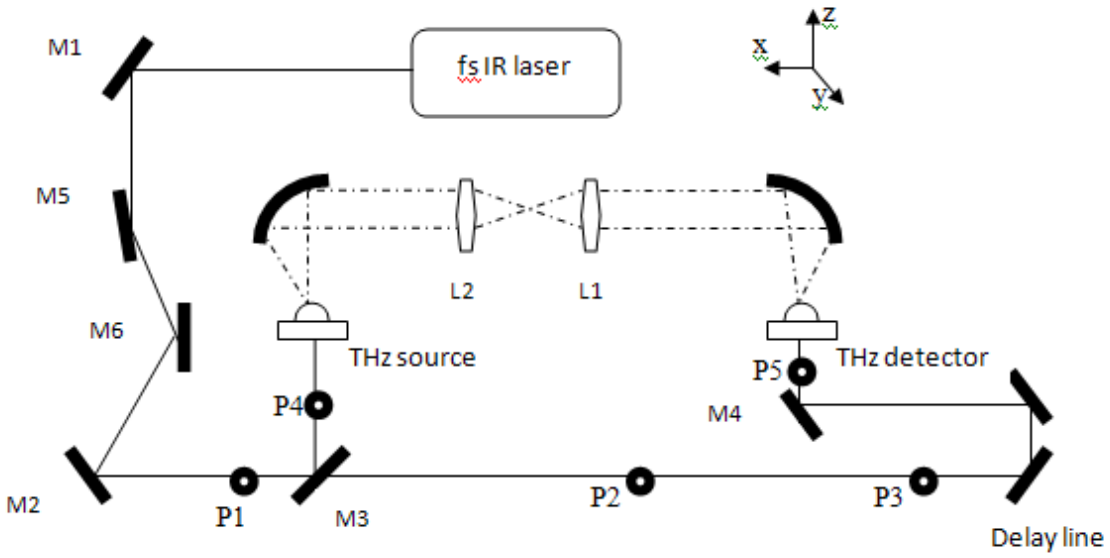


Fig. C.1. A schematic of the Pulse imaging set-up

To start, we first have to take the sample and the two objective lenses (L1 and L2) out of the set-up. Then, we have to check the alignment of the IR beam. The advantage of this part of the alignment is that unlike the THZ beam, the IR beam can be seen and traced by an IR-viewer. To trace the IR beam, we put small pinholes at different positions along the path of the IR beam and by using the IR-viewer, we check to see if the beam is passing through the middle of the pinhole or not. If the beam

was not passing through the middle of the pinhole, we have to adjust the beam path through the pinhole by changing the tilt of the mirror which is relatively far from the pinhole. To understand this concept, let's go back to figure C.1. If we put the pinhole at P1 and the beam isn't passing through the middle of this pinhole, it is obvious that changing the tilt of M2, M5 and M6, which are near this pinhole, may not change the position of the beam in this pinhole very much while a small change in the tilt of M1would greatly affect the position of the beam passing through P1 and thus makes the alignment more accurate. According to the same concept, it would be best to align the position of the beam passing through P2 with M5 (or even M6) and align the position of the beam passing through P3 with M2. For the beam passing through P4 and P5, we use M3 and M4 respectively, even though they are relatively close to the pinholes. The reason is that for example for aligning the beam passing through P4, using any mirror in the set-up (except M3) would also change the beam path passing through P2, P3 and P5. M3 is the only mirror that a change in its tilt would just affect the beam passing through P4. The same debate holds for P5 and M4.

After making sure that the IR beam is traveling along the correct path, we have to check if the THz signal is being generated in the set-up. The first step would be to see if photocurrent is being generated in both the source dipole and detector dipole. To do this, we put the chopper in front of the THz source to let the IR beam be modulated before hitting the gap of the dipole. We connect the output of the source dipole to a current amplifier and from there to the lock-in and apply a bias voltage to the dipole. By twisting the screws of the translation stage on which the source dipole is installed, we can move the dipole in the horizontal and vertical direction in a plane perpendicular to the incident IR beam, in order to find the dipole's gap and let the IR beam be incident on it. The best way to do this is to twist one of the screws in one direction and if the photocurrent shown on the lock-in is increasing, we continue to twist in the same direction and if not, we twist the screw to the other direction. Then, we do the same thing with the other screw and we repeat maximizing the current by switching between the screws alternatively to find the gap. After it was checked that photocurrent is being generated by the source dipole, we have to repeat the same procedure for the detector to make sure that the IR beam is hitting the detector at the dipole's gap.

After we checked that the incident IR beam and the IR probe beam are hitting the correct points of the source and detector dipole respectively, we need to check the path of the THz pump beam generated at the source and incident on the detector. To check this, we connect the signal generator to the source dipole to provide the pulsed bias voltage and connect the output of the detector dipole to the current amplifier and from there to the lock-in. We change the position of the delay-line by moving its

translation stage over its whole range to see if the THz pulse can be detected or not. If the THz pulse cannot be detected, either the alignment of the parabolic mirrors has changed or the silicon lenses at the back of the source and detector dipoles have been displaced. The first case is less probable in our set-up because the parabolic mirrors are fixed after being aligned for the first time. When the second case happens, the silicon lenses of both the source and detector must be checked. Two screws are attached to the pad that holds each of the lenses. One moves the silicon lens horizontally while the other moves it vertically. Let's say we start with checking the detector first. We start twisting one of the screws attached to that lens in a certain direction then by changing the delay-line; we try to find the position of the signal's peak. If the peak value has increased, we continue twisting the same screw in the same direction and every time, to check if the signal has increased or not, we need to change the delay-line to find the peak of the THz signal, because any slight change in the position of a silicon lens, changes the delay of the THz pulse. When the signal is not increasing anymore, we start twisting the other screw in a certain direction and repeat the same procedures. After the maximum signal is achieved by twisting the other screw, we go back to the first screw. We repeat the same periodic alignment for the detector until its maximum signal wouldn't increase anymore. Then, we can move on to the source's silicon lens and do the same procedures for it. By repeating the same procedure for both lenses, for a few times, the THz pulse can be recovered.

Now, we must put the object lenses between the two parabolic mirrors –as shown in figure C.1- in order to focus the THz beam on the sample, but first, we need to find the path of the THz beam between the two parabolic mirrors. To do this, we put an open iris on a two dimensional translation stage and between the two mirrors. Then, by changing its y and z position, we try to obtain the maximum signal passing through it and by repeating the same procedure for smaller pinhole sizes, we try to find the approximate position of the center of the THz beam so as to place the optical center of the lenses at the same y and z coordinates but at different x positions. We fix the position of one of the lenses and since this changes the phase of the THz beam, we change the delay-line to find the position at which the signal is at its peak value. Then we put the other lens at a distance around two times the focal length of the lenses from the fixed lens and by changing its position along x direction and a slight change in y and z directions, we find the position at which the THz signal is maximum. Note that after adding the second lens to the system, we should change the delay line again to compensate the phase shift. Then, we should change the position of the second lens and the delay-line again to obtain the maximum possible signal. Note that the face of the object lenses must be parallel

to the zy-plane. After fixing the position of the two object lenses, we need to find the focus point between them where we put the sample.

The sample must be placed on a three dimensional stage which can be moved in x, y and z directions. In order to find the focus point, we put a small pinhole opened at its largest size on the 3D-stage and by moving it along each of the three possible directions; we try to find the position at which the output power is maximized. When such position was found, we decrease the size of the pinhole and repeat the same procedure but by using the screws for fine-tuning. If we continue to decrease the size of the pinhole, when the output power was maximized for the smallest pinhole size, we can be sure that the focus has been found with a good approximation. In order to scan the sample, we need to replace the pinhole with the sample and make sure that the x, y and z of the center of the sample is placed exactly at the position of the center of the pinhole. Note that if we are performing a two dimensional transmission imaging, the peak of the THz signal must be located at the surface of the sample. Therefore, when we put the sample on the beam's path, we need to find the peak of the THz signal again by changing the delay-line. However, if we are performing a depth measurement, there's no need to do so because in depth measurement, the whole range of the delay-line is scanned at each point of the sample to find out the whole THz pulse.

# Bibliography


[1] D.M. Mittleman, *Sensing with Terahertz Radiation*, Springer, 2003

[2] B. E. A. Saleh, and M. C. Teich, *Fundamentals of Photonics*, A John and Sons, Inc., Publication, 2007

[3] Joseph W. Goodman, *Introduction to Fourier optics. Englewood*, Colo. : Roberts &Co., 2005

[4] R.F. Harrington, *Time-Harmonic Electromagnetic Fields*, IEEE Press Series on Electromagnetic Wave Theory, 2001

[5] T. L. Williams, *The optical transfer function of imaging systems*, Institute of Physics Publishing, c1999

[6] G. D. Boreman, , *Modulation Transfer Function in optical and electro-optical systems*, SPIE Press, 2001

[7] Rafael C. Gonzalez, and Richard Eugene Woods, *Digital Image Processing*, Addison-Wesley Publishing Company, 2002

[8] M. Born, and E. Wolf, *Principles of Optics*, London: Pergamon, 1959

[9] Chris Guy, and Dominic Ffytche, *An Introduction to the Principles of Medical Imaging,* London: Imperial College P, 2005

[10] Vadim Kuperman, *Magnetic Resonance Imaging, Physical Principles and Applications*, Chicago: Academic P, 2000

[11] Fred A. Mettler, and J. Guiberteau Milton, *Essentials of Nuclear Medicine Imaging,* Philadelphia: W.B. Saunders, 1991

[12] K. Kirk Shung, Michael B. Smith, and Benjamin M. W. Tsui, *Principles of Medical Imaging,* San Diego; Toronto: Academic P, 1992

[13] T. Loffler et al, "All-Optoelectronic Terahertz Imaging Systems and Examples of Their Application", *Proceedings of the IEEE*, vol. 95, NO. 8, pp. 1576-1581, 2007

[14] J. M. Chamberlain, et al., "What Constitutes a Useful and Meaningful Terahertz Image", *Proceedings of the IEEE*, pp. 81- 84, 2007

[15] J. F. Federici, et al., "Terahertz Near-field Imaging", *Physics in Medicine and Biology Series*, Institute of Physics Publishing, 2002

[16] Bradley Ferguson, et al., "T-ray Computed Tomography", *Optics Letters*, Vol. 27, No. 15, 2002

[17] W. L. Chan, et al., "Terahertz imaging with compressed sensing and phase retrieval", *Conference on Lasers and Electro-optics*, pp.1-2, 2007

[18] P., H. Siegel, "Terahertz Technology in Biology and Medicine", *IEEE Transactions on Microwave Theory and Techniques*, Vol. 52, No. 10, pp. 2438 - 2447 , 2004

[19] Roger Appleby, Rupert N. Anderton, "Millimeter-Wave and Submillimeter-Wave Imaging for Security and Surveillance", *Proceedings of the IEEE*, vol. 95, NO. 8, pp. 1683-1689, 2007

[20] Vincent P. Wallace, et al, "Biomedical Applications of THz Imaging", *IEEE MTT-S Digest*, pp. 1579-1581, 2004

[21] K. Humphreys, et al., "Medical Applications of Terahertz Imaging: A Review of Current Technology and Potential Applications in Biomedical Engineering", *Proceedings of the 26th Annual International Conference of the IEEE EMBS*, pp. 1302-1305, 2004

[22] B. B. Hu, M. C. Nuss, "Imaging with Terahertz Waves", *Optics Letters*, Vol. 20, No. 16, 1995

[23] John J. Carey, "Near-field effects of Terahertz Pulses", PhD thesis, University of Strathclyde, Glasgow, England, 2002

[24] Daryoosh Saeedkia, Safieddin Safavi-Naeini, "Terahertz Photonics: Optoelectronic Techniques for Generation and Detection of Terahertz Waves", *Journal of Lightwave Technology*,vol.26, no.15, pp.2409-2423, 2008
[25] G. Dammertz, et al, "Development of a 140GHz, 1MW Continuous-wave Gyrotron for the W7-X Stellarator", *IEEE Transactions Plasma Sciences*, Vol. 30, No. 3, pp. 808-818, 2002
[26] A. J. Fitzgerald, et al, "An Introduction to Medical Imaging with Coherent Terahertz Frequency Radiation", *Physics in Medicine and Biology 47*, 2002
[27] A., P. Foulds, et al, "Terahertz Imaging of Wound Healing", *7th IEEE High Frequency Postgraduate Student Colloquium*, 2002
[28] E. Pickwell, and P. Wallace, "Biomedical Applications of Terahertz Technology", *Journal of Physics D; Applied Physics*, 2006
[29] A. J. Fitzgerald, et al., "Effects of Frequency on Image Quality in Terahertz Pulsed Imaging", *Proceedings of SPIE*, Vol 4682, 2002
[30] R. M. Woodward, "Terahertz Technology in Medical and Pharmaceutical Industry", *Preclinica, Vol. 2, No. 5*, 2004
[31] Craig M. Ciesla, , et al., "Biomedical Applications of Terahertz Pulse Imaging", *Proceedings of SPIE*, Vol 3934, 2000
[32] S. C. Islam, et al., "A THz Triangulation and Imaging System and its Application", *32nd International Conference on Infrared and Millimeter Waves*, 2007
[33] A. Hellicar et al., "Development of a Terahertz Imaging System", *IEEE Antennas and Propagation Society International Symposium*, Honolulu, USA, June, 2000
[34] S. Mickan, et al., "Analysis of System Trade-offs for Terahertz Imaging", *Microelectronics Journal 31*, 2000
[35] B.Davoudi, M.Khabiri, D.Saeedkia, and S.Safavi-Naeini, "Comparison of Image Resolution in THz Pulsed and Continuous-wave Imaging Systems", *Conference on Infrared, Millimeter and THz Waves*, September 2008
[36] J. A. Zeitler, and L. F. Gladden, "In-vitro tomography and non-destructive imaging at depth of pharmaceutical solid dosage forms", *European Journal of Pharmaceutics and Biopharmaceutics*, 2008
[37] Kaveh Houshmad, , "Defect detection via THz imaging: potentials and limitations", MASc. thesis, University of Waterloo, Waterloo, Ontario, Canada, 2008
[38] N. Fang, et al., "Sub-diffraction-limited optical imaging with a silver superlens", *Science 308*, 2005
[39] Ja-Yu Lu et al., "Optoelectronic-Based High-Efficiency Quasi-CW Terahertz Imaging", *IEEE PHOTONICS TECHNOLOGY LETTERS*, Vol. 17, No. 11, 2005
[40] A. Korestein-Ilan et al, "Terahertz radiation increases Genomic instability in human Lymphocytes", *Radiation Research 170*, pp 224–234, 2008
[41] A. F. Fercher et al., "Optical coherence tomography-principles and applications", *Reports on Progress in Physics 66*,pp. 239-303, 2003
[42] Victor X. D. Yang et al., "Interstitial Doppler optical coherence tomography", *Optics Letters*, Vol. 30, No. 14, pp. 1791-1793, 2005
[43] D. M. Mittleman et al., "T-ray imaging", *IEEE Selected Topic Quantum Electron.,* 1996
[44] Z .Jiang, and X. Zhan., "Terahertz Imaging via Electrooptic Effect", *IEEE Transactions on Microwave Theory and Techniques,* Vol. 47, No. 12, 1999
[45] A. J. Kreisler and A. Gaugue, "Recent progress in high-temperaturesuperconductor bolometric detectors:from the mid-infrared to thefar-infrared (THz) range", *Journal of Superconductor science & technology*, vol. 13, no 8, pp. 1235-1245, 2000

[46] A. J. Kriesler et al., “New Trend in THz Detection: High Tc Superconducting Hot Electron Bolometer Technology May Exhibit Advantage vs Low Tc Devices”, *IEEE/MTT-S International Microwave Symposium proceedings,* pp 345-348, 2007.
[47] www.springerlink.com/index/H27W4516833667P5.pdf
[48] www.wikipedia.org
[49] http://www.frascati.enea.it/THz-BRIDGE/